12-15-2017 10:30 AM

Adsorbed Gas Behaviour and Guest-Host Interactions in Ultramicroporous Metal-Organic Frameworks

Bligh Desveaux
The University of Western Ontario

Supervisor
Huang, Yining
The University of Western Ontario

Recommended Citation

Abstract

Metal-organic frameworks (MOFs) are a class of porous materials that have attracted much attention due to their large surface areas, high tunability and their high selectivity for gas adsorption applications. In this work, solid-state nuclear magnetic resonance (SSNMR) experiments and single crystal X-ray diffraction (SCXRD) experiments are used to investigate carbon dioxide adsorption within the ultramicroporous MOFs SIFSIX-3-Zn (Chapter 2) and ZnAtzOx. (Chapter 3). Analysis finds that the CO_2 SIFSIX-3-Zn undergoes wobbling motions with a low temperature dependence, and in ZnAtzOx undergoes wobbling and hopping motions with a low temperature dependence. SCXRD is used to precisely determine the CO_2 adsorption site in SIFSIX-3-Zn, centered within the pore. Chapter 4 discusses the use of SSNMR to study the effects of water adsorption within these MOFs, with preliminary results suggesting water is strongly adsorbed in both frameworks with a low degree of temperature dependence.

Keywords: Metal-organic frameworks, solid-state NMR, CO_2, SCXRD, adsorption.

Co-Authorship Statement

Dr. Victor V. Terskikh (University of Ottawa, Ottawa, Ontario) is credited for the acquisition of high field SSNMR spectra at 21.1 T. Theoretical calculations were also performed by V. V. Terskikh.

Dr. Paul D. Boyle (University of Western Ontario, London, Ontario) is credited for the SCXRD data collection and structure refinement presented in Chapter 2.

Acknowledgement

Foremost, I would like to thank my advisor Dr. Yining Huang for his constant teachings and supervision and his key role in supporting my research, and helping to shape this thesis into what it has become.

I would also like to extend thanks to Dr. Victor V. Terskikh from the National Ultrahigh field NMR Facility for solids, for running many of the NMR experiments that I could not perform at UWO. Additional thanks are owed to Dr. Paul D. Boyle for conducting single-crystal XRD experiments.

Then I would like to thank the members of my examination committee, Dr. T. K. Sham, Dr. François Lagugné-Labarthet, Dr. Richard Puddephatt and Dr. Sean Shieh (Department of Earth Sciences) for taking the time to conduct my thesis examination.

Finally, I would like to thank those who worked alongside me every day, including PhD students Shan Jiang, Shoushun Chen and Jason Zhang, and Master's students Zitong Wang, Bowei Wu and Hendrick Chan. Special thanks are owed to post-doc Dr. Bryan E. G. Lucier and NMR facility manager Dr. Mathew Willans, for their constant patience and help with the SSNMR spectrometer.

Table of Contents

List of Tables

List of Figures

List of Appendices

List of Abbreviations

BET	Brunauer–Emmett–Teller
CCS	carbon capture and storage
CP	cross polarization
CPO	Coordination Polymer of Oslo
CPS	curved position sensitive
CS	chemical shift
CSA	chemical shift anisotropy
CT	contact time
dobdc	2,5-dioxido-1,4-benzenedicarboxylate
EFG	electric field gradient
FMA	fumarate
FSLG	frequency-switched-Lee-Goldburg
GIPAW	gauge-including projector augmented wave
HETCOR	heteronuclear correlation
HKUST	Hong Kong University of Science and Technology
HUM	hybrid ultramicroporous material
IAST	ideal adsorbed solution theory
IRMOF	isoreticular metal-organic framework
MAS	magic-angle spinning
MIL	Matériaux de l′Institut Lavoisier
MOF	metal-organic framework
NMR	nuclear magnetic resonance

NOAA	National Oceanic and Atmospheric Administration
OMS	open metal site
ppm	parts per million
PXRD	powder X-ray diffraction
QI	quadrupolar interaction
REDOR	rotational-echo double resonance
rf	radiofrequency
RH	relative humidity
SBA	Santa Barbara Amorphous
SCXRD	single crystal X-ray diffraction
SDB	4,4′-Sulfonyldibenzoic acid
SSNMR	solid-state nuclear magnetic resonance
TEPA	tetraethylenepentamine
TGA	thermal gravimetric analysis
TMS	tetramethylsilane
TPPM	two pulse phase modulation
TTMS	tris(trimethylsilyl)silane
UiO	Universitetet i Oslo
VT	variable temperature
ZIF	zeolitic imidazolate framework
ZnAtzOx	zinc-aminotriazolato-oxalate

List of Symbols

B_0	strength of the external magnetic field
C_2	two-fold rotation axis
C_6	six-fold rotation axis
C_Q	nuclear quadrupole coupling constant
D	dipolar coupling constant
E	elementary charge (1.602×10^{-19})
h	Planck constant (6.626×10^{-34} J s)
I	nuclear spin
t_d	evolution time of indirect dimension
T_{1p}	relaxation time during magnetization transfer
P	equilibrium pressure of gas
P_0	saturated pressure of gas
Q	quadrupole moment
r_{IS}	internuclear distance
S_0	control spectrum
S_{CW}	selectivity for CO_2 over H_2O
S_r	reduced spectrum
V_{11}, V_{22}, V_{33}	principle components of electric field gradient tensor
α	rotational angle about C_6 axis
β	rotational angle about C_2 axis
γ	gyromagnetic ratio
$\delta_{11}, \delta_{22}, \delta_{33}$	principle components of chemical shift tensor

δ_{iso}	isotropic chemical shift
ΔS	difference spectrum
η_Q	EFG tensor asymmetry parameter
θ	angle between two axes
θ_m	magic-angle pulses
κ	chemical shift tensor skew parameter
λ	wavelength
μ_0	permeability of a vacuum
$\sigma_{11}, \sigma_{22}, \sigma_{33}$	principle components of chemical shielding tensor
τ	contact time
Ω	chemical shift tensor span parameter

Chapter 1 : Introduction

1.1 Background

1.1.1 The threat of atmospheric carbon dioxide

In 2013, the concentration of carbon dioxide in the atmosphere was observed to cross the 400 ppm threshold for the first time since records have been kept, as shown in Figure 1.1.[1] This represents an estimated increase of 130 ppm over pre-industrial levels.[2] Carbon dioxide is one of the most abundant of the greenhouse gases, which also include nitrogen oxide, methane and water vapour. These gases absorb infrared radiation emitted by the Earth and reemit it in all directions, warming the Earth.[3] Due to the enhancement of this greenhouse effect, it is estimated that global average surface temperatures will increase between 0.3 °C and 4.8 °C by the year 2100, as compared to temperatures between 1986 and 2005.[3, 4] This warming is expected to lead to more frequent and intense heat waves, a greater number of extreme precipitation events, ocean acidification, ocean warming, and sea level rise.[3, 4] Given the known problems associated with high atmospheric carbon dioxide concentrations, there is great interest in minimizing carbon dioxide emissions, which totalled 36.2 billions tons in 2015.[5]

While the stabilization of carbon dioxide concentrations can be achieved by substituting non carbon-based energy sources, such as wind and solar, the high costs of implementation combined with the current abundance of fossil fuels mean that this path is not immediately feasible. The Intergovernmental Panel on Climate Change has recommended the implementation of carbon capture and storage (CCS) as a necessary technology to mitigate increasing atmospheric CO_2 concentrations.[6, 7]
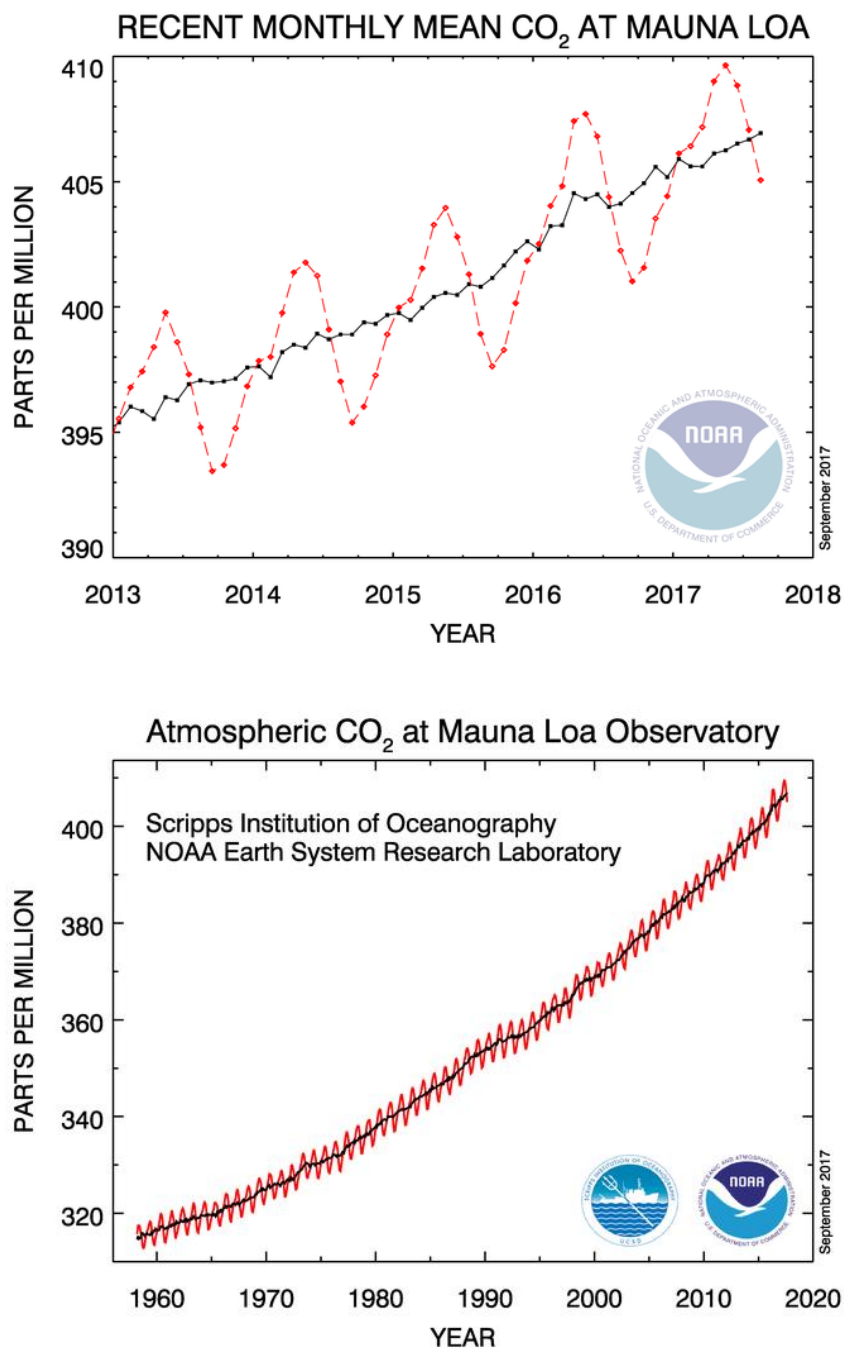
Figure 1.1: The graphs depict atmospheric CO₂ concentrations from 2013-17 (above), and from 1958-2017 (below), as measured at Mauna Loa, Hawaii). This image has been reproduced from reference 8.[8] The red line represents the monthly mean, while the black line is corrected for the average seasonal cycle. It can be seen that the atmospheric CO₂ concentrations just recently broke the 400 ppm threshold.

1.1.2 Carbon dioxide capture

Anthropogenic sources of carbon dioxide can be divided into two broad categories: point sources and mobile sources.[9] Point sources include energy production, heating, and industrial activities. Mobile sources of CO_2 are predominantly from the transportation and automobile industry. Point sources make up over half of anthropogenic carbon dioxide emissions, and their emissions can be dramatically reduced through the development and use of CCS technologies.[10] One of the most widely explored CCS strategies is post-combustion CO_2 capture. This strategy involves the extraction of CO_2 from flue gas streams, transportation of this CO_2 to a suitable storage site, and sequestration of the CO_2 in the storage site such that there is no leakage of captured CO_2.[11, 12] The capture process is illustrated in a general sense within Figure 1.2. There is also growing interest in developing technologies capable of CO_2 capture directly from the air, which would help negate CO_2 emissions from mobile as well as point sources.[9, 12]

One of the advantages of post-combustion CO_2 capture is that no modification is needed to existing combustion facilities in order to perform post-combustion capture. However, the low concentration of CO_2 in flue gas (between 4% and 15%) as well as the presence of impurities such as SO_2 and NO_x, are problems for many of the post-combustion gas separation processes.[6] Strategies for isolating CO_2 gas from flue gas streams include adsorption, absorption, gas separation membranes, and cryogenic distillation.[11] Of these, chemical absorption by alkanolamine aqueous solutions, such as monoethanolamine, is one of the most well explored options given present-day technology.[13, 14] However, there are numerous drawbacks to these chemical absorption processes, chiefly equipment corrosion, high energy consumption, solvent loss to evaporation and solvent degradation.[15] As a result, there is a growing amount of research going into the development of solid adsorption materials that can be employed in CO_2 capture.

The search for ideal solid adsorption materials has included investigations of more traditional solid sorbents (*e.g.*, zeolites, a class of microporous aluminosilicate materials, and activated carbons, a form of carbon processed to contain small volume pores), as well recently developed materials such as mesoporous silicas and metal-organic frameworks (MOFs).

STEP 1: Adsorption

High Pressure, Low Temperature

Flue Gas
(CO_2 + Other gases)

Sorbent Material + Adsorbed CO_2

CO_2 Free Gas
(Other gases)

STEP 2: Evacuation

Low Pressure, High Temperature

Sorbent Material

Isolated CO_2 Gas
(CO_2)
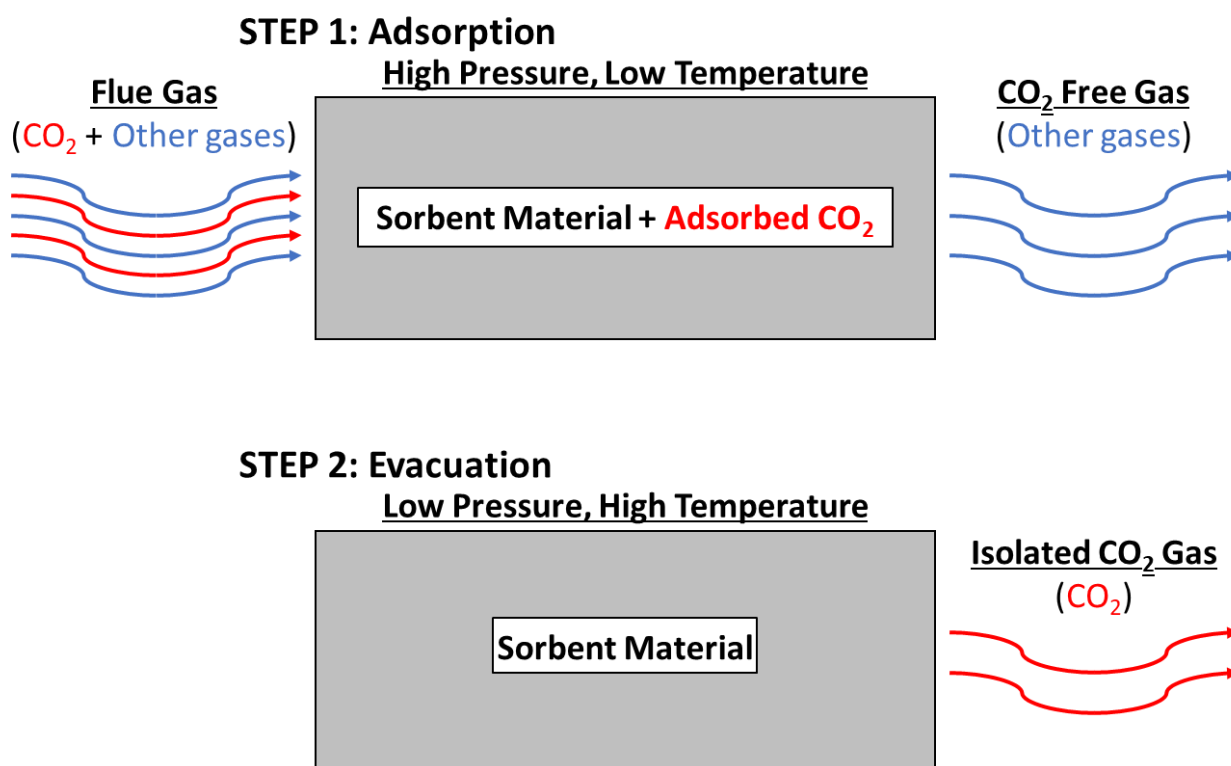
Figure 1.2: A simplified depiction of two-stage post-combustion carbon dioxide capture is shown. Carbon dioxide rich flue gases are compressed through a carbon dioxide adsorbing material. This material would later be evacuated under heat and vacuum, and the CO₂ gas isolated.

1.1.3 Metal-organic frameworks and their applications

MOFs have been studied for approximately two decades, during which research in the field has expanded dramatically. The phrase "metal-organic framework" was first introduced in 1995

by Yaghi et al.[16] Since the structure of MOF-5 was reported in 1999,[17] the MOF label has since expanded to include a broad class of coordination polymers with organic ligands which contain potential voids.[18] A small number of MOFs, such as zeolitic imidazolate framework-8[19] (ZIF-8) and HKUST-1 (named for the Hong Kong University of Science and Technology),[20] are currently available commercially. Crystalline MOFs can be synthesized through numerous methods,[21] including solvothermal, microwave-assisted,[22] electrochemical,[23] and mechanochemical routes.[24] MOFs are characterized by organic ligands acting as likers, which connect metal cations or metal clusters to form a three-dimensional framework.

Figure 1.3 depicts four different well known MOF structures: isoreticular MOF-1 (IRMOF-1 or MOF-5),[25] HKUST-1,[20] ZIF-8,[26] and M-MOF-74 (also known as Coordination Polymer of Oslo-27-M, abbreviated to CPO-27-M, or as M-dobdc for its 2,5-dioxido-1,4-benzenedicarboxylate ligands).[27] From these examples, it is apparent that the nearly endless combinations of organic and inorganic components leads to a class of highly diverse porous compounds. The structure and porosity of MOFs can vary with external factors (*e.g.*, temperature, pressure, etc.); research is to understand the behaviour and functionality of various MOFs is ongoing, which will assist in intelligently modifying the nature and functionality of MOF nodes and linkers. This will allow for the design of new MOF structures to address practical applications in the coming years.
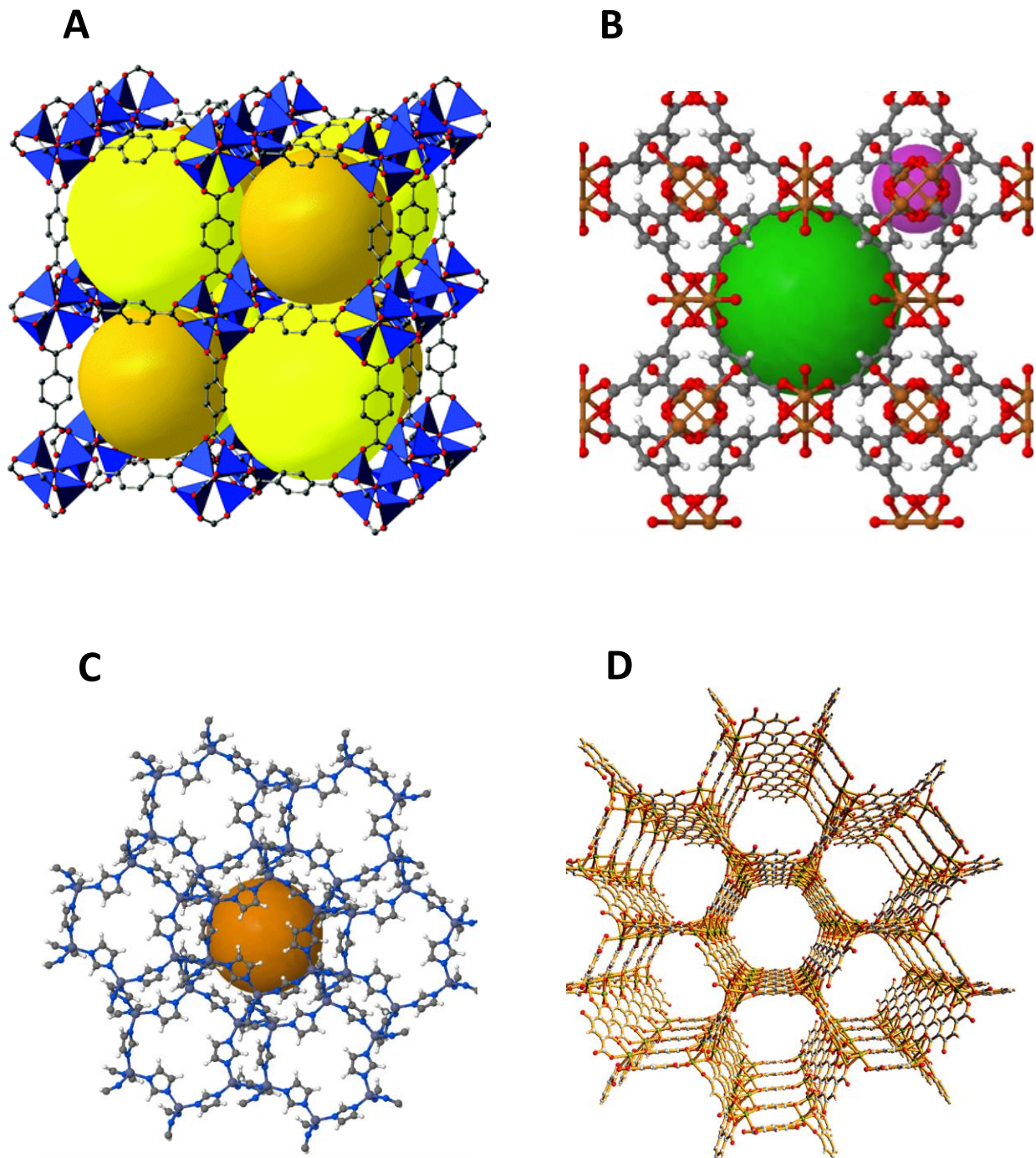
Figure 1.3: A depiction the frameworks MOF-5 (A), HKUST-1 (B), ZIF-8 (C) and M-MOF-74 (D) are shown above.[20, 25-27] Spheres are used to indicate the available volume for guests within MOF-5, HKUST-1 and ZIF-8.
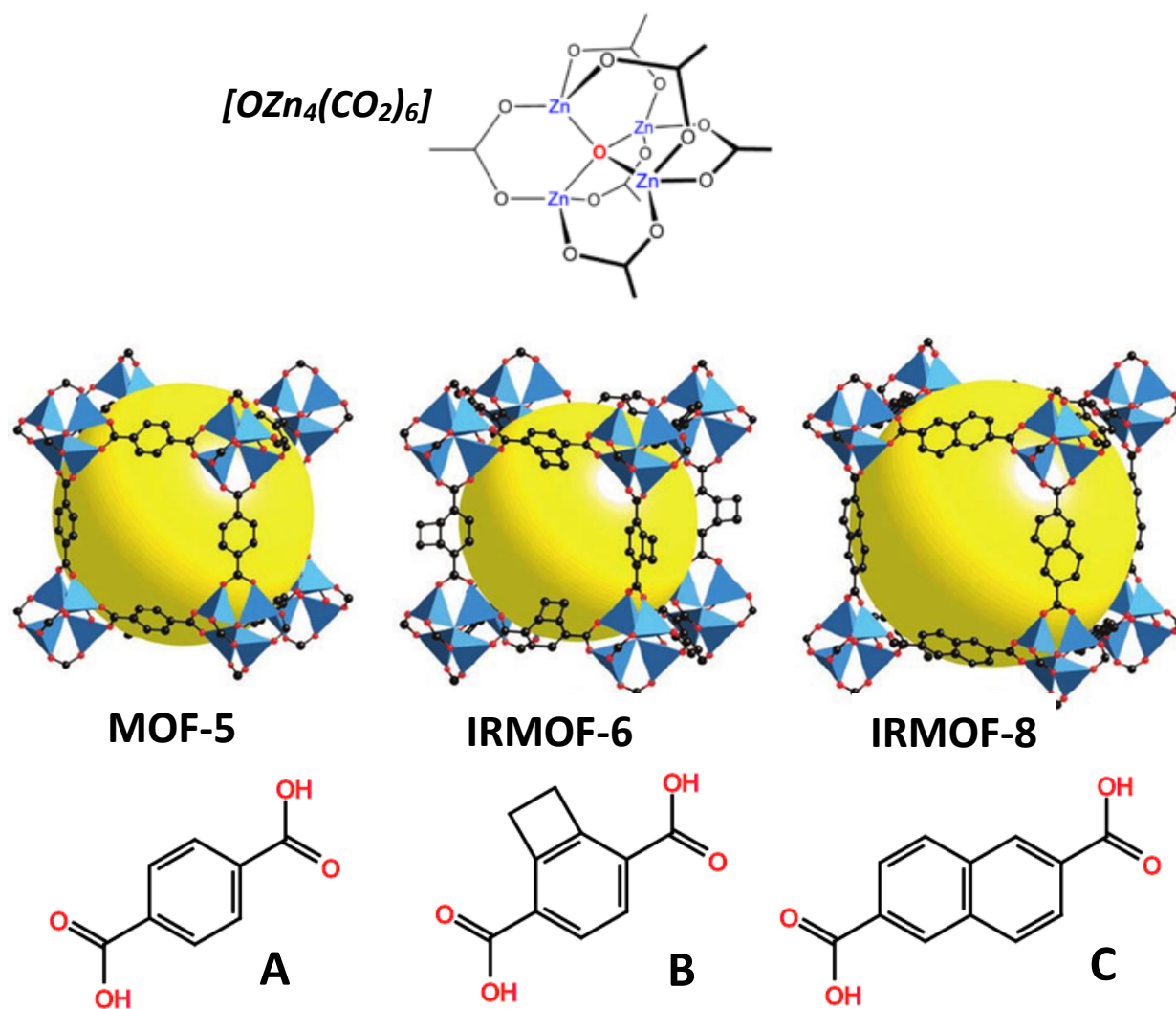
Figure 1.4: A depiction of three MOFs MOF-5, IRMOF-6 and IRMOF-8 is shown above, as reproduced from reference 25. These frameworks are composed of $[OZn_4(CO_2)_6]$ clusters and organic linkers 1,4-benzenedicarboxylate (A), cyclobutylbenzedicarboxylate (B) and 2,6-napthalenedicarboxylate (C). The structures of the linkers are shown below their respective frameworks. The yellow sphere indicates the available volume for guests within each framework.

As many MOFs are microporous materials with high surface areas and guest gas loading capacities, one of the most commonly investigated applications for MOFs is gas adsorption, including CO_2 adsorption. MOF research has been directed toward applications such as gas

purification, gas separation, gas storage and heterogeneous catalysis,[28] though other applications in electronics, optics, drug delivery, as well as chemical and radiation detection have also been explored.[29] Compared with more traditional porous solids such as zeolites and activated carbon, MOFs typically exhibit higher surface areas,[30, 31] greater flexibility, and higher tunability of their pore size and functionality through linker choice and functionalization, as depicted in Figure 1.4.[32]

The tunable nature of MOFs allows materials chemists to influence their adsorption properties. For example, after its discovery, MOF-5 was soon expanded into a large family of isoreticular MOFs,[25] labelled IRMOF-1 to IRMOF-16 to describe the linker type within the structure. Three of these IRMOFs are depicted in Figure 1.4 alongside the corresponding linker molecule. The nodes of this MOF structure are composed of four ZnO_4 tetrahedra joined by a single bridging oxygen atom to form $[OZn_4(CO_2)_6]$ clusters. Within MOF-5, these nodes are joined into a three-dimensional net by 1,4-benzenedicarboxylate (BDC) linkers, though different MOFs within this series make use of different linkers. This allows the pore size and functionality within this series to be dramatically influenced by the choice of linker. For example, when comparing the small isoreticular MOF $Zn_4O(FMA)_3$[33] with the large IRMOF-16[25], the pore volume is increased by a factor of 8. Pore size and functionality of the MOF can additionally be influenced by the reactant concentrations, temperatures, and other experimental conditions.[25]

1.1.4 Carbon dioxide adsorption in metal-organic frameworks

The high porosity and surface area of MOFs is advantageous for applications in gas adsorption and separations. Recent work has focused on using MOFs as adsorbents for toxic or greenhouse gases, such as CO_2.[34] Given the corrosiveness of alkanolamine absorbents and the high energy consumption required in the associated CO_2 absorption process, there is interest in

developing less hazardous solid adsorbent materials that can be applied to post-combustion CO_2 capture.

Table 1.1 compares the CO_2 adsorption relevant properties of some popular MOFs with traditional solid physisorbents such as Zeolite 13X and the activated carbon material NCLK3. The values for Brunauer–Emmett–Teller (BET) surface area and pore size tend to be closely correlated in porous materials.[35] Porous materials are generally designed with the goal of achieving high surface areas and pore volumes, which are associated with high CO_2 uptake.[36] The CO_2 uptake heading in Table 1.1 refer to the overall uptake of CO_2 in the framework.

Table 1.1: A summary of the CO_2 uptake and surface area of the activated carbon NCLK3, Zeolite 13X, and select MOFs is shown below. MOFs tend to possess high surface areas and CO_2 uptakes compared to other solid physisorbent materials.

Sorbent	Temp (°C)	Pressure (kPa)	CO_2 mol fraction	CO_2 uptake (mol kg^{-1})	BET Surface area (m^2 g^{-1})
NCLK3[37]	25	120	-	3.5	-
Zeolite 13X[38-40]	50	100	0.15	3	585.5
HKUST-1[41]	30	1000	0.20	8.07	1326
MIL-101(Cr)[41]	30	1000	0.20	7.19	2549
MOF-177[42]	40	100	0.15	0.65	4690
Mg-MOF-74[42]	40	100	0.15	7.5	1800
Zn-MOF-74[43]	25	3500	1	7.1	816
MIL-53(Al)[44]	30	1000	1	5	-
MIL-100(Fe)[45]	30	101.3	0.15	0.67	1894

The Mg-MOF-74 and HKUST-1 MOFs are examples of materials with particularly high CO_2 uptakes that feature strong host-guest interactions with CO_2 molecules. The strong host-guest interactions involve open metal sites of the MOF and the polar oxygen ends of guest CO_2 molecules, an example of which is shown in Figure 1.5. This strong adsorptive interaction promotes the selective adsorption of CO_2 over competing non-polar gases such as N_2, H_2 and CH_4.
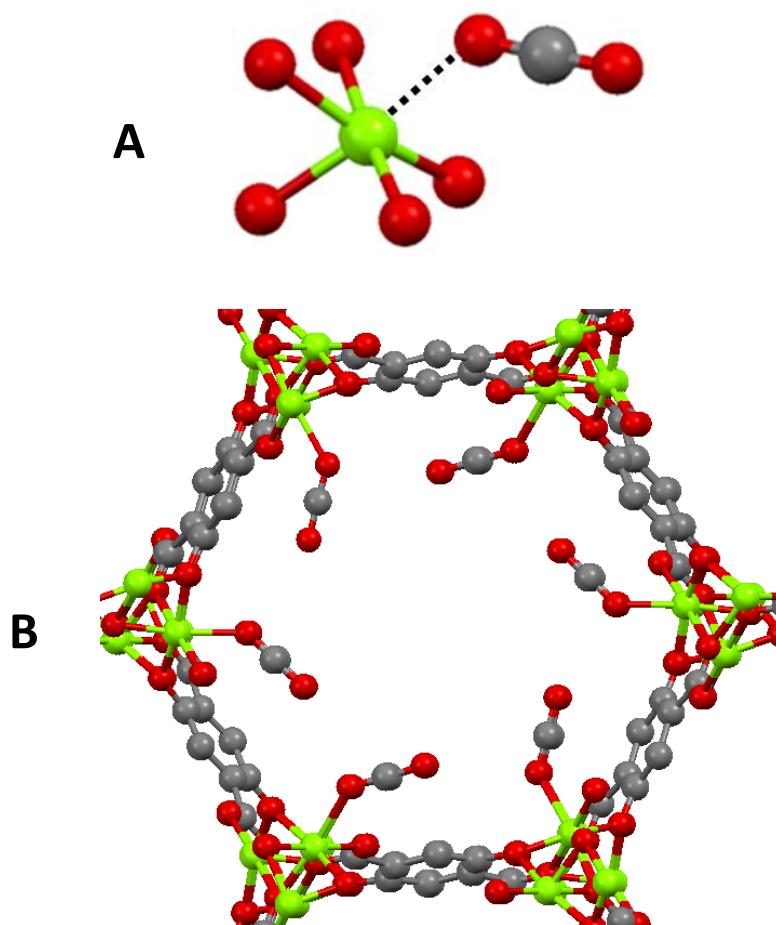
Figure 1.5: The interaction between the open metal site and the CO_2 molecule within Mg-MOF-74 is depicted above (A). In B, the hexagonal Mg-MOF-74 channel is shown saturated with CO_2 molecules (B). In this figure, the atom colours are green for Mg, grey for C and red for O.

Surface area, CO_2 uptake, selectivity against N_2 are not sufficient on their own for determining optimal CO_2 capture performance. While evaluation of these factors are common metrics for evaluating adsorbent performance, there are other criteria that must also be addressed. The required regeneration energy of the host material should be low; physisorbent materials such as MOFs tend to have lower energy requirements, as the adsorption will only weakly perturb the electronic state. Chemisorbent solid or solution materials can require regeneration temperatures exceeding 100 °C,[15, 46, 47] due to the strong detectable change in the electronic state and the higher heat of adsorption and bond strength of the adsorption interaction. Mechanical, thermal, and chemical stabilities are also issues. As such, the performance of individual frameworks and correlations between adsorption performance and host structure, pore size, and surface area must be studied and understood to rationally design improved CO_2 adsorption and CCS materials. Two characterization techniques which can yield detailed information regarding the structure and properties of solid framework samples are single crystal X-ray diffraction (SCXRD) and solid-state nuclear magnetic resonance spectroscopy (SSNMR).

1.2 Experimental Background and Techniques

1.2.1 Powder and single crystal X-ray diffraction

Powder X-ray diffraction (PXRD) is often used to identify the phase and purity of crystalline solids.[48] Monochromated X-ray radiation of a set wavelength (*e.g.*, Cu Kα radiation, λ = 1.5418 Å), when directed at a microcrystalline sample, generates a scattering pattern characteristic of the long-range ordering of the crystal structure. This allows for identification of a material by comparing an experimental PXRD pattern with a calculated or experimental reference pattern. If a high-quality PXRD pattern and sufficient complementary data is present, the structure of a material can even be solved using PXRD patterns, although this is very challenging.

One of the most reliable tools to analyze the long-range crystal structure of a framework is SCXRD. SCXRD is advantageous in that it is typically much easier to solve a structure from SCXRD data than from PXRD data.[49] In the context of MOFs, SCXRD can be used for many purposes, such as to determine the precise changes in atomic positions after guests are introduced within the pores.[50-56] Due to the framework flexibility present in many MOFs, guest adsorption can induce significant structural changes in a framework. In ideal conditions, SCXRD can even pinpoint guest molecule locations and occupancies, allowing easy visualization of the guest-host interactions that occur in a given framework. Unfortunately, without the use of powerful synchrotronic X-rays, obtaining this information requires high quality, relatively large crystals of at least 0.2 mm along two dimensions, which are capable of surviving the solvent evacuation and guest loading process. Obtaining such crystals is not always possible. In addition, locating the mobile guests using SCXRD is not easy. Performing SCXRD at low temperatures can minimize problems arising from guest dynamics, however this also limits the amount of motional information that can be obtained for guest molecules such as CO_2. Therefore, obtaining motional information regarding guest molecules is often easier achieved using alternative techniques.

1.2.2   Solid-state nuclear magnetic resonance spectroscopy

SSNMR is a technique primarily used to examine the properties of nuclei in powder samples. Most nuclei have a spin, and a corresponding nuclear spin magnetic moment. Nuclear spins experience several distinct interactions within an external magnetic field, notably the Zeeman interaction, dipolar interaction, chemical shift interaction, J-coupling interaction and quadrupolar interaction.[57] The Zeeman interaction is the strongest interaction, shown in Table 1.2,[58] with other interactions acting as perturbations on the Zeeman interaction. The Zeeman interaction refers to the interaction between the magnetic moment of the nuclear spin with the external magnetic field.

Table 1.2*: An estimate of the magnitudes of typical nuclear spin interactions is shown below.*[58]

Interaction	Magnitude in solids (Hz)
Zeeman	10^7-10^9
Chemical shift	10^2-10^5
Dipolar	10^3-10^5
J-coupling	10^0-10^3
Quadrupolar	10^3-10^7

The different spin states of a nucleus are degenerate in the absence of a magnetic field; when a strong external magnetic field is applied, the nuclear spin energies lose their degeneracy and split into $2I + 1$ non-equivalent energy levels, where *I* is the nuclear spin. The value of the nuclear spin is determined by the number of protons and neutrons within a specific nucleus. The magnitude of the splitting between spin energy levels (ΔE) is proportional to the nuclear gyromagnetic ratio γ and the external magnetic field strength B_0, as given in equation *(1)* where *h* is Planck's constant. The gyromagnetic ratio is a particle dependant property describing the ratio of the magnetic moment to the angular momentum of a given particle within a magnetic field, with units of rad s^{-1} T^{-1}.

$$\Delta E = h\gamma B_0/2\pi \qquad\qquad (1)$$

An example of this splitting in a spin 1/2 nucleus is shown in Figure 1.6. The splitting of the energy levels is necessary to conduct nuclear magnetic resonance spectroscopy experiments.

When placed in a magnetic field, such as the one associated with an NMR spectrometer, the nuclear magnetic moments within a sample will align either parallel or antiparallel to the applied magnetic field (B_0), with the Zeeman interaction in a spin 1/2 nucleus causing a splitting in energy between the two spin states.[57] The nuclear magnetic moments will precess parallel or

antiparallel to B_0 at a Larmor frequency, which is dependant on the identity of the nuclear isotope and its corresponding gyromagnetic ratio, as well as the strength of B_0. The majority of spins will align parallel to B_0, in the 1/2 energy level shown in Figure 1.6, while a minority will align antiparallel to B_0, in the -1/2 energy level.
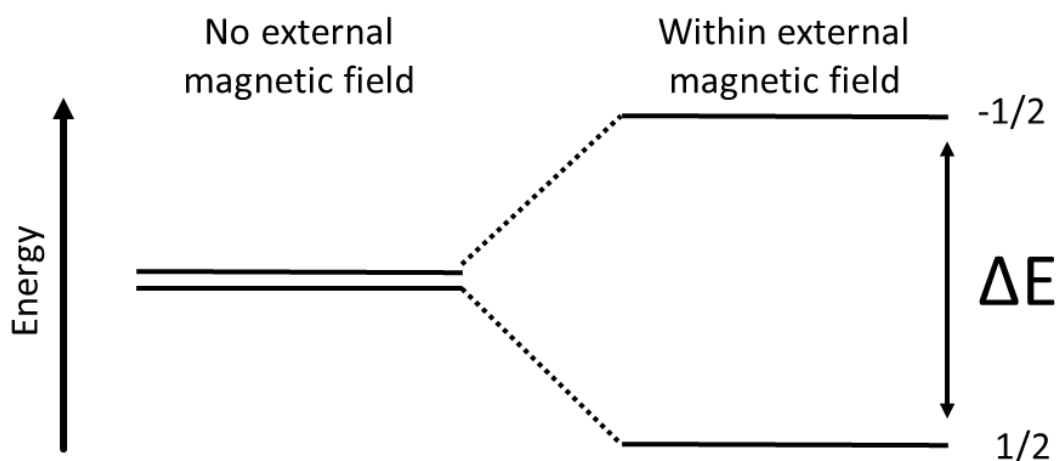
Figure 1.6: The energy level splitting caused by the Zeeman interaction of a spin 1/2 nuclei is depicted above.

Using an NMR coil, radiofrequency (rf) pulses are applied at the Larmor frequency, generating an additional magnetic field and causing spins to transition to the higher energy, antiparallel orientation. This changes the net magnetization of the system. After this secondary magnetic field is switched off, the precession of spin magnetism back to parallel with B_0 can induce an electric current in the NMR coil surrounding the sample, allowing for characterization of the magnetic shielding.[57]

1.2.3   Chemical shift and chemical shielding

The presence of electrons produces local magnetic fields, which will circulate in an externally applied magnetic field B_0, and the circulation of electrons generates local magnetic fields that act to shield or deshield the nuclei from B_0. This chemical shielding produces small deviations in the magnetic shielding of the nucleus, which is characteristic of specific chemical environments and local coordination geometries.[57] The chemical shielding can be modelled by a second rank tensor known as the chemical shielding tensor.[59] Only the symmetric portions of this tensor (σ_{11}, σ_{22} and σ_{33}, defined such that $\sigma_{11} \leq \sigma_{22} \leq \sigma_{33}$) make observable contributions to the NMR spectra, with the corresponding diagonalized matrix representation of the tensor given in equation *(2)*.

$$\ddot{\sigma} = \begin{pmatrix} \sigma_{11} & 0 & 0 \\ 0 & \sigma_{22} & 0 \\ 0 & 0 & \sigma_{33} \end{pmatrix} \qquad (2)$$

Measurements from NMR spectra are typically reported in field-independent chemical shift (CS) values measured in ppm, which compare an experimental resonant frequency with that of a known reference compound and can be compared no matter the strength of B_0 employed. The conversion of a chemical shielding σ to a CS δ is shown in equation *(3)*.

$$\delta = \frac{\sigma_{ref} - \sigma}{1 - \sigma_{ref}} \times 10^6 \qquad (3)$$

The CS is modelled by its own CS tensor related directly to the chemical shielding tensor, with components δ_{11}, δ_{22} and δ_{33}.[59] The diagonalized matrix representation of the tensor is shown below as equation *(4)*. The average of these three components is the isotropic chemical shift, δ_{iso}.

$$\overset{\bm{\cdot\cdot}}{\delta} = \begin{pmatrix} \delta_{11} & 0 & 0 \\ 0 & \delta_{22} & 0 \\ 0 & 0 & \delta_{33} \end{pmatrix} \qquad (4)$$
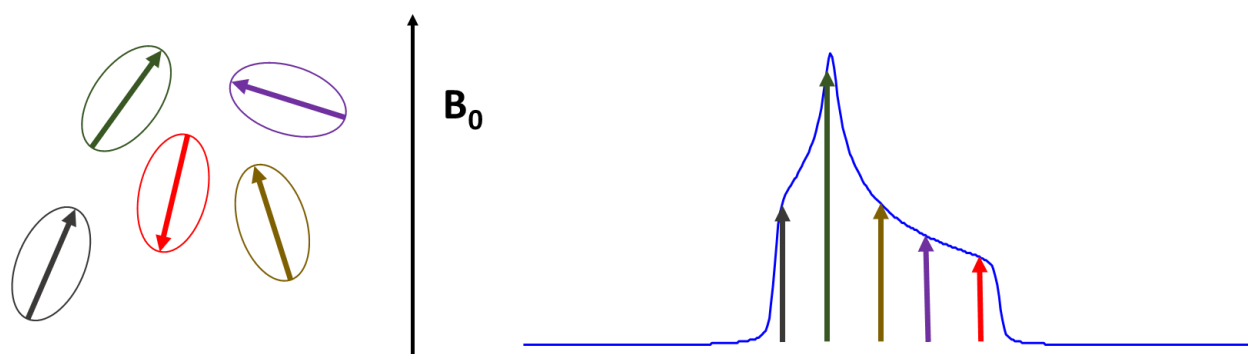
Figure 1.7: Above, the anisotropy of individual crystallites orients the shielding tensor in random directions relative to the applied magnetic field B_0 is depicted on the left. This leads to a broad NMR powder pattern shown on the right.

Solid SSNMR samples consist of many crystallites, which assume all possible spatial orientations with respect to the magnetic field. As nuclear spin interactions are heavily dependant on the orientation of the corresponding interaction tensor with respect to B_0, each crystallite orientation corresponds to slightly different SSNMR resonant frequency.[59] This means that SSNMR spectra of powdered solid samples consist of broad lines or powder patterns arising from the slightly different resonant frequency of each crystallite orientation, as depicted in Figure 1.7. This is called chemical shift anisotropy (CSA),[57, 59] and the correspondingly broad powder patterns limits the resolution in static SSNMR and makes it difficult to distinguish multiple inequivalent nuclear sites. However, CSA-dominated powder patterns yield useful information regarding the CS tensor. The CS interaction and corresponding powder pattern can be discussed in terms of

isotropic CS, span, and skew, which are defined in relation to the CS tensor parameters as shown

in equations *(5)*, *(6)* and *(7)*.

Isotropic CS:
$$\delta_{iso} = \frac{\delta_{11}+\delta_{22}+\delta_{33}}{3}$$
(5)

Span:
$$\Omega = \delta_{11} - \delta_{33}$$
(6)

Skew:
$$\kappa = \frac{3(\delta_{22}-\delta_{iso})}{\Omega}$$
(7)

These three parameters produce characteristic effects on the SSNMR powder pattern. Their

effects can be observed in Figure 1.8.
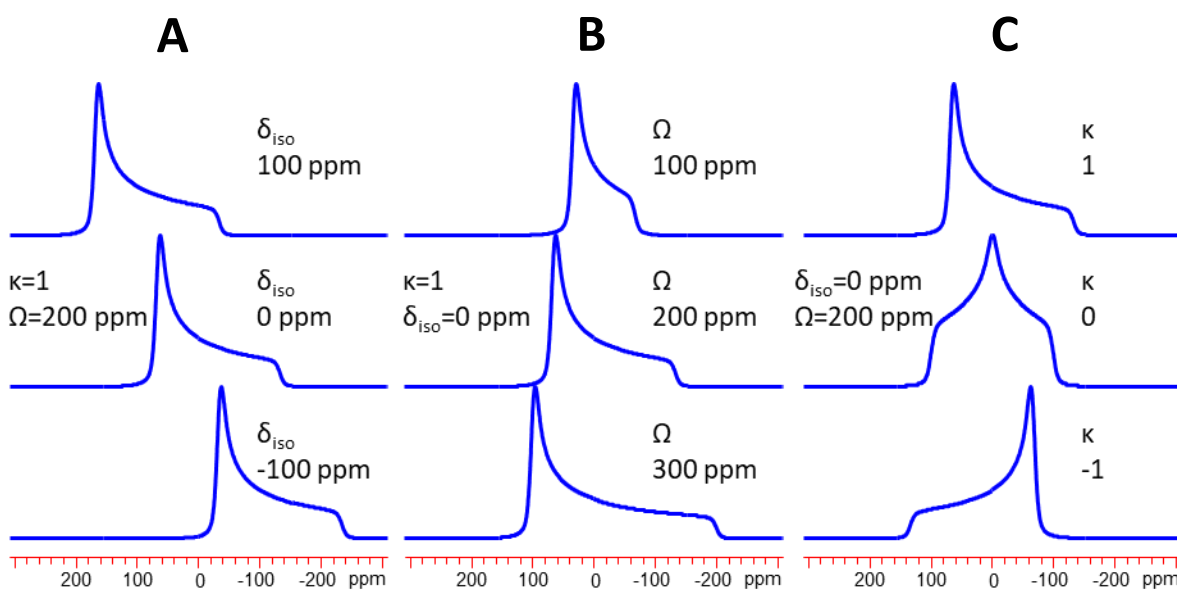
Figure 1.8: The effects of δ_{iso} (A), Ω (B) and κ (C) on the shape of a SSNMR powder pattern are shown above.
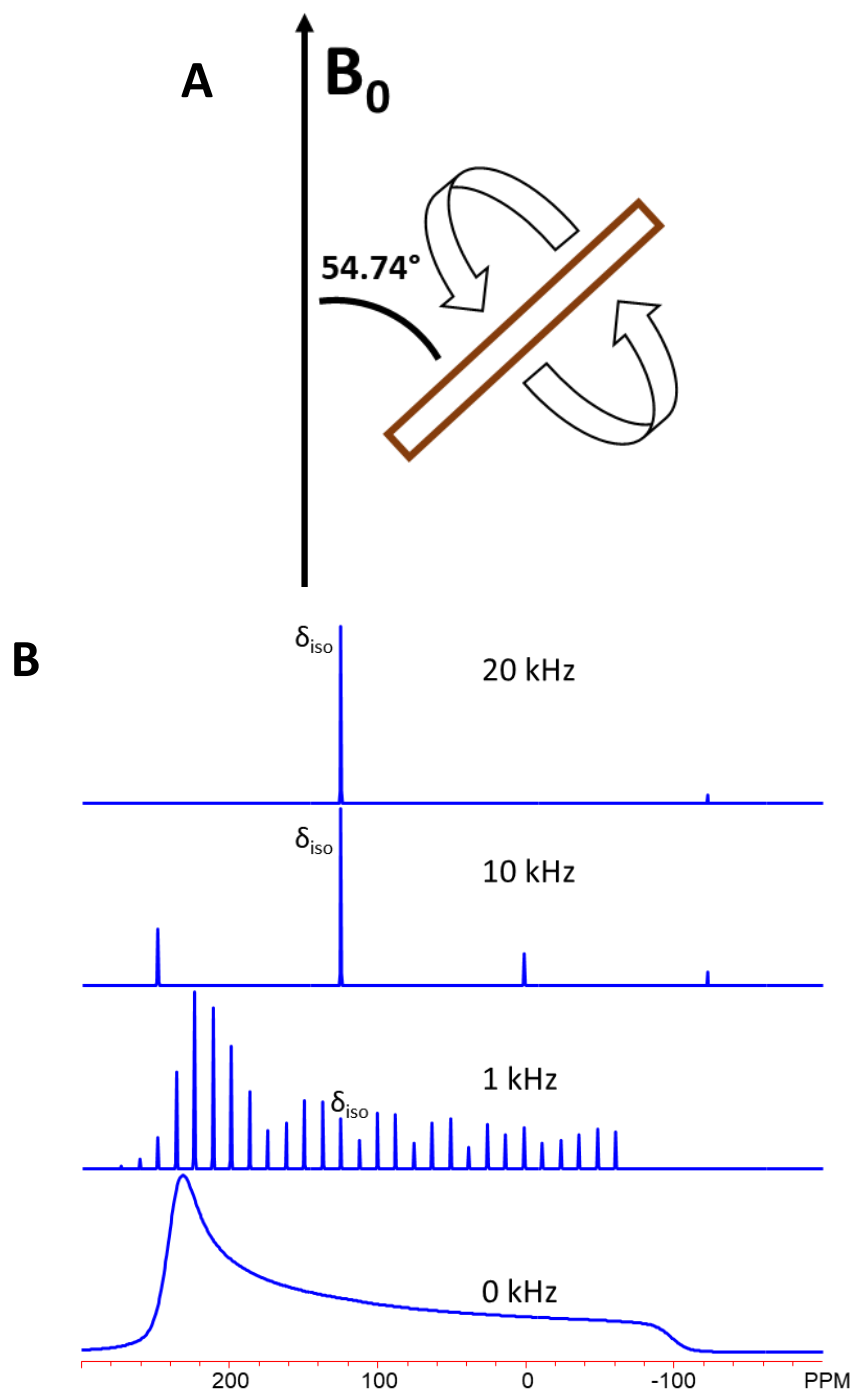
Figure 1.9: A depiction of a rotating MAS SSNMR sample is shown above (A). WSolids[60] simulations are used to demonstrate the effect of MAS on the ^{13}C SSNMR spectra of CO_2 (B). While the frequency and intensity of spinning sidebands changes, the frequency of the δ_{iso} resonance is unchanged regardless of spinning speed.

One of the most widely used techniques in SSNMR is magic-angle spinning (MAS). MAS removes the effects of CSA, and assists in the removal of dipolar and quadrupolar coupling effects, which will be mentioned below. Effectively, MAS at a sufficiently high spinning rate compared to the span of the CS tensor will narrow the NMR powder pattern to one or several sharp resonances.[59] This is due to the orientation dependence of the nuclear spin interaction containing the mathematical term $[3\cos^2(\theta) - 1]$ where θ is the angle of the interaction tensor with respect to the applied magnetic field.

If the sample is spun at an angle of 54.74° (the magic-angle) with respect to the applied magnetic field $[3\cos^2(\theta) - 1]$ equals zero, and the interaction anisotropies of the sample average to zero.[57, 59] This averages the anisotropic powder pattern to a single narrow resonance located at the isotropic chemical shift. Slower spinning rates will produce spinning sidebands observed at set intervals along the spectra. These intervals are equal to the spinning rate of the sample.[59] Nuclei with larger CSAs and correspondingly broad powder patterns require very high spinning rates to completely remove the presence of spinning sidebands. The rotor position in a MAS experiment and the effect of spinning speed on spinning sidebands is depicted in Figure 1.9.

1.2.4 Examining dipolar interactions with SSNMR

Another technique employed in SSNMR is cross-polarization (CP), typically to assist in observing dilute or lower frequency spins such as ^{13}C, which has only a 1% natural abundance. CP allows a dilute nucleus S to be spin-polarized by a nearby network of abundant spins I, such as ^{1}H.[59, 61] A basic example of a CP pulse sequence is shown in Figure 1.10. CP requires the Hartmann-Hahn match condition to be satisfied.[59, 61] This depends on the gyromagnetic ratio γ of the type of nuclei involved, and the applied rf fields B, as shown in equation *(8)*.

$$\gamma_S B_S = \gamma_I B_I \qquad\qquad (8)$$

A satisfied Hartmann-Hahn match condition allows spin polarization of the abundant nucleus *I* to be partially transferred to the dilute nucleus *S*. Contact pulses are applied for a duration of time known as the contact time (CT), during which time spin polarization is transferred between the two nuclear spins.[59, 61]
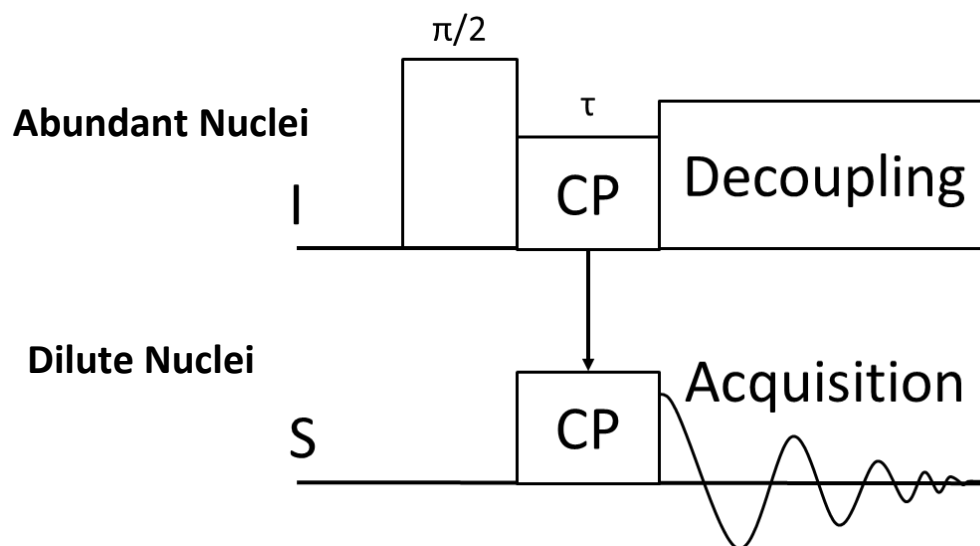
Figure 1.10: The pulse sequence for CP of spin I to spin S is shown above. τ is the contact time used. A π/2 pulse flips the net magnetization by 90°, before CP is used to transfer magnetization between nuclei.

CP experiments are mediated by the dipolar coupling between the two nuclei involved. By extension, the experiments are dependent on the internuclear distance between the two nuclei by a factor of r^{-3}.[59] This can be seen in equation *(9)*, where μ_0 is the permeability of a vacuum and *D* is the dipolar coupling constant quantifying the strength of the dipolar interaction.

$$D = \frac{\mu_0}{4\pi} \frac{\gamma_I \gamma_S}{r_{IS}^3} \frac{h}{2\pi} \qquad (9)$$

The CT used in a CP experiment describes the amount of time that CP is allowed to occur. By using a longer CT, polarization can occur across greater internuclear distances. This allows CP

experiments to be used as a means of judging the dipolar coupling strength and the distances between different nuclei, such as guest nuclei and framework nuclei.[62] Longer CTs will eventually cause a decrease in resonance intensity, due to magnetization relaxation occurring during the magnetization transfer. This relaxation will reduce the observed signal intensity, eventually reducing intensity more than the CT enhances it. This relaxation is governed by the time T_{1p}.[59] A stronger dipolar interaction between nuclei means that the resonance will peak in intensity at low CTs. A weaker interaction requires longer CTs to observe the signal enhancement from the magnetization transfer.

Rotational-echo double resonance (REDOR) experiments are another means of assessing the strength of the dipolar interaction between nuclei.[59, 63] An initial 90° excitation pulse is applied to a spin I, and then a series of rotor synchronized 180° dephasing rf pulses are applied to another spin S. This results in a spectrum S_r with reduced signal for the observed nucleus I.[59, 63] The dephased spectrum is compared to a control spectrum S_0 generated by omitting the dephasing pulses. The difference between the control and dephased spectra is ΔS, which allows for determination of the strength of the dipolar interaction between I and S. Spectra are collected for several different dephasing times, which are all a multiple of twice the rotor period. The magnitude of the dephasing effect varies in a predictable manner depending on the dephasing time and the strength of the dipolar interaction.[63]

A more detailed picture of internuclear interactions and connectivity can be obtained by employing two-dimensional heteronuclear correlation (HETCOR) NMR experiments. These can be imagined as a two-dimensional version of CP experiments. In two-dimensional NMR, a multiple pulse one-dimensional experiment is repeated many times with a systematic variation of

the delay time t_d, and then the stacked results are plotted.[57] Frequency-switched-Lee-Goldburg (FSLG) HETCOR experiments can be used to probe the connectivity between spins I and S.[64-66]
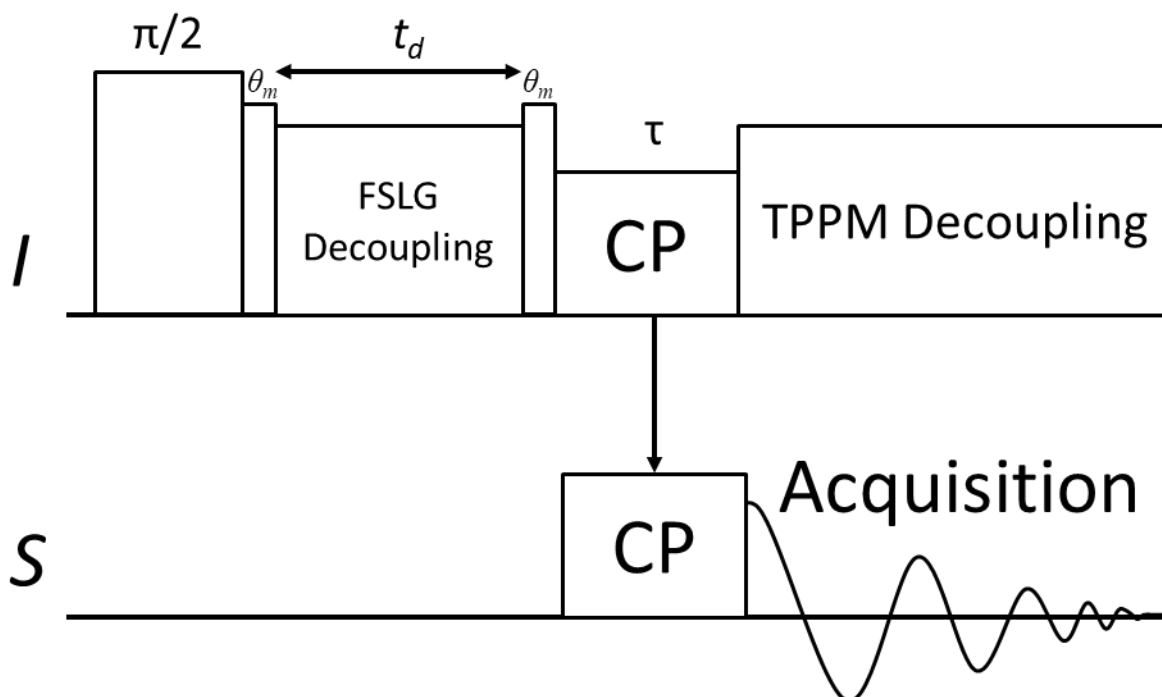
Figure 1.11: *The FSLG-HETCOR pulse sequence for correlating spin I to spin S is shown above. t_d is the delay time varied. θ_m pulses are used to align I magnetization at the magic angle with respect to B_0.*

An example of an FSLG-HETCOR pulse sequence is shown in Figure 1.11. After an initial $\pi/2$ pulse, the magnetization of I evolves over t_d, with the final magnetization dependent on the chemical shift of the I nucleus. During this time, I magnetization is aligned with the magic angle using θ pulses and subjected to FSLG homonuclear decoupling.[64] The I magnetization is then transferred into S magnetization using CP, before heteronuclear two pulse phase modulation (TPPM) decoupling is used.[67] As t_d is varied, the intensity of the NMR signals varies as a function of the delay time and the I-S dipolar coupling constant. As the experiment is repeated for many

values of t_d, a stack is obtained containing both I and S chemical shift information for all $I - S$ pairs in the molecule. A Fourier transformation in both dimensions then generates a plot correlating different I and S spins to one another, as indicated by cross peaks.[57] Using low CTs prevents correlation between more distant spins.

1.2.5   Examining the quadrupolar interaction with SSNMR

Quadrupolar nuclei with a spin greater than 1/2 will possess an asymmetric charge distribution, approximated by the illustration in Figure 1.12. These quadrupolar nuclei will couple to the electric field gradient (EFG) surrounding the nuclei, influencing spin energy levels and the resulting NMR spectra.[57] This interaction is the quadrupolar interaction (QI). Quadrupolar nuclei will split into three or more spin states within B_0, with the QI affecting all spin energy levels. The difference between +1/2 and -1/2 spin states (known as the central transition), is perturbed only by second order quadrupolar effects, and therefore this is what is observed in SSNMR experiments.
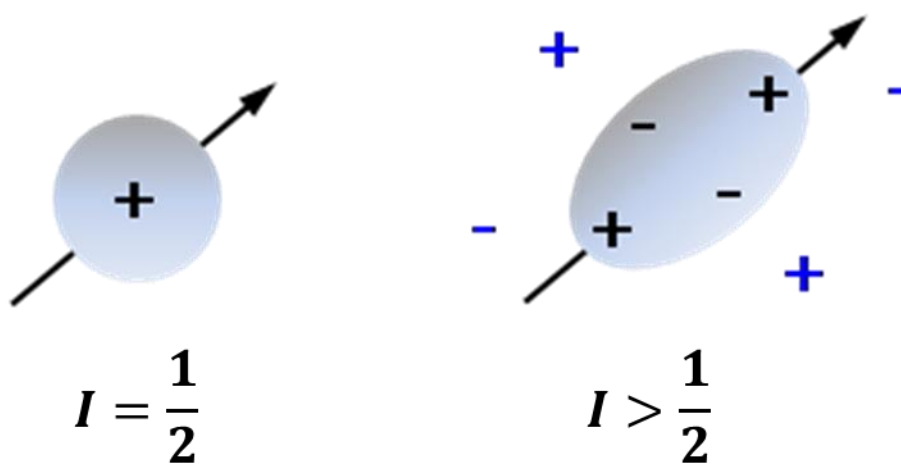
Figure 1.12: An approximation of a spin 1/2 nuclei and a quadrupolar nuclei is depicted above. Quadrupolar nuclei possess an asymmetric distribution of positive charge, and will couple to the EFG about the nucleus. This interaction is highly dependent on the local distribution of charges and the local electronic environment. This image was reproduced from reference 68.

Like the CS interaction, the QI can be described by a second rank tensor with three principal components, V_{11}, V_{22} and V_{33}, ordered such that $V_{11} \leq V_{22} \leq V_{33}$. In SSNMR spectra, the EFG tensor can be defined by two parameters, the quadrupolar coupling constant (C_Q) and the asymmetry parameter (η_Q), defined in equations *(10)* and *(11)*.[57] Changes in these parameters will produce well-defined effects on a SSNMR powder pattern, allowing these values to be determined from experimental spectra.

$$C_Q = \frac{eQV_{33}}{\hbar} \qquad (10)$$

$$\eta_Q = \frac{V_{11} - V_{22}}{V_{33}} \qquad (11)$$

The C_Q value describes the magnitude of the QI, and is dependant on V_{33}, the component of the EFG with the greatest magnitude. The magnitude of the C_Q is correlated with the spherical symmetry about the quadrupolar nuclei, with a smaller C_Q suggesting greater spherical symmetry. A perfectly symmetrical environment will produce a C_Q of zero, as there will be no QI. While C_Q can be a positive or negative value, NMR experiments can only determine its magnitude.
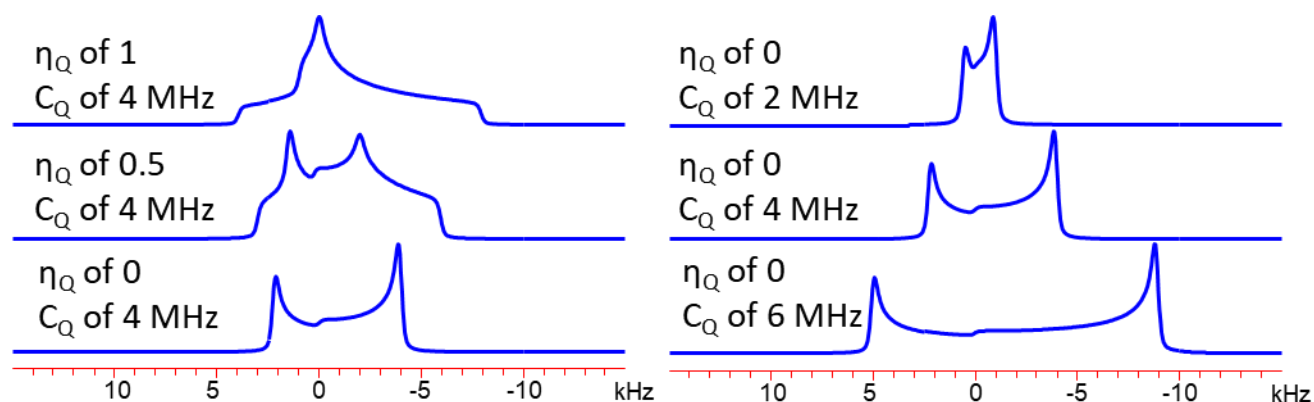
Figure 1.13: The effects of C_Q and η_Q on a theoretical static ^{67}Zn SSNMR powder pattern of the central transition at 21.1 T are shown above. The simulations were performed using WSolids.[60]

The η_Q is dependent on V_{11}, V_{22} and V_{33}, and varies between 0 and 1. If V_{11} and V_{22} are equal, the η_Q is zero, and V_{33} must coincide with a $\geq C_3$ axis of symmetry. The η_Q value therefore conveys information about the axial symmetry of the EFG about the quadrupolar nuclei, and by extension the chemical environment about the nucleus, with a lower value suggesting greater axial symmetry. Changes in C_Q affect the breadth of the powder pattern, while changes in η_Q affect both the pattern's breadth and position of the characteristic powder pattern "horns." This effect is illustrated in Figure 1.13.

1.2.6 SSNMR of MOFs

SSNMR experiments have been employed on MOFs to examine both the guest, linker, and metal nuclei, allowing for estimates of framework-adsorbate interactions, predictions on the number and location of adsorption sites, and understanding the detailed motional behaviour of adsorbed molecules.[69]

When adsorbed inside a MOF, guest molecules such as CO_2 exhibit restricted motional behaviour. This produces predictable averaging of the ^{13}C CSA of the $^{13}CO_2$ powder pattern, since the CSA parameters for solid CO_2 are known.[70] The effects on the powder pattern vary with the types, rates, and angles of motion occurring. One common type of CO_2 motion in MOFs is a temperature dependant combination of rotational wobbling upon an adsorption site along with hopping between adjacent adsorption sites,[56, 62, 71, 72] depicted in Figure 1.14. This manifests in changes to the span and skew of the ^{13}C SSNMR powder pattern. The effects of these motions on the powder pattern are shown in Figure 1.15. The SSNMR powder pattern of Solid CO_2 has a Ω of 335 ppm and a κ of 1.[70] In the Matériaux de l′Institut Lavoisier-53(Al) MOF, or MIL-53(Al), the Ω has decreased to 246 ppm and the κ to 0.78 at 293 K.[62] In the PbSDB MOF, named for its

lead metal centres and 4,4'-sulfonyldibenzoic acid linkers, the motional angles of adsorbed CO_2 are even greater, and the Ω and κ are 115 ppm and 0.55 respectively.[56] ^{13}C SSNMR is therefore a very useful tool for assessing the behaviour of CO_2 within framework pores.
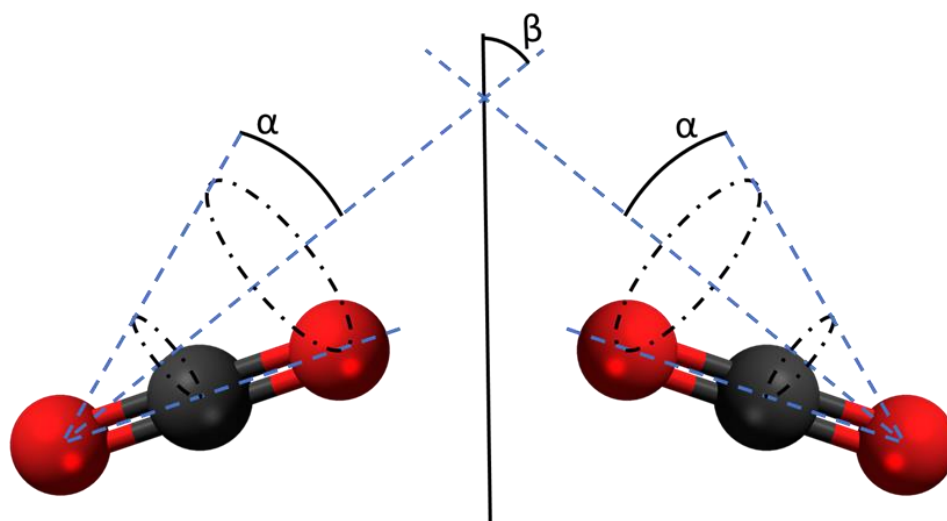
Figure 1.14: The wobbling and hopping motions of a CO_2 molecule are shown above, described by the α and β angles respectively.

As CP NMR is dependent on the strength of the dipolar interaction, CP SSNMR offers a means of examining the interactions between guest molecules and framework nuclei as adsorption occurs. For example, in MIL-53(Al), [1]H-^{13}C MAS CP spectra were able to reveal how signals corresponding to carboxyl groups were affected by the presence of water molecules in the framework, highlighting the interactions between the guest and the linker.[73] Static [1]H-^{13}C CP experiments were used to explore the interaction between CO_2 and the MIL-53(Ga) and MIL-53(Al) frameworks, with differences in relative CP enhancements suggesting a weaker guest-host interaction in MIL-53(Ga) than in MIL-53(Al). CP spectra of deuterated MIL-53 was also used to

help identify the binding site, suggesting that it was close to the bridging hydroxyl groups in the MOF.[73]
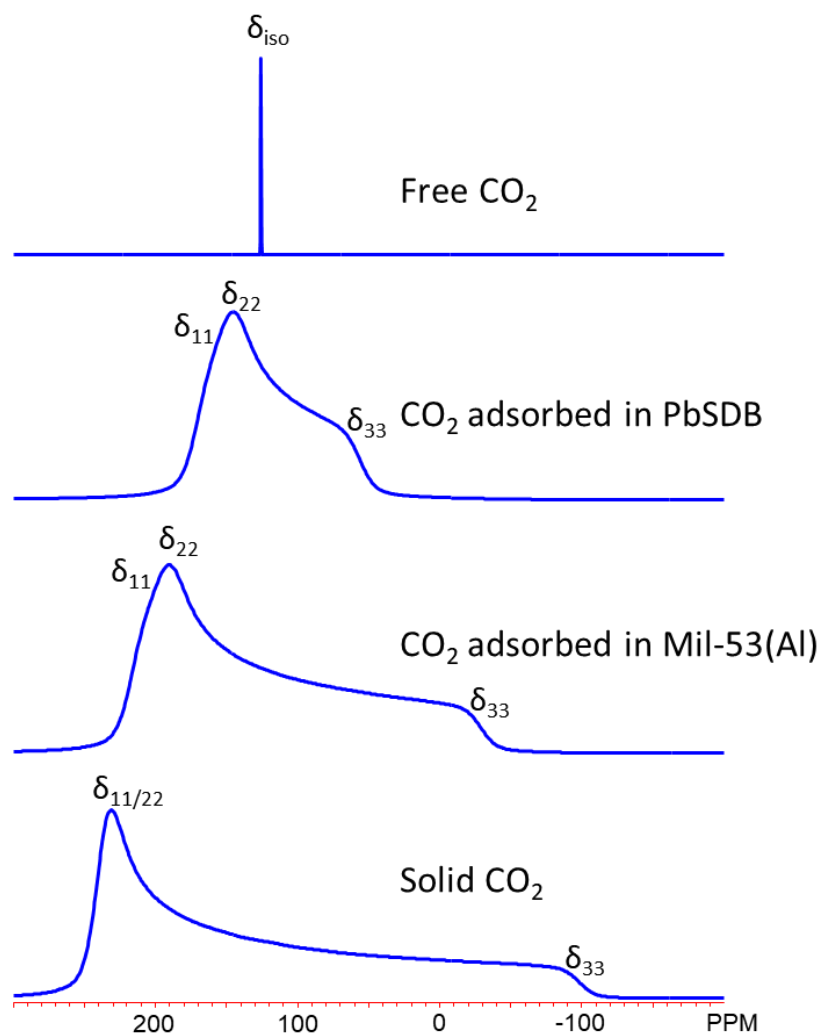
Figure 1.15: WSolids[60] simulated spectra performed using experimental δ values are shown above, depicting the effects of CSA on the ¹³C NMR spectra of CO₂ at 293 K. In PbSDB, the CO₂ wobbles about a 38° angle and hops between sites at a 25° angle, with the resulting motional averaging narrowing the powder pattern.[56] Within Mil-53(Al), the motional angles are only 19°, and the resulting powder pattern is broader and more skewed.[62]

While ^{13}C is a spin 1/2 nucleus, many of the metal centers within MOFs are quadrupolar. SSNMR of the metal centers in MOFs can help identify changes in the EFG about the metal center, and thus hint at changes in the chemical environment about the metal centre. However, many of these centers, such as ^{67}Zn, ^{25}Mg or ^{91}Zr, possess high quadrupole moments, low magnetic moments, and/or low natural abundances, and therefore necessitate the use of strong external magnetic fields or large sample volumes; these nuclei have not been studied as extensively as more receptive quadrupoles such as ^7Li and ^{23}Na. The first characterization of ^{67}Zn environments in MOFs was for MOF-5, one of the most widely studied MOFs.[74-76] This was done using an ultrahigh magnetic field of 21.1 T.

SSNMR of quadrupolar nuclei also allows for the verification of structural models and identification of the number and local symmetry of unique metal sites.[74-79] C_Q and η_Q values can be determined computationally and the measured and calculated parameters compared to assess the quality of proposed models. Quadrupolar NMR can also be performed on guest molecules such as D_2 and D_2O, as well as on the framework nuclei. The motional behaviour of water in a zinc trimesate framework was examined using ^2H NMR, where it was found that coordinated D_2O exhibited a well defined quadrupolar pattern above temperatures of 100 °C.[80] In M-MOF-74, ^2H NMR was used to show the specific type of metal center strongly influenced the water adsorption behaviour of the MOF, with Mg-MOF-74 producing broad ^2H spectra, while Zn-MOF-74 spectra consisted of a broad and narrow component.[81] The spectra also demonstrated the effects of temperature on the D_2O motions, with the Mg-MOF-74 spectra producing resonances characteristic of slower motional rates as the temperature was decreased to 153 K.

1.3   Thesis Outline

Increasing atmospheric CO_2 concentrations and global temperatures will require a variety of technologies to minimize or curb these effects. Capture of CO_2 gas using solid porous materials can be readily applied to existing CO_2 point sources, and is less energy intensive and less damaging to equipment than aqueous amine alternatives. MOFs, as a class of tunable porous materials and strong CO_2 adsorbents, are well-suited as potential CO_2 capture materials. It is beneficial to understand the interactions between CO_2 and different MOF materials; by elucidating the links between CO_2 adsorption, CO_2 motion, and MOF structural features, better and more efficient solid CO_2 adsorbent MOFs can be designed.

SCXRD and SSNMR can offer insight on the long- and short-range structure of MOFs. Where possible SCXRD can be applied to precisely determine MOF structural changes with temperature and guest loading. SSNMR can be used to gain insight into the local environment of target nuclei and guest-host interactions that occur inside a framework. CP, REDOR, and HETCOR specifically can gauge the strength of the dipolar interactions and establish connectivity between nuclei. NMR of quadrupolar metal centres can determine changes in the EFG, which will be affected by metal guest interactions which change as guests are evacuated or loaded into the framework.

This thesis will focus on the use of XRD and SSNMR techniques to examine the previously reported ultramicroporous frameworks SIFSIX-3-Zn[82] and ZnAtzOx.[83] While these frameworks lack open metal sites to serve as strong adsorption sites for carbon dioxide, both frameworks are known to have unusually high adsorption selectivity for CO_2 over gases such as N_2, H_2 and CH_4. These characteristics are believed to be due to the strong electrostatic interactions between the framework walls and the carbon dioxide molecule, enhanced by the ultramicroporous nature of the pores. This makes both frameworks valuable subjects for study when trying to better understand

CO₂ adsorption in solid frameworks. Using the techniques outlined above, a more complete understanding of the guest-host interactions within these frameworks has been developed.

1.4   References

1.   Monastersky, R., Global carbon dioxide levels near worrisome milestone. *Nature* **2013,** *497* (7447), 13-14.

2.   Falkowski, P.; Scholes, R. J.; Boyle, E.; Canadell, J.; Canfield, D.; Elser, J.; Gruber, N.; Hibbard, K.; Hogberg, P.; Linder, S.; Mackenzie, F. T.; Moore, B.; Pedersen, T.; Rosenthal, Y.; Seitzinger, S.; Smetacek, V.; Steffen, W., The global carbon cycle: A test of our knowledge of earth as a system. *Science* **2000,** *290* (5490), 291-296.

3.   IPCC, *Climate Change 2013: The Physical Science Basis. Contribution of Working Group I to the Fifth Assessment Report of the Intergovernmental Panel on Climate Change*. Cambridge University Press: Cambridge, United Kingdom and New York, NY, USA, 2013; p 1535.

4.   IPCC, *IPCC, 2014: Climate Change 2014: Synthesis Report. Contribution of Working Groups I, II and III to the Fifth Assessment Report of the Intergovernmental Panel on Climate Change*. IPCC: Geneva, Switzerland, 2014; p 151.

5.   Olivier, J. G. J.; Janssens-Maenhout, G.; Muntean, M.; Peters, J. A. H. W., Trends in global CO₂ emissions: 2016 Report. PBL Netherlands Environmental Assessment Agency: The Hague, 2016; p 86.

6.   IPCC, *Carbon Dioxide Capture and Storage: A Special Report of Working Group III of the Intergovernmental Panel on   Climate Change*. Cambridge, United Kingdom and New York, NY, USA   2005.

7.   IPCC, *Climate Change 2014: Mitigation of Climate Change.   Contribution of Working Group III to the Fifth Assessment Report of the   Intergovernmental Panel on Climate Change*. Cambridge University Press: Cambridge, U.K. and New York, 2014.

8.   NOAA Earth System Research Laboratory, Trends in Atmospheric Carbon Dioxide. http://www.esrl.noaa.gov/gmd/ccgg/trends/index.html (accessed September 20).

9.   Goeppert, A.; Czaun, M.; Prakash, G. K. S.; Olah, G. A., Air as the renewable carbon source of the future: an overview of CO2 capture from the atmosphere. *Energy & Environmental Science* **2012,** *5* (7), 7833-7853.

10.   IPCC, *Carbon Dioxide Capture and Storage: A Special Report of Working Group III of the Intergovernmental Panel on   Climate Change*. Cambridge, United Kingdom and New York, NY, USA   2005.

11.   Pires, J. C. M.; Martins, F. G.; Alvim-Ferraz, M. C. M.; Simoes, M., Recent developments on carbon capture and storage: An overview. *Chemical Engineering Research & Design* **2011,** *89* (9), 1446-1460.

12.   Sanz-Perez, E. S.; Murdock, C. R.; Didas, S. A.; Jones, C. W., Direct Capture of CO₂ from Ambient Air. *Chemical Reviews* **2016,** *116* (19), 11840-11876.

13.   Rochelle, G. T., Amine Scrubbing for CO2 Capture. *Science* **2009,** *325* (5948), 1652-1654.

14.   Shakerian, F.; Kim, K. H.; Szulejko, J. E.; Park, J. W., A comparative review between amines and ammonia as sorptive media for post-combustion CO2 capture. *Applied Energy* **2015,** *148*, 10-22.

15.   Knudsen, J. N.; Jensen, J. N.; Vilhelmsen, P. J.; Biede, O., Experience with CO(2) capture from coal flue gas in pilot-scale: Testing of different amine solvents. *Greenhouse Gas Control Technologies 9* **2009,** *1* (1), 783-790.

16.   Yaghi, O. M.; Li, H. L., HYDROTHERMAL SYNTHESIS OF A METAL-ORGANIC FRAMEWORK CONTAINING LARGE RECTANGULAR CHANNELS. *Journal of the American Chemical Society* **1995,** *117* (41), 10401-10402.

17.   Li, H.; Eddaoudi, M.; O'Keeffe, M.; Yaghi, O. M., Design and synthesis of an exceptionally stable and highly porous metal-organic framework. *Nature* **1999,** *402* (6759), 276-279.

18.   Batten, S. R.; Champness, N. R.; Chen, X. M.; Garcia-Martinez, J.; Kitagawa, S.; Ohrstrom, L.; O'Keeffe, M.; Suh, M. P.; Reedijk, J., Terminology of metal-organic frameworks and coordination polymers (IUPAC Recommendations 2013). *Pure and Applied Chemistry* **2013,** *85* (8), 1715-1724.

19.   Park, K. S.; Ni, Z.; Cote, A. P.; Choi, J. Y.; Huang, R. D.; Uribe-Romo, F. J.; Chae, H. K.; O'Keeffe, M.; Yaghi, O. M., Exceptional chemical and thermal stability of zeolitic imidazolate frameworks. *Proceedings of the National Academy of Sciences of the United States of America* **2006,** *103* (27), 10186-10191.

20.   Chui, S. S. Y.; Lo, S. M. F.; Charmant, J. P. H.; Orpen, A. G.; Williams, I. D., A chemically functionalizable nanoporous material Cu-3(TMA)(2)(H$_2$O)(3) (n). *Science* **1999,** *283* (5405), 1148-1150.

21.   Stock, N.; Biswas, S., Synthesis of Metal-Organic Frameworks (MOFs): Routes to Various MOF Topologies, Morphologies, and Composites. *Chemical Reviews* **2012,** *112* (2), 933-969.

22.   Klinowski, J.; Paz, F. A. A.; Silva, P.; Rocha, J., Microwave-Assisted Synthesis of Metal-Organic Frameworks. *Dalton Transactions* **2011,** *40* (2), 321-330.

23.   Campagnol, N.; Van Assche, T.; Boudewijns, T.; Denayer, J.; Binnemans, K.; De Vos, D.; Fransaer, J., High pressure, high temperature electrochemical synthesis of metal-organic frameworks: films of MIL-100 (Fe) and HKUST-1 in different morphologies. *Journal of Materials Chemistry A* **2013,** *1* (19), 5827-5830.

24.   Klimakow, M.; Klobes, P.; Thunemann, A. F.; Rademann, K.; Emmerling, F., Mechanochemical Synthesis of Metal-Organic Frameworks: A Fast and Facile Approach toward Quantitative Yields and High Specific Surface Areas. *Chemistry of Materials* **2010,** *22* (18), 5216-5221.

25.   Eddaoudi, M.; Kim, J.; Rosi, N.; Vodak, D.; Wachter, J.; O'Keeffe, M.; Yaghi, O. M., Systematic design of pore size and functionality in isoreticular MOFs and their application in methane storage. *Science* **2002,** *295* (5554), 469-472.

26.   Morris, W.; Stevens, C. J.; Taylor, R. E.; Dybowski, C.; Yaghi, O. M.; Garcia-Garibay, M. A., NMR and X-ray Study Revealing the Rigidity of Zeolitic Imidazolate Frameworks. *Journal of Physical Chemistry C* **2012,** *116* (24), 13307-13312.

27.   Rosi, N. L.; Kim, J.; Eddaoudi, M.; Chen, B. L.; O'Keeffe, M.; Yaghi, O. M., Rod packings and metal-organic frameworks constructed from rod-shaped secondary building units. *Journal of the American Chemical Society* **2005,** *127* (5), 1504-1518.

28.   Czaja, A. U.; Trukhan, N.; Muller, U., Industrial applications of metal-organic frameworks. *Chemical Society Reviews* **2009,** *38* (5), 1284-1293.

29.   Meek, S. T.; Greathouse, J. A.; Allendorf, M. D., Metal-Organic Frameworks: A Rapidly Growing Class of Versatile Nanoporous Materials. *Advanced Materials* **2011,** *23* (2), 249-267.

30.   Furukawa, H.; Cordova, K. E.; O'Keeffe, M.; Yaghi, O. M., The Chemistry and Applications of Metal-Organic Frameworks. *Science* **2013,** *341* (6149), 974-+.

31.   Furukawa, H.; Ko, N.; Go, Y. B.; Aratani, N.; Choi, S. B.; Choi, E.; Yazaydin, A. O.; Snurr, R. Q.; O'Keeffe, M.; Kim, J.; Yaghi, O. M., Ultrahigh Porosity in Metal-Organic Frameworks. *Science* **2010,** *329* (5990), 424-428.

32.   Schneemann, A.; Bon, V.; Schwedler, I.; Senkovska, I.; Kaskel, S.; Fischer, R. A., Flexible metal-organic frameworks. *Chemical Society Reviews* **2014,** *43* (16), 6062-6096.

33.   Xue, M.; Liu, Y.; Schaffino, R. M.; Xiang, S. C.; Zhao, X. J.; Zhu, G. S.; Qiu, S. L.; Chen, B. L., New Prototype Isoreticular Metal-Organic Framework Zn$_4$O(FMA)(3) for Gas Storage. *Inorganic Chemistry* **2009,** *48* (11), 4649-4651.

34.   DeCoste, J. B.; Peterson, G. W., Metal-Organic Frameworks for Air Purification of Toxic Chemicals. *Chemical Reviews* **2014,** *114* (11), 5695-5727.

35.   Belmabkhout, Y.; Guillerm, V.; Eddaoudi, M., Low concentration CO_2 capture using physical adsorbents: Are metal-organic frameworks becoming the new benchmark materials? *Chemical Engineering Journal* **2016,** *296*, 386-397.

36.   Li, J. R.; Ma, Y. G.; McCarthy, M. C.; Sculley, J.; Yu, J. M.; Jeong, H. K.; Balbuena, P. B.; Zhou, H. C., Carbon dioxide capture-related gas adsorption and separation in metal-organic frameworks. *Coordination Chemistry Reviews* **2011,** *255* (15-16), 1791-1823.

37.   Gonzalez, A. S.; Plaza, M. G.; Pis, J. J.; Rubiera, F.; Pevida, C., Post-combustion CO_2 capture adsorbents from spent coffee grounds. *Ghgt-11* **2013,** *37*, 134-141.

38.   Dantas, T. L. P.; Luna, F. M. T.; Silva, I. J.; de Azevedo, D. C. S.; Grande, C. A.; Rodrigues, A. E.; Moreira, R., Carbon dioxide-nitrogen separation through adsorption on activated carbon in a fixed bed. *Chemical Engineering Journal* **2011,** *169* (1-3), 11-19.

39.   Dantas, T. L. P.; Luna, F. M. T.; Silva, I. J.; Torres, A. E. B.; de Azevedo, D. C. S.; Rodrigues, A. E.; Moreira, R., Carbon dioxide-nitrogen separation through pressure swing adsorption. *Chemical Engineering Journal* **2011,** *172* (2-3), 698-704.

40.   Dantas, T. L. P.; Luna, F. M. T.; Silva, I. J.; Torres, A. E. B.; de Azevedo, D. C. S.; Rodrigues, A. E.; Moreira, R., MODELING OF THE FIXED-BED ADSORPTION OF CARBON DIOXIDE AND A CARBON DIOXIDE-NITROGEN MIXTURE ON ZEOLITE 13X. *Brazilian Journal of Chemical Engineering* **2011,** *28* (3), 533-544.

41.   Ye, S.; Jiang, X.; Ruan, L. W.; Liu, B.; Wang, Y. M.; Zhu, J. F.; Qiu, L. G., Post-combustion CO_2 capture with the HKUST-1 and MIL-101(Cr) metal-organic frameworks: Adsorption, separation and regeneration investigations. *Microporous and Mesoporous Materials* **2013,** *179*, 191-197.

42.   Mason, J. A.; Sumida, K.; Herm, Z. R.; Krishna, R.; Long, J. R., Evaluating metal-organic frameworks for post-combustion carbon dioxide capture via temperature swing adsorption. *Energy & Environmental Science* **2011,** *4* (8), 3030-3040.

43.   Millward, A. R.; Yaghi, O. M., Metal-organic frameworks with exceptionally high capacity for storage of carbon dioxide at room temperature. *Journal of the American Chemical Society* **2005,** *127* (51), 17998-17999.

44.   Camacho, B. C. R.; Ribeiro, R.; Esteves, I.; Mota, J. P. B., Adsorption equilibrium of carbon dioxide and nitrogen on the MIL-53(Al) metal organic framework. *Separation and Purification Technology* **2015,** *141*, 150-159.

45.   Xian, S. K.; Peng, J. J.; Zhang, Z. J.; Xia, Q. B.; Wang, H. H.; Li, Z., Highly enhanced and weakened adsorption properties of two MOFs by water vapor for separation of CO_2/CH_4 and CO_2/N_2 binary mixtures. *Chemical Engineering Journal* **2015,** *270*, 385-392.

46.   Kumar, A.; Madden, D. G.; Lusi, M.; Chen, K. J.; Daniels, E. A.; Curtin, T.; Perry, J. J.; Zaworotko, M. J., Direct Air Capture of CO_2 by Physisorbent Materials. *Angewandte Chemie-International Edition* **2015,** *54* (48), 14372-14377.

47.   Ben-Mansour, R.; Habib, M. A.; Bamidele, O. E.; Basha, M.; Qasem, N. A. A.; Peedikakkal, A.; Laoui, T.; Ali, M., Carbon capture by physical adsorption: Materials, experimental investigations and numerical modeling and simulations - A review. *Applied Energy* **2016,** *161*, 225-255.

48.   Waseda, Y.; Matsubara, E.; Shinoda, K., *X-Ray Diffraction Crystallography Introduction, Examples and Solved Problems*. Springer-Verlag: Berlin Heidelberg, 2011; p 310.

49.   Zhang, J. P.; Liao, P. Q.; Zhou, H. L.; Lin, R. B.; Chen, X. M., Single-crystal X-ray diffraction studies on structural transformations of porous coordination polymers. *Chemical Society Reviews* **2014,** *43* (16), 5789-5814.

50.   Takamizawa, S.; Nakata, E.; Saito, T.; Kojima, K., Structural determination of physisorbed sites for CO2 and Ar gases inside an organometallic framework. *Crystengcomm* **2003,** *5*, 411-413.

51.   Takamizawa, S.; Nakata, E.; Saito, T., Gas inclusion crystal between 1-D coordination polymer and nitrous oxide: occurrence of crystal phase transition induced by a slight amount of fluid guests inside host. *Inorganic Chemistry Communications* **2003,** *6* (12), 1415-1418.

52.   Takamizawa, S.; Takasaki, Y.; Miyake, R., Host-guest transformational correlations for a gas inclusion co-crystal on changing gas pressure and temperature. *Chemical Communications* **2009,** (43), 6625-6627.

53.   Wriedt, M.; Sculley, J. P.; Yakovenko, A. A.; Ma, Y. G.; Halder, G. J.; Balbuena, P. B.; Zhou, H. C., Low-Energy Selective Capture of Carbon Dioxide by a Pre-designed Elastic Single-Molecule Trap. *Angewandte Chemie-International Edition* **2012,** *51* (39), 9804-9808.

54.   Zhao, P.; Lampronti, G. I.; Lloyd, G. O.; Wharmby, M. T.; Facq, S.; Cheetham, A. K.; Redfern, S. A. T., Phase Transitions in Zeolitic Imidazolate Framework 7: The Importance of Framework Flexibility and Guest-Induced Instability. *Chemistry of Materials* **2014,** *26* (5), 1767-1769.

55.   Sotelo, J.; Woodall, C. H.; Allan, D. R.; Gregoryanz, E.; Howie, R. T.; Kamenev, K. V.; Probert, M. R.; Wright, P. A.; Moggach, S. A., Locating Gases in Porous Materials: Cryogenic Loading of Fuel-Related Gases Into a Sc-based Metal-Organic Framework under Extreme Pressures. *Angewandte Chemie-International Edition* **2015,** *54* (45), 13332-13336.

56.   Chen, S. S.; Lucier, B. E. G.; Boyle, P. D.; Huang, Y. N., Understanding The Fascinating Origins of CO_2 Adsorption and Dynamics in MOFs. *Chemistry of Materials* **2016,** *28* (16), 5829-5846.

57.   Akitt, J. W.; Mann, B. E., *NMR and Chemistry*. 4th ed.; Stanley Thornes Ltd: Cheltenham, United Kingdom, 2000; p 400.

58.   MacKenzie, K.; Smith, M. E., *Multinuclear Solid-State Nuclear Magnetic Resonance of Inorganic Materials*. Pergamon: Oxford New York, 2002.

59.   Duer, M. J., *Solid-State NMR Spectroscopy*. Blackwell Publishing Ltd: Oxford, United Kingdom, 2004; p 349.

60.   Eichele, R. E. W. K. *WSolids1*, University of Tübingen: Germany, 2001.

61.   Bryce, D. L.; Bernard, G. M.; Gee, M.; Lumsden, M. D.; Eichele, K.; Wasylishen, R. E., Practical aspects of modern routine solid-state multinuclear magnetic resonance spectroscopy: One-dimensional experiments. *Canadian Journal of Analytical Sciences and Spectroscopy* **2001,** *46* (2), 46-82.

62.   Zhang, Y.; Lucier, B. E. G.; Huang, Y. N., Deducing CO_2 motion, adsorption locations and binding strengths in a flexible metal-organic framework without open metal sites. *Physical Chemistry Chemical Physics* **2016,** *18* (12), 8327-8341.

63.   Gullion, T., Introduction to rotational-echo, double-resonance NMR. *Concepts in Magnetic Resonance* **1998,** *10* (5), 277-289.

64.   Lee, M.; Goldburg, W. I., NUCLEAR-MAGNETIC-RESONANCE LINE NARROWING BY A ROTATING RF FIELD. *Physical Review* **1965,** *140* (4A), 1261-&.

65.   Bielecki, A.; Kolbert, A. C.; Levitt, M. H., FREQUENCY-SWITCHED PULSE SEQUENCES - HOMONUCLEAR DECOUPLING AND DILUTE SPIN NMR IN SOLIDS. *Chemical Physics Letters* **1989,** *155* (4-5), 341-346.

66.   van Rossum, B. J.; de Groot, C. P.; Ladizhansky, V.; Vega, S.; de Groot, H. J. M., A method for measuring heteronuclear (H-1-C-13) distances in high speed MAS NMR. *Journal of the American Chemical Society* **2000,** *122* (14), 3465-3472.

67.   Bennett, A. E.; Rienstra, C. M.; Auger, M.; Lakshmi, K. V.; Griffin, R. G., HETERONUCLEAR DECOUPLING IN ROTATING SOLIDS. *Journal of Chemical Physics* **1995,** *103* (16), 6951-6958.

68.   Patching, S. G., NMR-Active Nuclei for Biological and Biomedical Applications. *Journal of Diagnostic Imaging in Therapy* **2016**, *3* (1), 7-48.

69.   Mali, G., *Metal-Organic Frameworks*. InTech: 2016.

70.   Beeler, A. J.; Orendt, A. M.; Grant, D. M.; Cutts, P. W.; Michl, J.; Zilm, K. W.; Downing, J. W.; Facelli, J. C.; Schindler, M. S.; Kutzelnigg, W., LOW-TEMPERATURE C-13 MAGNETIC-RESONANCE IN

SOLIDS .3. LINEAR AND PSEUDOLINEAR MOLECULES. *Journal of the American Chemical Society* **1984,** *106* (25), 7672-7676.

71.   Lu, Y. J.; Lucier, B. E. G.; Zhang, Y.; Ren, P. J.; Zheng, A. M.; Huang, Y. N., Sizable dynamics in small pores: CO_2 location and motion in the alpha-Mg formate metal-organic framework. *Physical Chemistry Chemical Physics* **2017,** *19* (8), 6130-6141.

72.   Wang, W. D.; Lucier, B. E. G.; Terskikh, V. V.; Wang, W.; Huang, Y. N., Wobbling and Hopping: Studying Dynamics of CO2 Adsorbed in Metal-Organic Frameworks via O-17 Solid-State NMR. *Journal of Physical Chemistry Letters* **2014,** *5* (19), 3360-3365.

73.   Loiseau, T.; Serre, C.; Huguenard, C.; Fink, G.; Taulelle, F.; Henry, M.; Bataille, T.; Ferey, G., A rationale for the large breathing of the porous aluminum terephthalate (MIL-53) upon hydration. *Chemistry-a European Journal* **2004,** *10* (6), 1373-1382.

74.   Sutrisno, A.; Terskikh, V. V.; Shi, Q.; Song, Z. W.; Dong, J. X.; Ding, S. Y.; Wang, W.; Provost, B. R.; Daff, T. D.; Woo, T. K.; Huang, Y. N., Characterization of Zn-Containing Metal-Organic Frameworks by Solid-State ^{67}Zn NMR Spectroscopy and Computational Modeling. *Chemistry-a European Journal* **2012,** *18* (39), 12251-12259.

75.   Xu, J.; Lucier, B. E. G.; Sinelnikov, R.; Terskikh, V. V.; Staroverov, V. N.; Huang, Y. N., Monitoring and Understanding the Paraelectric-Ferroelectric Phase Transition in the Metal-Organic Framework NH_4 M(HCOO)(3) by Solid-State NMR Spectroscopy. *Chemistry-a European Journal* **2015,** *21* (41), 14348-14361.

76.   He, P.; Lucier, B. E. G.; Terskikh, V. V.; Shi, Q.; Dong, J. X.; Chu, Y. Y.; Zheng, A. M.; Sutrisno, A.; Huang, Y. N., Spies Within Metal-Organic Frameworks: Investigating Metal Centers Using Solid-State NMR. *Journal of Physical Chemistry C* **2014,** *118* (41), 23728-23744.

77.   Volkringer, C.; Popov, D.; Loiseau, T.; Ferey, G.; Burghammer, M.; Riekel, C.; Haouas, M.; Taulclle, F., Synthesis, Single-Crystal X-ray Microdiffraction, and NMR Characterizations of the Giant Pore Metal-Organic Framework Aluminum Trimesate MIL-100. *Chemistry of Materials* **2009,** *21* (24), 5695-5697.

78.   Xu, J.; Terskikh, V. V.; Huang, Y. N., Mg-25 Solid-State NMR: A Sensitive Probe of Adsorbing Guest Molecules on a Metal Center in Metal-Organic Framework CPO-27-Mg. *Journal of Physical Chemistry Letters* **2013,** *4* (1), 7-11.

79.   Xu, J.; Terskikh, V. V.; Huang, Y. N., Resolving Multiple Non-equivalent Metal Sites in Magnesium-Containing MetalOrganic Frameworks by Natural Abundance ^{25}Mg Solid-State NMR Spectroscopy. *Chemistry-a European Journal* **2013,** *19* (14), 4432-4436.

80.   Celic, T. B.; Mazaj, M.; Guillou, N.; Elkaim, E.; El Roz, M.; Thibault-Starzyk, F.; Mali, G.; Rangus, M.; Cendak, T.; Kaucic, V.; Logar, N. Z., Study of Hydrothermal Stability and Water Sorption Characteristics of 3-Dimensional Zn-Based Trimesate. *Journal of Physical Chemistry C* **2013,** *117* (28), 14608-14617.

81.   Xu, J.; Sinelnikov, R.; Huang, Y. N., Capturing Guest Dynamics in Metal-Organic Framework CPO-27-M (M = Mg, Zn) by H-2 Solid-State NMR Spectroscopy. *Langmuir* **2016,** *32* (22), 5468-5479.

82.   Nugent, P.; Belmabkhout, Y.; Burd, S. D.; Cairns, A. J.; Luebke, R.; Forrest, K.; Pham, T.; Ma, S.; Space, B.; Wojtas, L.; Eddaoudi, M.; Zaworotko, M. J., Porous materials with optimal adsorption thermodynamics and kinetics for CO_2 separation. *Nature* **2013,** *495* (7439), 80-84.

83.   Vaidhyanathan, R.; Iremonger, S. S.; Dawson, K. W.; Shimizu, G. K. H., An amine-functionalized metal organic framework for preferential CO_2 adsorption at low pressures. *Chemical Communications* **2009,** (35), 5230-5232.

Chapter 2 : Studying Carbon Dioxide Adsorption within the Highly Selective SIFSIX-3-Zn Framework

2.1   Introduction

One recently reported novel class of materials is the SIFSIX frameworks.[1] These materials can be described as hybrid ultramicroporous materials (or HUMs) rather than MOFs. SIFSIX materials are HUMs because in addition to organic linkers that join the metal centres into a two-dimensional sheet, the sheets are further linked into a three-dimensional framework by inorganic SiF_6^{2-} pillars, giving the framework their name. This combination of inorganic and organic linkers alongside metal centres distinguishes this material from traditional MOFs. HUM materials that have been investigated for CO_2 adsorption include SIFSIX materials,[2, 3] TIFSIX and SNIFSIX materials,[4, 5] MOOFOUR and CROFOUR materials[6], NbOFFIVE materials[7] and AlFFIVE materials,[8] with the SIFSIX materials among the most popular and widely studied.

Unlike many MOFs investigated for applications in gas adsorption and separation, the SIFSIX frameworks do not possess any open metal sites (OMSs). OMS MOFs such as HKUST-1[9] and Mg-MOF-74[10] are often considered among the most promising CO_2 capture materials due to the strong interactions between OMSs and CO_2 molecules. However, such sites are also hydrophilic, therefore water often acts as a competitor to CO_2.[11, 12] In a worst-case scenario, water can permanently degrade a MOF through a hydrolysis or ligand displacement reaction. The presence of coordinatively-saturated metal centres within the frameworks, rather than unsaturated OMSs, is potentially advantageous for water stability and CO_2 selectivity of the MOF, as the adsorption mechanism is no longer a metal-sorbate interaction.
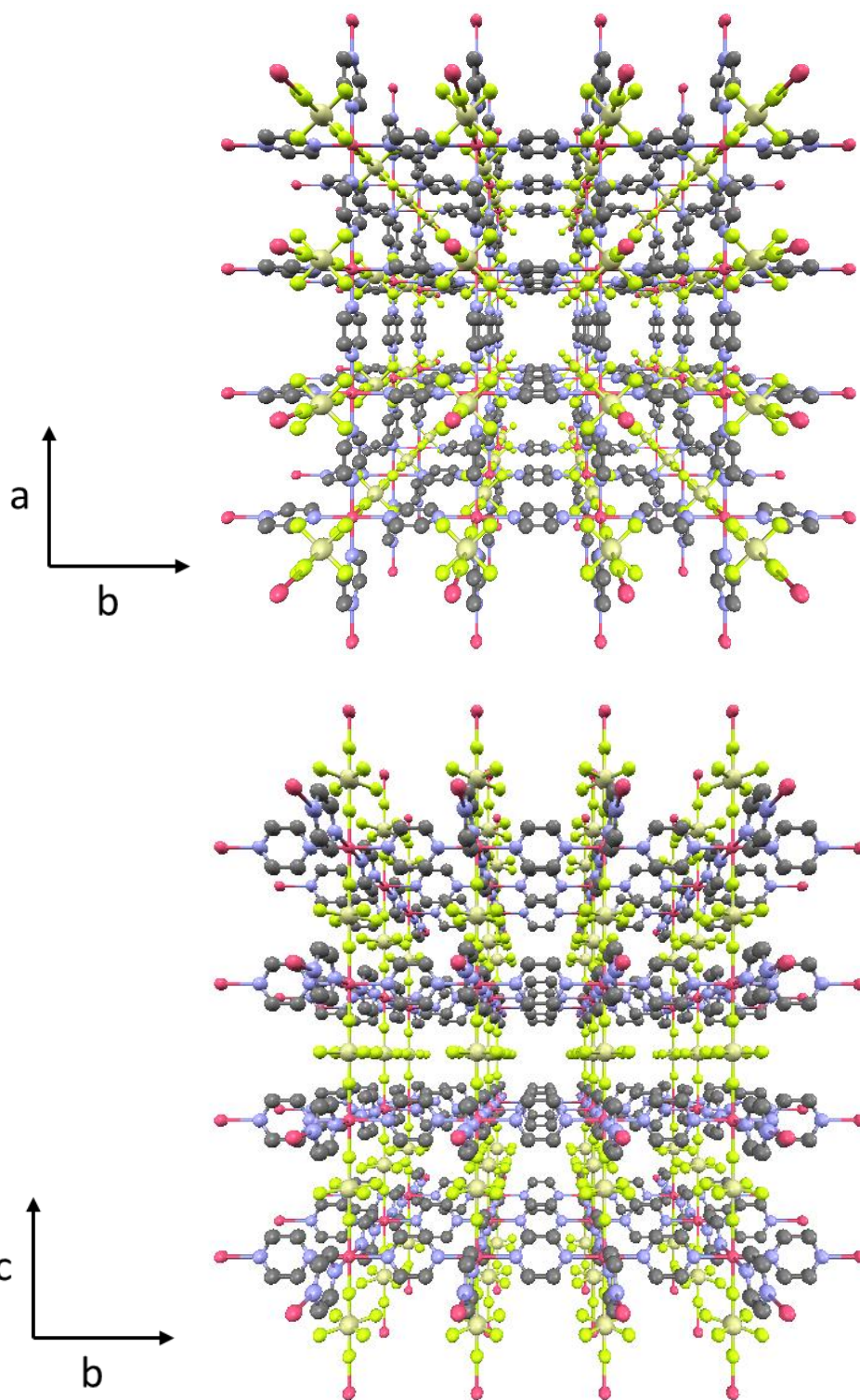
Figure 2.1: The SIFSIX-3-Zn framework is illustrated from a perspective that lies along the c-axis (above) and a-axis (below). In this Figure, the atom colours are pink for Zn, tan for Si, yellow for F, blue for N, and grey for C.

SIFSIX-3 materials, which contain organic pyrazine ligands along with SiF_6^{2-} inorganic pillars, have shown particular promise in the field of CO_2 adsorption.[12-14] The first SIFSIX-3 material studied for CO_2 adsorption applications was SIFSIX-3-Zn.[2, 3] In SIFSIX-3-Zn, one-dimensional square channels 3.84 Å diagonally across point run along the length of the framework's *c*-axis. Four fluorine atoms extend from the corners into these channels at regular intervals. Small windows which measure 2 Å diagonally connect the channels along the *a* and *b*-axes. Computational and Raman spectroscopy studies of SIFSIX-3-Zn have offered insight into the CO_2 adsorption behaviour of the material.[13-16] The fluorine atoms are thought to interact with the electropositive carbon atom on the CO_2 molecule, oriented along the direction of the channels, allowing for a single guest molecule per unit cell. The maximum CO_2 uptake remains unchanged at pressures as high as 25.0 atm, and this uptake has been observed at temperatures as high as 338 K.[14]

One unusual aspect of SIFSIX-3-Zn adsorption behaviour is the adsorption of greater amounts of CO_2 at room temperature than at 195 K.[13] This phenomenon is thought to be partially due to the conformational flexibility of the pyrazine rings within the framework, which at low temperatures can tilt from the perpendicular direction to the parallel direction of the channel in order to reduce pore volume and surface area.[13] Diffusion of guest CO_2 within the channels is thought to be limited at lower temperatures due to increased interaction strengths between the guest molecules and the framework. This leads to pore blockage, which hinders the ability of free CO_2 molecules to access potential adsorption sites within the framework.[14]

The framework structure of SIFSIX-3-Zn as viewed along the crystallographic *c*-axis is shown in Figure 2.1.[2] The structure is a tetragonal crystal system with a space group of P4/mmm. The similar dimensions of the pore diameter, 3.84 Å, and CO_2 kinetic diameter, 3.30 Å,[17] facilitates

strong electrostatic interactions between the framework and guest molecules, as well as high selectivity towards CO_2 over CH_4, H_2 and N_2, despite the framework's relatively small surface areas and pore sizes. Ideal adsorbed solution theory (IAST) calculations were used comparing the ratio of adsorbed gases divided by the ratio of the gases before adsorption.[2] This quantifies the SIFSIX-3-Zn selectivity for CO_2 at 1 bar as 1818 against N_2, 231 against CH_4, and over 1800 against H_2.[2] The selectivity against N_2 is extremely high, easily exceeding the selectivity of popular frameworks such as Mg-MOF-74,[10] which has a selectivity of 800 against N_2, and Zeolite 13X,[18] which has a selectivity of 420 against N_2.

Table 2.1: The CO_2 adsorption properties of various solid sorbent materials are listed below. These were determined using temperature-programmed desorption experiments after either direct air capture experiments or moist simulated-flue gas capture experiments. The S_{CW} value indicates the experimental sorbent selectivity for CO_2 over H_2O.

Adsorbent	Direct Air Capture			Moist CO_2 (0.15 atm, 75% RH)		
	CO_2 (mg g^{-1})	H_2O (mg g^{-1})	S_{CW}	CO_2 (mg g^{-1})	H_2O (mg g^{-1})	S_{CW}
SIFSIX-3-Ni[19]	8.0	93	5.43	76	46	0.27
SIFSIX-3-Cu[20]	14.1	88	10.03	101	54	0.31
Zeolite 13X[19]	1.5	146	0.63	26.3	93	0.05
Mg-MOF-74[19]	6.3	171	2.60	68	65	0.17
ZIF-8[20]	2.3	7.6	18.67	2.5	>1	0.50
MIL-101[20]	<1.0	95	<0.63	11.2	16.8	0.11
TEPA-SBA-15[19]	158	12	830	130.3	11	1.92

This high selectivity for CO_2 is also observed in other SIFSIX-3 materials with alternate metal centres, including SIFSIX-3-Cu,[21] SIFSIX-3-Ni,[22, 23] and SIFSIX-3-Co.[23] A series of studies aimed at assessing CO_2 adsorption properties found that SIFSIX-3-Ni and SIFSIX-3-Cu had especially strong selectivity for CO_2 adsorption over H_2O adsorption compared to other physisorbents, as depicted in Table 2.1.[19, 20] The potential applications of SIFSIX-3 materials in gas adsorption were made clear from these results. While ZIF-8[24] was found to possess greater selectivity for CO_2 than SIFSIX-3-Ni, it had an extremely low overall CO_2 uptake.[20] ZIF frameworks are known to be hydrophobic if their imidazolate linkers do not possess hydrophilic functional groups.[25] The chemisorbent functionalized silica framework TEPA-SBA-15[26] possessed greater uptake and selectivity than SIFSIX-3-Ni,[19] however, as a chemisorbent, it is vulnerable to sorbent degradation from NO_x, SO_x, and O_2. Chemisorbents also typically require more energy for reactivation than physisorbents, with temperature programmed desorption experiments showing TEPA-SBA-15 required higher temperatures to desorb both CO_2 and H_2O than SIFSIX-3-Ni.[19] SIFSIX-3-Ni has also shown little change in surface area or CO_2 uptake after accelerated stability testing.[19]

The results of these experiments are especially important for practical applications, as the presence of moisture in air is typically unavoidable, and mentioned above many MOFs degrade in the presence of moisture or liquid water due to nucleophilic water molecules attacking the metal-ligand bonds within the framework.[11, 12] Unfortunately, these results show SIFSIX materials still rate behind traditional chemisorbents in CO_2 selectivity, thus continued investigation into their adsorption properties and continued development of new and improved MOFs and HUMs incorporating SIFSIX components is necessary to develop a practical solid physisorbent material for CO_2 adsorption applications.

While the unusual CO_2 adsorption behaviour of SIFSIX-3 materials are known, a comprehensive description of the CO_2 interactions and motions within the frameworks does not yet exist. To improve the scientific community's understanding of MOFs and their carbon dioxide capture applications, this chapter helps fill this gap by offering information on how the framework and guest CO_2 molecule interact with and affect one another. This is done through two techniques: single crystal X-ray diffraction (SCXRD) and solid-state nuclear magnetic resonance spectroscopy (SSNMR).

SCXRD experiments can identify the precise number, locations, and occupancies of adsorption sites within the framework. SCXRD is widely used for determining the crystal structure of MOFs, and obtaining the locations of guest molecules within the framework.[27-30] This can be supplemented by SSNMR experiments, which provide information on guest molecule mobility.

Table 2.2: Select physical properties and CO_2 adsorption properties of SIFSIX-3-M materials are listed below. The Q_{st} value indicates the isoteric enthalpy of adsorption for CO_2 capture.

Adsorbent	BET Surface Area (m^2 g^{-1})	Pore Size (Å)	Q_{st} (kJ mol^{-1})	Static CO_2 uptake at 0.15 bar (mol kg^{-1})
SIFSIX-3-Ni[23]	368	3.7	51	2.65
SIFSIX-3-Co[23]	223	-	47	2.5
SIFSIX-3-Cu[21]	300	3.5	54	2.45
SIFSIX-3-Zn[2]	250	3.84	45	2.2

Solid-state NMR is a powerful tool for obtaining molecular-level insight regarding the origins and mechanisms of guest adsorption,[27, 31-34] and for the SIFSIX family, the SIFSIX-3-Zn analogue was selected for study.

SIFSIX-3-Zn shares many of the characteristic properties of SIFSIX-3 materials in terms of structure and CO_2 adsorption behaviour, as shown in Table 2.2.[2, 21-23] Unfortunately, SIFSIX-3-Zn is sensitive to the presence of moisture, unlike other SIFSIX-3 materials.[35] However, the diamagnetic Zn^{2+} metal centre was more useful for this study, as paramagnetic ions such as Ni^{2+}, Co^{2+}, or Cu^{2+} possess unpaired electrons giving rise to strong local magnetic fields. These can complicate the spectral analyses.[36] It is hoped that insight into the CO_2 adsorption behaviour of SIFSIX-3-Zn will be useful for understanding the CO_2 adsorption behaviour of other SIFSIX-3 materials.

2.2   Experimental

2.2.1   Synthesis of SIFSIX-3-Zn

SIFSIX-3-Zn was synthesized solvothermally using previously described methods.[2]   A typical synthesis is as follows: a 10 mL solution of pyrazine (0.48 g, 6 mmol, Alfa Aesar, 98%) in methanol was decanted into a separate 10 mL solution of zinc hexafluorosilicate hydrate (0.62 g, 3 mmol, Sigma-Aldrich, 99%) in methanol. The resulting 20 mL solution was left at room temperature for 3 days, after which yellow crystals were collected and dried at 90 °C in air for three hours. Prior to activation and guest loading, SIFSIX-3-Zn samples were solvent exchanged in a methanol solution for three days, as done in the literature.[2] The methanol solution was replaced daily.

2.2.2 Powder X-ray diffraction

The identities and purities of the product were confirmed using powder X-ray diffraction (PXRD). Patterns were recorded on an Inel CPS powder diffractometer operating with Cu Kα radiation (λ = 1.5418 Å). Experimental and simulated PXRD patterns are depicted in Figure 2.2. The experimental PXRD patterns are consistent with patterns calculated from reported crystal structures,[2] and are also consistent with previously determined experimental PXRD patterns of the materials.[2] This suggests phase purity of the synthesized framework.
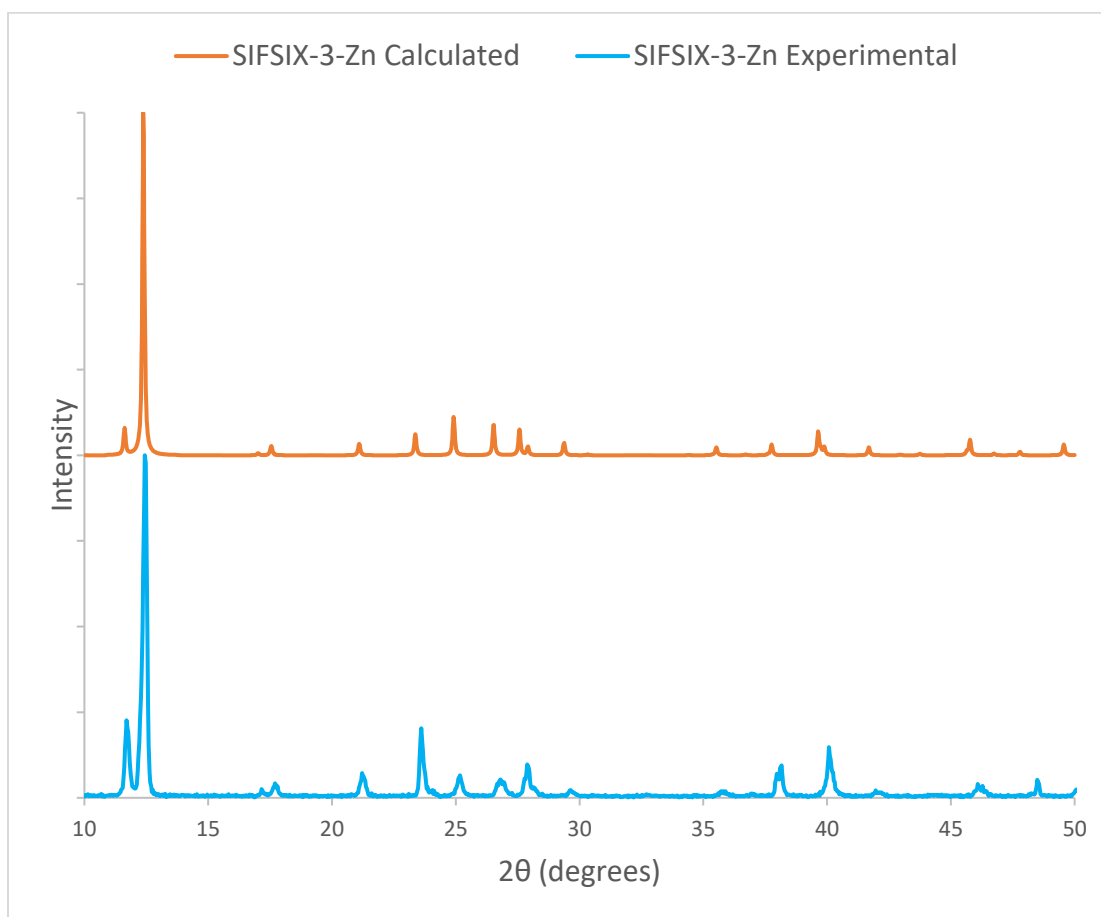
Figure 2.2: The experimental and calculated SIFSIX-3-Zn PXRD patterns are depicted above.

2.2.3 Sample activation and gas loading

The activation process removes solvent molecules from the framework pores. A Schlenk line was used for the activation of SIFSIX-3-Zn. Samples were placed into the bottom of an L-shaped glass tube, and a thin layer of glass wool was used to secure the sample in place. SIFSIX-3-Zn samples were activated under dynamic vacuum (< 1 mbar) at 80 ± 10 °C for twenty-four hours. CO_2 gas was released into the line, which has a measured total volume of 82.7 mL, as the CO_2 pressure was monitored simultaneously. The sample was then loaded with a known quantity of CO_2 while the glass tube was immersed in liquid nitrogen. The loaded sample within the glass tube was then flame sealed off from the Schlenk line to trap guest molecules in a closed space with the sample prior to SSNMR experiments.

A 0.25 molar ratio of CO_2 to Zn^{2+} was used when loading samples with carbon dioxide for SSNMR experiments. ^{13}C labelled CO_2 was used to load samples for ^{13}C SSNMR experiments.

2.2.4 SCXRD experiments

A small amount of SIFSIX-3-Zn single crystals were packed into a glass tube, activated, and loaded with CO_2 using the procedures outlined above. Samples were loaded to saturation with CO_2. Prior to SCXRD experiments, the glass tubes containing CO_2-saturated SIFSIX-3-Zn were broken, and the single crystals were immediately coated with paratone oil to prevent loss of CO_2 from the framework. Using an optical microscope, high-quality single crystals were selected for use in structure determination and refinement.

All X-ray measurements were made on a Bruker-Nonius KappaCCD Apex2 diffractometer at a temperature of 110 K. The frame integration was performed using SAINT.[37] The resulting raw data was scaled and absorption corrected using a multi-scan averaging of symmetry equivalent data using SADABS.[38] The structure was solved by using a dual space methodology using the

SHELXT program.[39] All framework non-hydrogen atoms were obtained from the initial solution. The hydrogen atoms were introduced at idealized positions and were allowed to ride on the parent atom. The position of the CO_2 molecule was recovered from a difference Fourier map. The structural model was fit to the data using full matrix least-squares based on F^2. The calculated structure factors included corrections for anomalous dispersion from the usual tabulation. The structure was refined using the SHELXL-2014 program from the SHELX suite of crystallographic software.[40] Graphic plots were produced using the NRCVAX program suite.[41]

2.2.5 SSNMR experiments

^{13}C, ^{29}Si, ^{1}H and ^{19}F SSNMR experiments were performed at the University of Western Ontario in London, Ontario, using a Varian Infinity Plus wide-bore NMR spectrometer, equipped with an Oxford 9.4 T wide-bore magnet. Direct-excitation static ^{13}C experiments were conducted with a 5 mm HFXY Varian/Chemagnetics probe. All ^{13}C, ^{1}H and ^{19}F magic-angle spinning (MAS) experiments were performed with a 4 mm HXY Varian/Chemagnetics probe, while ^{29}Si MAS and static cross polarization (CP) experiments were carried out with a 7.5 mm HXY Varian/Chemagnetics probe.

^{13}C spectra were referenced to tetramethylsilane (TMS) using the methylene carbon in ethanol as a secondary reference, which has a chemical shift (CS) of 58.05 ppm.[42] All direct-excitation ^{13}C SSNMR experiments were performed using the DEPTH-echo pulse sequence to minimize the probe background signal.[31] The Hartmann-Hahn match in ^{1}H-^{13}C CP experiments was set up using solid adamantane (Sigma-Aldrich, 98+%), while the Hartmann-Hahn match in ^{19}F-^{13}C CP experiments was set up using solid polytetrafluoroethylene (Sigma-Aldrich). ^{29}Si spectra were referenced to TMS using the methylsilane silicon in tris(trimethylsilyl)silane (TTMSS, Sigma-Aldrich, ≥97%) as a secondary reference, which has a CS of -9.60 ppm.[42] The

Hartmann-Hahn match in ^{1}H-^{29}Si CP experiments was set up using TTMSS. ^{19}F spectra were referenced to trichloro-fluoro-methane using liquid trifluorotoluene (Sigma-Aldrich, 99+%) as a secondary reference, which has a CS of -63.0 ppm,[43] while ^{1}H spectra were referenced to TMS using the CH$_2$ sites in solid adamantane (Sigma-Aldrich, 98+%) as a secondary reference with a CS of 1.85 ppm.[44] Direct-excitation ^{1}H and ^{19}F experiments were performed using a one pulse sequence. All experiments were performed using a 30 kHz ^{1}H decoupling field, and doubly decoupled spectra were collected using an additional 30 kHz ^{19}F decoupling field (Figure S2.2).

^{67}Zn experiments were conducted at 21.1 T on a Bruker II Advance spectrometer at the National Ultrahigh-field NMR facility for Solids in Ottawa, Canada, with a home built 7 mm HX probe, using a solid-echo pulse sequence. Spectra were referenced to 1.0 M aqueous Zn(NO$_3$)$_2$, at 0 ppm.

Additional acquisition parameters for specific spectra are listed in Tables S2.1 to S2.4.

2.2.6 Spectral simulations

The WSolids[45] computer software was used to analytically simulate all static ^{13}C SSNMR spectra and obtain apparent powder pattern parameters. The ^{13}C patterns are broadened and dominated by the CS anisotropy (CSA), while the ^{67}Zn patterns are dominated by the quadrupolar interaction (QI). WSolids calculated the powder pattern of a static powder sample showing effects of the CSA or QI. ^{13}C SSNMR patterns were calculated through inputting the orthogonal components of the CS tensor (δ_{11}, δ_{22} and δ_{33}). ^{67}Zn SSNMR patterns were calculated through inputting the electric field gradient (EFG) parameters (C$_Q$ and η$_Q$). By comparing the known experimental powder patterns to a calculated pattern, the experimental powder pattern parameters for ^{13}C (δ_{iso}, Ω and κ) and ^{67}Zn (C$_Q$ and η$_Q$) can be determined. The errors in pattern parameters were estimated by bidirectional variation of the parameters from the best-fit value.

The EXPRESS[46] computer software was used to simulate the effects of motion on ^{13}C SSNMR powder patterns. EXPRESS describes motion in terms of discrete (Markovian) jumps at specified rates between sites. A motional model can then be described by the number, orientation, and populations of sites, as well as the nature of the connections and rates of jumps. The motion results in a predictable averaging of CS tensor components. Given the known powder pattern parameters of solid CO_2 (δ_{iso} = 126 ppm, Ω = 335 ppm, and κ = 1),[47] and assuming a linear geometry for the CO_2 molecule, powder patterns produced by specific types and rates of motion were calculated across 4096 powder increments using the ZCW powder averaging procedure and compared to the experimental powder pattern.

2.2.7   Theoretical calculations

Gauge-including projector augmented wave (GIPAW) quantum chemical calculations were performed by Dr. Victor Terskikh with the NMR module of the CASTEP software package version 4.4 within Materials Studio.[48, 49] The unit cell parameters and atomic coordinates for SIFSIX-3-Zn were taken from the reported room temperature crystal structure,[2] with and without geometry optimization prior to NMR calculations. Calculations were performed with a plane-wave cut-off energy of 500 eV and on-the-fly generated ultrasoft pseudopotentials.

2.3   Results and Discussion

2.3.1   SCXRD of CO_2 loaded SIFSIX-3-Zn at 110 K

SCXRD of the CO_2 loaded framework provides a precise view of average CO_2 locations within the framework and the exact dimensions of the structure after CO_2 loading. This offers a bigger picture of the structure before SSNMR probes specific motional behaviour and host-guest interactions.
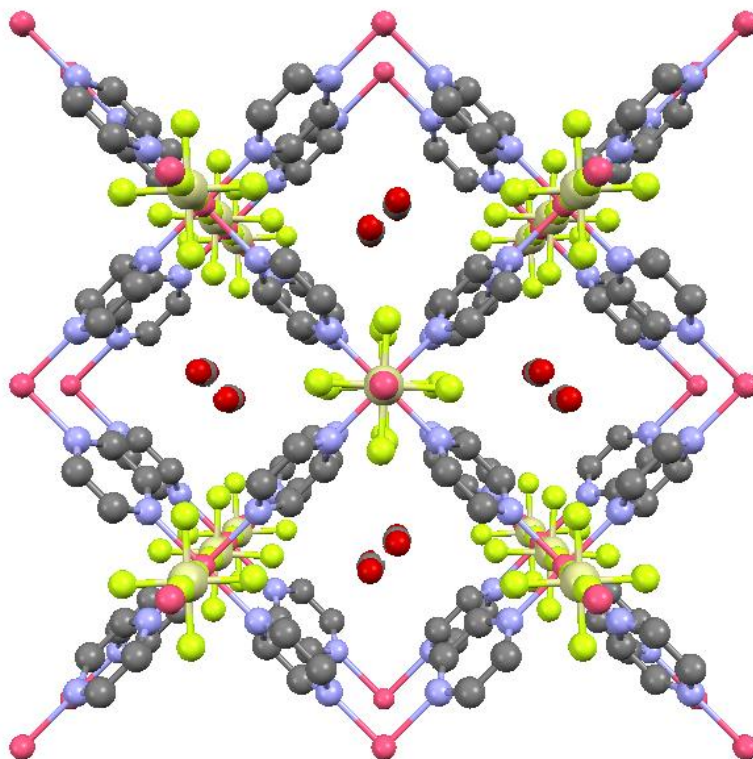
Figure 2.3: The crystal structure of CO_2 loaded SIFSIX-3-Zn is shown above, as viewed along the c-axis. The structure is depicted with pores occupied by CO_2. CO_2 molecules are located about the crystallographic inversion centre, and positionally disordered across the centre. In Figures 2.3, 2.4, 2.5, 2.6, 2.7 and 2.8, the atom colours are pink for Zn, tan for Si, yellow for F, blue for N, and grey for C.

A view of the structure along the *c*-axis can be seen in Figure 2.3. The exact location of adsorbed CO_2 and the structural parameters of SIFSIX-3-Zn were determined using SCXRD. The CO_2 was located near a crystallographic inversion centre within the centre framework channels, found directly between four equatorial fluorine atoms of the hexafluorosilicate ligands extending into the channel. The CO_2 molecule positionally disordered across that centre. The occupancy parameter converged to a value of 0.466(7), and the CO_2 geometry is linear ($\angle$O–C–O = 178.19°, with the oxygen atoms tilted slightly towards the framework). Rather than adsorbing directly in

the centre of the channel, the CO_2 molecule possesses two symmetry equivalent adsorption sites within each pore, located closer to the framework atoms. The relative locations of these sites are shown in Figure 2.3.

A previous study using single component adsorption simulations of CO_2 in SIFSIX-3-Zn estimated there was a distance of 4.4 Å between the CO_2 molecule and the nearest silicon atom.[14] This is consistent with the distance of 4.624 Å between the guest and the Si atom, obtained from the single crystal structure. The location of the CO_2 within the centre of the framework channels agrees with the previously modelled occupancy, suggesting one carbon dioxide molecule per unit cell within the framework.[2, 14] The structure finds the CO_2 molecules are aligned parallel with the framework channels, which is consistent with previously performed simulations.[2, 14]

Fluorine and hydrogen atoms extend into the channel near the CO_2, and are thought to interact with the CO_2. The nearest two fluorine atoms are 2.958 Å from the adsorbed carbon. The nearest two hydrogen atoms are 3.438 Å from the adsorbed carbon and 2.935 Å from the nearest adsorbed oxygen. These short distances are suggestive of physical interactions between the carbon nucleus and the framework protons and fluorine atoms extending into the channel. These distances are depicted in Figure 2.4 and Figure 2.5. Changes in the framework structure after CO_2 loading, due to these interactions, move these atoms in closer proximity to the guest CO_2 molecule, as explained in more detail below.

The crystallographic structure of empty SIFSIX-3-Zn has been previously studied at both room temperature and 100 K.[2, 14] The presence of CO_2 within the framework changes the space group of the crystal structure, from P4/mmm to I4/mcm. This is due to a redefining of the bounds of the unit cell, altering the unit cell parameters, depicted in Figure 2.6. The *a* parameter increases to 9.9917(14) Å (from 7.116(1) Å at 100 K) while *c* increases to 15.088(2) Å (from 7.58(1) Å).

The structure is contracted slightly from the previously reported 100 K structure, with the distance between Zn^{2+} ions being 7.065 Å along the *a*-axis and *b*-axis, alongside a 7.544 Å contraction along the *c*-axis. This indicates a slight contraction of 0.051 Å along the *a*-axis and *b*-axis, and a contraction of 0.036 Å along the *c*-axis, compared to the previously reported structure at 100 K.[14] Along the *c*-axis, this is due to a shrinking of the Zn – F – Si bonds by about 0.015 Å. Along the *a*-axis, this is due to a shrinking of the Zn – N bond by approximately 0.018 Å, and a shrinking of the pyrazine ring diameter by approximately 0.015 Å. The bond angles about the Zn and Si nuclei are unchanged, with both sites being octahedral.
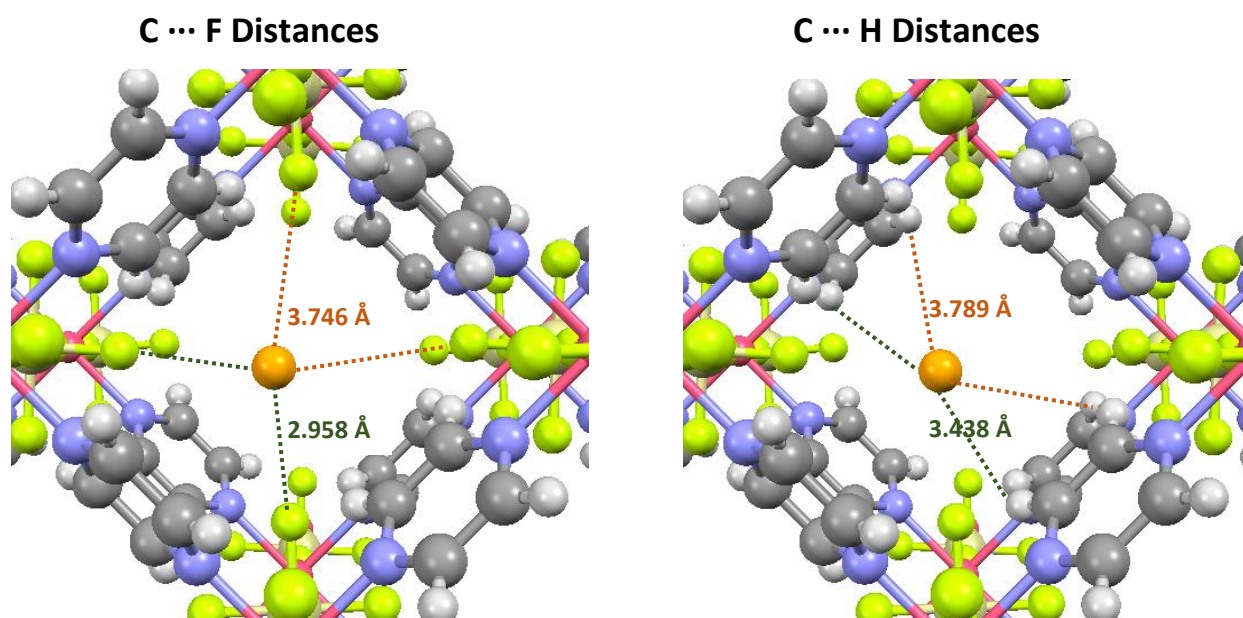
Figure 2.4: The position of the adsorbed carbon atom (orange) within the SIFSIX-3-Zn pore is shown above, as viewed along the c-axis. The carbon atom in the adsorbed CO_2 is more proximate to two of the adjacent fluorine atoms than the others, with C to F distances of 2.958 Å and 3.746 Å respectively, as seen in the leftmost image. Similarly, the adsorbed carbon atom is more proximate to two of the adjacent hydrogen atoms than to the other two, with C to H distances of 3.438 Å and 3.789 Å respectively, as depicted in the rightmost image.

O ··· H Distances
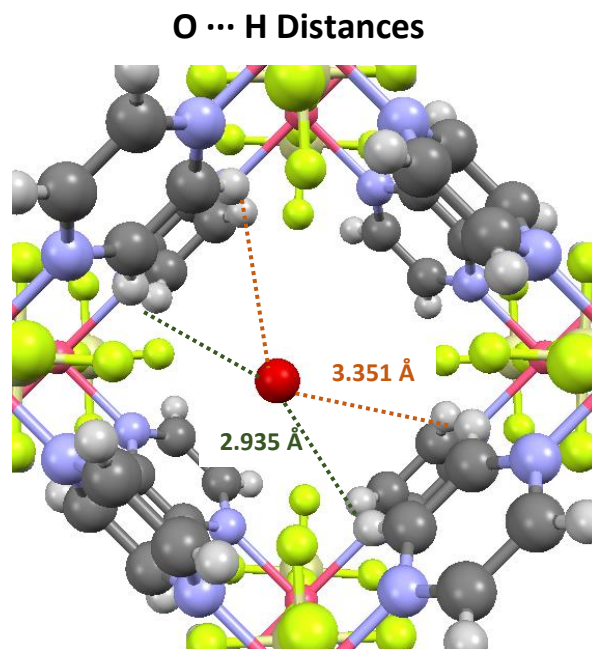
Figure 2.5: The position of an adsorbed oxygen atom (red) within the SIFSIX-3-Zn pore is shown above, as viewed along the c-axis. The oxygen atoms in the adsorbed CO_2 is more proximate to two of the adjacent hydrogen atoms than the others, with O to H distances of 2.935 Å and 3.351 Å respectively.

The overall contraction of the CO_2 loaded framework is evidence of strong interactions between the CO_2 and the crystal structure, as the shrinking will promote stronger interactions with the CO_2 residing within the framework pores.

The contraction causes the diagonal pore diameter between fluorine atoms to shrink to 3.72 Å, compared to the diameter of 3.79 Å previously observed in the reported framework at 100 K and the diameter of 3.84 Å that is observed at room temperature.[2, 14] While this is primarily due to the overall framework contraction, it is also in some part due to the elongation of the Si – F equatorial bonds from 1.664 Å in the reported structure at 100 K, to 1.669 Å in the CO_2 loaded structure. This elongation of the bonds brings the F atom closer the adsorbed CO_2 molecule, and is likely due to strong interactions between the fluorine atom and the adsorbed CO_2 molecule.
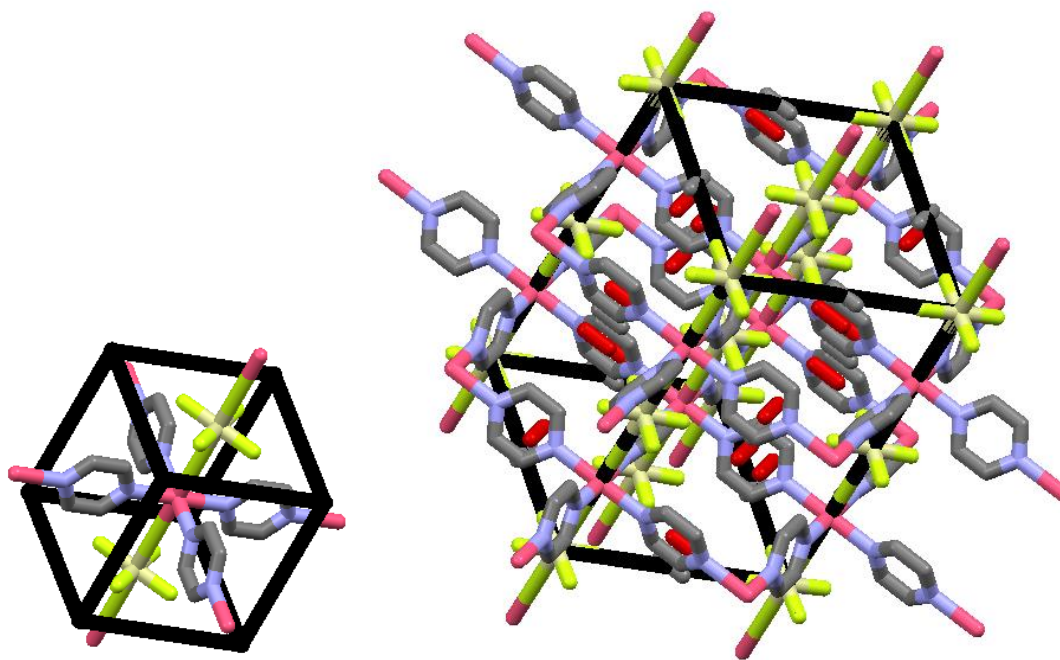
Figure 2.6: A comparison of the unit cell of the empty SIFSIX-3-Zn (left) and CO_2 loaded SIFSIX-3-Zn (right). Unit cell bounds are outlined in black. The presence of disordered CO_2 within the channels significantly redefines the unit cell parameters in SIFSIX-3-Zn.

Adjacent pyrazine rings within the framework are no longer coplanar with each other, as they are reported to be at room temperature. Instead, the rings are found to be tilted into the channels, in alternating directions. This behaviour is displayed in Figure 2.7. The planes of the pyrazine rings form an angle of 22.9 ° with respect to the *c*-axis. Previous structural studies of SIFSIX-3-Zn at 100 K report that the pyrazine rings were slanted at an angle of 13.9 °,[14] while previous computational studies of SIFSIX-3-Zn using density functional theory found that the pyrazine rings were slanted at an angle of 17.2 °, at a temperature of 195 K.[13] This enhanced angling of the pyrazine rings is due to the presence of host-guest interactions, as it brings the

framework protons closer to the centre of the channel, which would increase the strength of their dipolar interactions with the adsorbed carbon atom.

A: CO₂ Loaded, 110 K
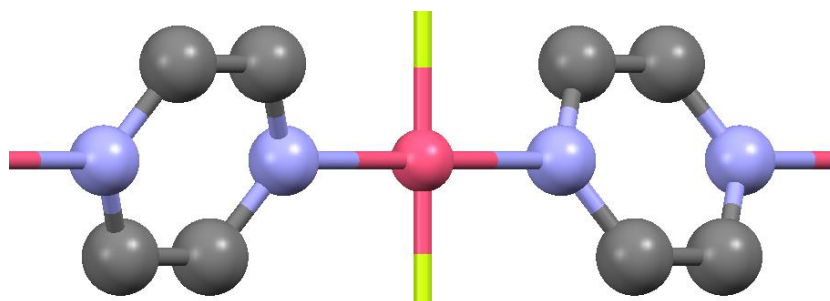
B: As Made, 293 K
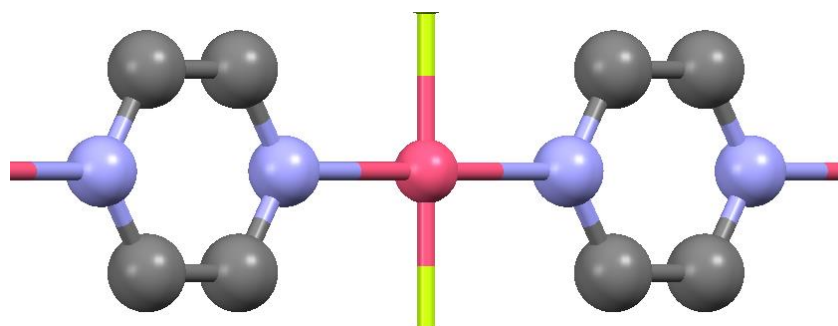
C: CO₂ Loaded, 110 K
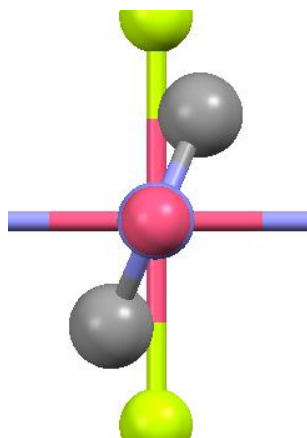
D: As Made, 293 K
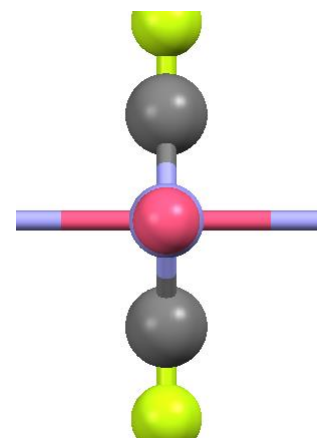
Figure 2.7: The 22.9 ° slanting of the pyrazine rings in the CO₂ loaded framework is depicted above as viewed along the a-axis (A), and contrasted with the parallel rings of the as made framework (B). This tilting is also depicted along the a-axis of the CO₂ loaded framework (C) and compared with the as made framework (D). Adjacent pyrazine rings are slanted in opposing directions. The slanting brings the framework protons closer to the guest CO₂ molecule, enhancing guest-framework interactions.

A: CO₂
Loaded, 110 K
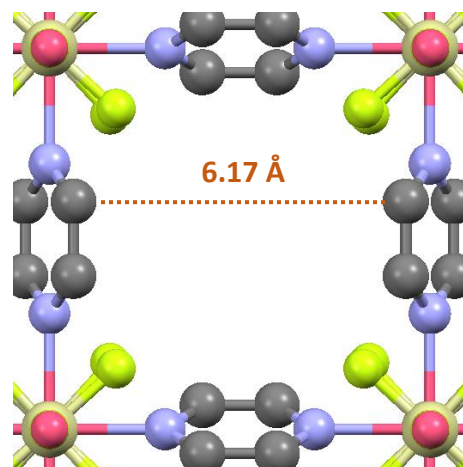
B: As Made,
293 K
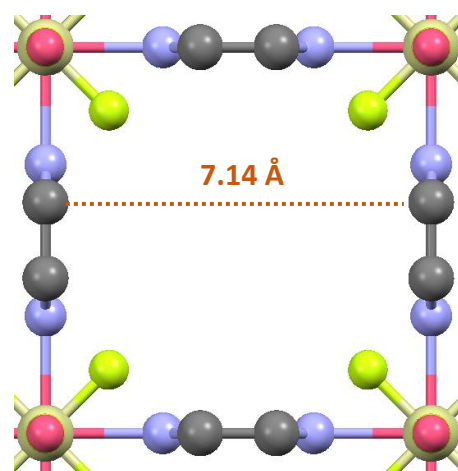
Figure 2.8: A view of the channels in the CO₂ loaded SIFSIX-3-Zn framework is depicted above, as viewed along the c-axis (A). This is contrasted with a view of the channels in the as made framework (B). The pyrazine slanting brings carbon nuclei into the channel, decreasing the proximity between carbon nuclei across the channel. This limits the available space within the channels. Accounting for van der Waals radii, the space between opposite pyrazine carbon nuclei across the channel diameter of the CO₂ loaded is only 2.77 Å. This is believed to limit the mobility of CO₂ in the framework and result in low CO₂ uptakes at low temperatures.[13, 14]

The pyrazine slanting is also found to bring carbon nuclei within the linkers on opposite sides of the channel closer together, shortening C – C distances by 0.4 Å. This feature is depicted in Figure 2.8. Pyrazine slanting in SIFSIX-3-Zn has previously been used to explain low CO₂

uptake at lower temperatures, due to pore blockage restricting the movement of CO_2 within the framework.[13, 14] Given the additional slanting observed after CO_2 adsorption, the pyrazine slanting can be expected to further limit guest molecule mobility within the channel, in addition to strengthening host-guest interactions. The additional contraction of the CO_2 loaded structure also likely contributes to the lower CO_2 uptake at low temperatures, as it would further restrict the movement of guest CO_2 molecules.

Table 2.3: Select structural parameters of SIFSIX-3-Zn are listed below Previous studies have characterized the empty SIFSIX-3-Zn framework. When compared with the values obtained for the CO_2 loaded phase, the structure is further contracted, and the pyrazine linkers are angled more strongly. Zn centers and pyrazine linkers were placed at special positions with no error.

Structural parameter	SIFSIX-3-Zn, 298 K[2]	SIFSIX-3-Zn, 100 K[14]	SIFSIX-3-Zn, CO_2 loaded, 110 K
Zn to Zn distance (*a*)	7.1409 Å	7.1151 Å	7.065 Å
Zn to Zn distance (*c*)	7.6068 Å	7.5747 Å	7.544 Å
Si – F (equatorial) bond length	1.657(4) Å	1.664(1) Å	1.669(1) Å
Diagonal pore diameter (F to F)	3.84(1) Å	3.79(1) Å	3.72(1) Å
Pyrazine angling	-	13.9(1) °	22.9(1) °
Distance between pyrazine linkers across pore length	7.1409 Å	6.573(6) Å	6.173(4) Å

Changes in the structural parameters from those of the reported SIFSIX-3-Zn framework are summarized in Table 2.3. The effects of CO_2 on framework contraction, while subtle, are in some respects more significant than the effects of a temperature change from 298 K to 100 K. These changes would promote stronger interactions between the framework and the guest CO_2 within the framework channels. The use of SCXRD has in this case identified the exact location

of CO_2 within the framework, as well as highlighted the effects of the electrostatic interactions between SIFSIX-3-Zn and the framework molecules.

2.3.2 Variable temperature (VT) static ^{13}C SSNMR of $^{13}CO_2$ loaded SIFSIX-3-Zn

While SCXRD experiments provide detailed structural information, their ability to provide motional information is limited. The low temperatures required to observe the guest molecules limits molecular motion, and SCXRD only provides a time averaged picture of the structure. A detailed understanding of the motional behaviour of guest CO_2 molecules can instead be obtained using SSNMR.

Experimental and simulated ^{13}C NMR spectra were collected for static $^{13}CO_2$ loaded SIFSIX-3-Zn at temperatures between 153 K and 393 K, and can be seen in Figure 2.9. There is no evidence of any free CO_2 within this MOF; gaseous non-adsorbed CO_2 would appear as a single sharp resonance at 126 ppm, which is not observed. CO_2 appears to be adsorbed at all experimental temperatures, which ranged from 153 K to 393 K.

The apparent CS parameters determined through WSolids[45] simulations are listed in Table 2.4. SSNMR powder patterns can be described by their isotropic CS in ppm (δ_{iso}), by their span in ppm (Ω) and by their skew (κ). The known parameters of solid CO_2 patterns are a δ_{iso} of 126 ppm, a Ω of 335 ppm and a κ of 1.00.[47] The Ω changes to 288 (2) ppm at 393 K, and decreases to 315 (5) ppm at 153 K. The κ reaches 1.00 (3) at 193 K and drops to 0.98 (2) at 393 K. The observed CS parameters are comparable those of solid CO_2, and show only minimal changes as the temperature increases. As the CO_2 is adsorbed to the framework it becomes less mobile, increasing CSA. The more immobile the molecule, the more similar its powder pattern is to that of solid CO_2.
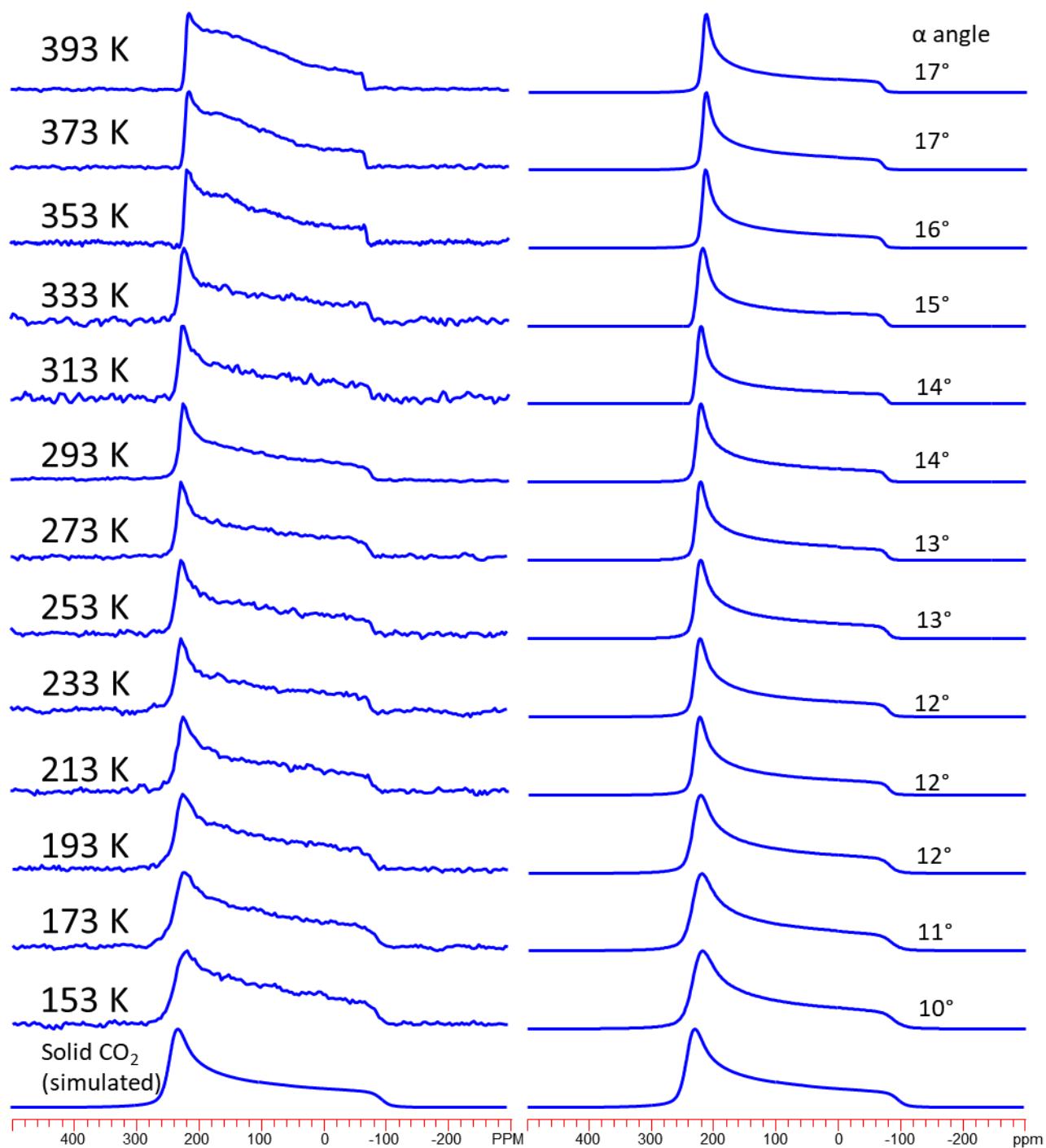
Figure 2.9: The experimental (left) and simulated (right) ^{13}C NMR spectra of $^{13}CO_2$ loaded SIFSIX-3-Zn are shown at temperatures of 393 K to 153 K. Spectra were collected using between 600 and 900 scans and a 5 s recycle delay, except at 293 K where 4000 scans and a 15 s recycle delay was used. C_6 motion of the CO_2 described by α angles listed on the simulated spectra. Simulated spectra of solid CO_2 depicted on the bottom for reference.[47]

The kind of CO_2 powder patterns displayed by SIFSIX-3-Zn is extremely unusual compared to previously studied MOFs.[27, 31, 32, 50, 51] Typically the very broad, highly skewed patterns shown here are only obtained at very low temperatures, where the CO_2 molecule is highly immobile. At higher temperatures, the patterns are expected to become narrower and less skewed.

Table 2.4: The observed ^{13}C chemical shift parameters of CO_2 adsorbed within SIFSIX-3-Zn are listed below. These parameters were obtained from analytical simulations of static ^{13}C SSNMR spectra using WSolids.[45]

Temperature (K)	δ_iso (ppm)	Ω (ppm)	κ
393	123 (1)	288 (2)	0.98 (2)
373	123 (1)	288 (2)	0.98 (2)
353	123 (1)	290 (2)	0.98 (2)
333	124 (1)	300 (2)	0.98 (2)
313	124 (1)	303 (2)	0.98 (2)
293	125 (1)	303 (2)	0.98 (2)
273	125 (1)	305 (2)	0.98 (2)
253	125 (1)	307 (2)	0.98 (2)
233	125 (1)	308 (2)	0.98 (2)
213	125 (1)	309 (2)	0.98 (2)
193	125 (2)	310 (2)	1.00 (3)
173	124 (2)	312 (4)	1.00 (3)
153	123 (2)	315 (5)	1.00 (4)

A notable comparison can be made with the ultramicroporous α-Mg formate MOF, containing pores 4.5 by 5.5 Å across and no OMSs. ^{13}C SSNMR of the CO_2 loaded MOF produced narrow patterns with Ω values between 30 and 69 ppm across all temperature ranges,[51] indicating a much greater degree of molecule mobility than what was observed in SIFSIX-3-Zn. Molecular dynamics simulations and CP SSNMR experiments suggested the adsorption within α-Mg formate

was due to interactions between the CO_2 molecule and the hydrogen nucleus on the formate linker which extended into the channel. There is a ~3.2 Å distance between the proton and the CO_2 oxygen nuclei, and a ~3.9 Å distance between the proton and CO_2 carbon nuclei. This is notably greater than the respective 2.935 Å and 3.438 Å H to O and H to C distances identified by SCXRD within SIFSIX-3-Zn. The confined SIFSIX-3-Zn pore promotes close proximity and strong interactions with multiple fluorine and hydrogen nuclei extending into the channel, with the CO_2 molecule being in close proximity to eight hydrogen nuclei and four fluorine nuclei within the channels.

Therefore, though the pores in SIFSIX-3-Zn are only slightly smaller than those in α-Mg formate, the powder patterns are significantly broader, highlighting the sensitive relationship between the nature of the pore and guest molecule behaviour. This is direct evidence of the confined nature of CO_2 within the framework pores and the strong interactions of CO_2 with the SIFSIX framework. Even at high temperatures, the CO_2 molecule in SIFSIX-3-Zn is unusually immobile compared to previously studied ultramicroporous frameworks. This immobility has been quantified using simulations.

Simulations using EXPRESS[46] allow for precise determination of the nature of CO_2 motions. The simulated powder pattern is consistent with a modelled six-fold (C_6) rotation through a rotational angle α. In practice, the molecule would be rotating through all positions on the rotational cone, as shown in Figure 2.10. The motional angles of C_6 rotation are listed in Figure 2.9, with an estimated error of 1°. The motional rate was found to be at least 10^7 Hz, which lies in the fast-motion regime of NMR dynamics. The C_6 rotation occurs upon a single localized adsorption site within SIFSIX-3-Zn, and simulations show this angle to be 10° at low temperatures, gradually increasing to 14° at room temperature and 17° at 393 K. No change in α at higher

temperatures was observed. Although a non-localized hopping motion has been observed via SSNMR for CO_2 in a variety of other MOFs,[27, 31, 32, 50] conclusive evidence of hopping between sites was not observed in SIFSIX-3-Zn, likely due to the relatively small dimensions of the channels in SIFSIX-3-Zn.
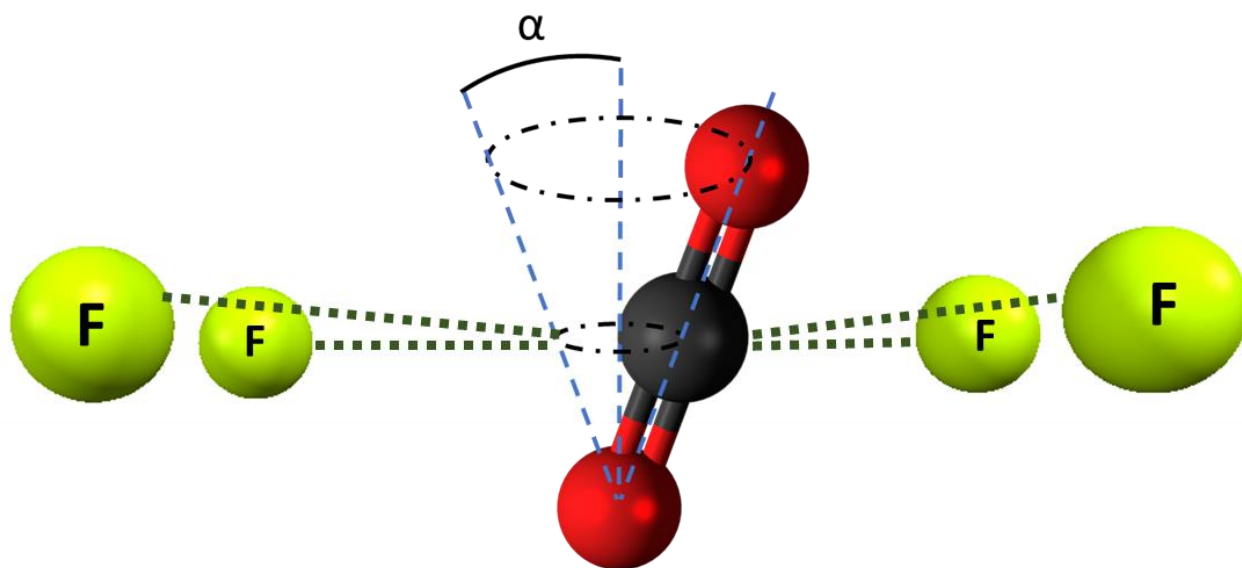
Figure 2.10: The wobbling motion of a CO_2 molecule is shown above, as it interacts with the fluorine atoms extending into the pore. This wobbling is described by the angle α. For the purposes of EXPRESS[46] simulations, the motions are modelled as a six-fold (C_6) rotation. In practice, the molecule would be rotating about a continuous cone.

In summary, VT static ^{13}C SSNMR provided qualitative and quantitative data regarding the motion of CO_2 within the SIFSIX-3-Zn framework, and showed CO_2 to be relatively immobile and strongly adsorbed within the framework. Wobbling modelled by a C_6 rotation of the molecule upon the adsorption site was determined to occur within the framework. The wobbling angles had little temperature dependence, varying between 12° and 19° between 153 K and 393 K, and all wobbling rates were in the fast motion regime.

2.3.3   Static ^{13}C CP SSNMR of ^{13}CO$_2$ loaded SIFSIX-3-Zn

The immobile nature of CO_2 within the SIFSIX-3-Zn framework pores is suggestive of strong interactions with the framework. The existence of such interactions can be verified with CP experiments, which gauge the distance of different nuclei through the dipolar interaction. Room temperature ^{1}H-^{13}C CP SSNMR experiments were performed on the ^{13}CO$_2$ loaded framework, using contact times (CTs) of 0.5 ms, 2.0 ms, 5.0 ms, 7.0 ms and 10.0 ms. The CT refers to the duration of time in which contact pulses are applied to transfer magnetization between different nuclear spins. As the dipolar coupling mediating CP experiments is related to distance by a factor of one over r^3, the contact time can be used to gauge the internuclear distances, as longer contact times are required for resonance enhancement of more distant nuclei. CP is also sensitive to motion, as motion will average the dipolar interaction and reduce CP efficiency. The room temperature and 153 K spectra can be seen in Figure 2.11 in blue.

When conducting ^{1}H-^{13}C CP experiments on the activated framework, the spectra show a broad resonance from the carbon in the pyrazine linkers (Figure 2.11, red). The spectra of the CO_2 loaded framework are easily distinguishable due to additional intensity from the adsorbed ^{13}CO$_2$, resulting in a skewed lineshape characteristic of immobile CO_2. This intensity becomes increasingly apparent when using long CTs, with the pattern intensity increasing steadily as the CT grows longer. The increasing intensity of the CO_2 resonance with longer CTs is suggestive of longer distances between the adsorbed CO_2 and the framework nuclei. Based on the SCXRD, there is a 3.438 Å distance between framework ^{1}H nuclei and adsorbed ^{13}C nuclei. The C – H bond in the framework is 0.951 Å.

Low temperature ^{1}H-^{13}C CP experiments were also performed on the ^{13}CO$_2$ loaded SIFSIX-3-Zn framework at a temperature of 153 K. Based on the static ^{13}C SSNMR experiments

outlined above, guest CO_2 molecules are expected to be less mobile at this temperature, which results in less modulation and dephasing of the dipolar interaction, thus, the effective dipolar coupling between framework and guest molecules is expected to be stronger. However, as the CO_2 molecule in SIFSIX-3-Zn is relatively immobile even at room temperature, there is little observable difference in the pattern intensity and shape at low temperatures compared to room temperature.
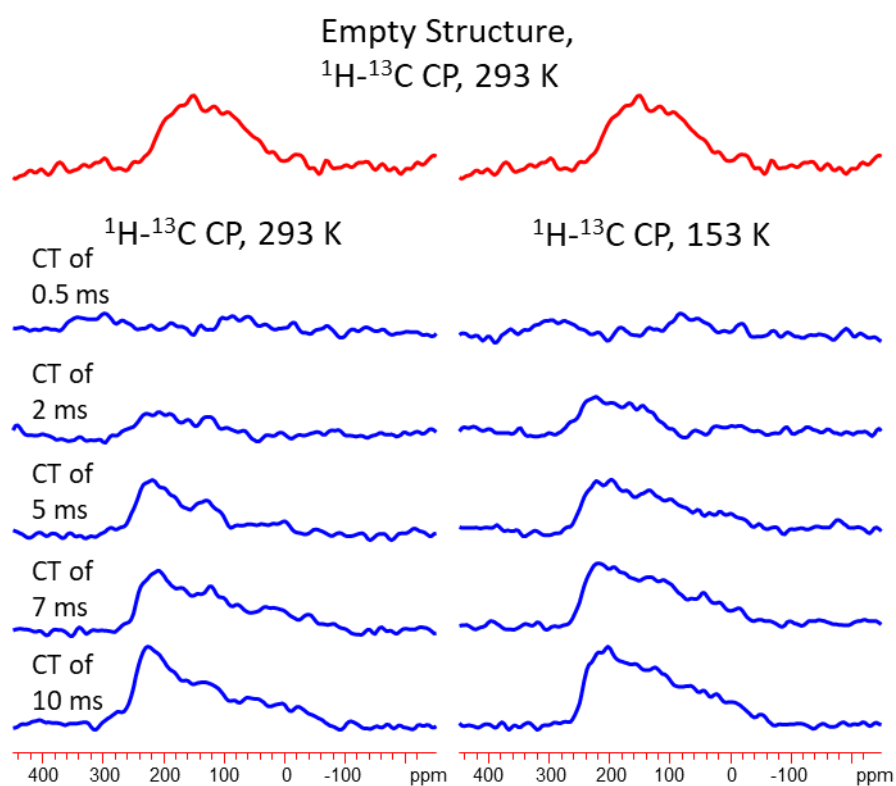
Figure 2.11: The room temperature ^1H-^{13}C (left, 5000 scans) and low temperature ^1H-^{13}C (right, 3000 scans), static CP spectra of $^{13}CO_2$ loaded SIFSIX-3-Zn are depicted in blue. A pulse delay of 2 s was used. They were collected using various CTs, listed to the left of the spectra. In red, the ^1H-^{13}C static CP spectrum of the activated SIFSIX-3-Zn framework is shown for comparison. The red spectrum was collected using 13 000 scans, a pulse delay of 1 s, and a CT of 10 ms.

CP experiments show that adsorbed CO_2 is sufficiently proximate to interact with ^1H within SIFSIX-3-Zn, as the $^{13}CO_2$ resonance is apparent in ^1H-^{13}C CP CP SSNMR at room temperature. Similar results are obtained at 153 K as at 293 K, due to the relative immobility of the guest molecule at all experimental temperatures. A better understanding of the effects of CT can be determined through CP/MAS experiments.

2.3.4 ^{13}C direct MAS and CP/MAS SSNMR of $^{13}CO_2$ loaded SIFSIX-3-Zn

The immobility and strong adsorption of CO_2 within the SIFSIX-3-Zn framework allow for MAS experiments to be performed on the CO_2 loaded MOF. This is relatively uncommon, with only two reported studies of MAS SSNMR on CO_2 loaded physisorbent MOFs.[52, 53] The use of MAS SSNMR allows for higher resolution spectra to be collected, allowing for a more precise look at the CO_2 adsorption sites and the effects of CP on the adsorbed ^{13}C nuclei.

^{13}C MAS, ^1H-^{13}C CP/MAS and ^{19}F-^{13}C CP/MAS spectra were collected and are shown in Figure 2.12. Within the direct-excitation ^{13}C spectra, a sharp signal can be observed at 124 (1) ppm, which is consistent with the δ_{iso} obtained from static ^{13}C spectra, and can therefore be inferred as belonging to the adsorbed CO_2 within the framework. No CO_2 signals corresponding to a second adsorption site or free CO_2 are evident, consistent with the SCXRD structure. A second, much broader and less intense signal is observed at 146 (1) ppm. This signal corresponds to the carbon atoms of the pyrazine linker in the framework, which have an expected δ_{iso} of 145.9 ppm.[54] This signal is much less intense than that of the adsorbed $^{13}CO_2$, due to the low natural abundance of ^{13}C in the linker versus the enriched abundance of ^{13}C in $^{13}CO_2$. Spinning sidebands are also observed for the adsorbed CO_2 signal, 15000 Hz from the main signal, due to the spin rate of 15.000 kHz. A slow spinning MAS NMR spectrum at a spinning rate of 2010 Hz was also collected for the CO_2 loaded SIFSIX-3-Zn. The δ_{iso} of $^{13}CO_2$ was unchanged in this spectrum, although the

sidebands were brought closer to the central resonance in a shape demonstrating the effects of CSA, as was observed in the static spectra (see Figure 2.9 above).
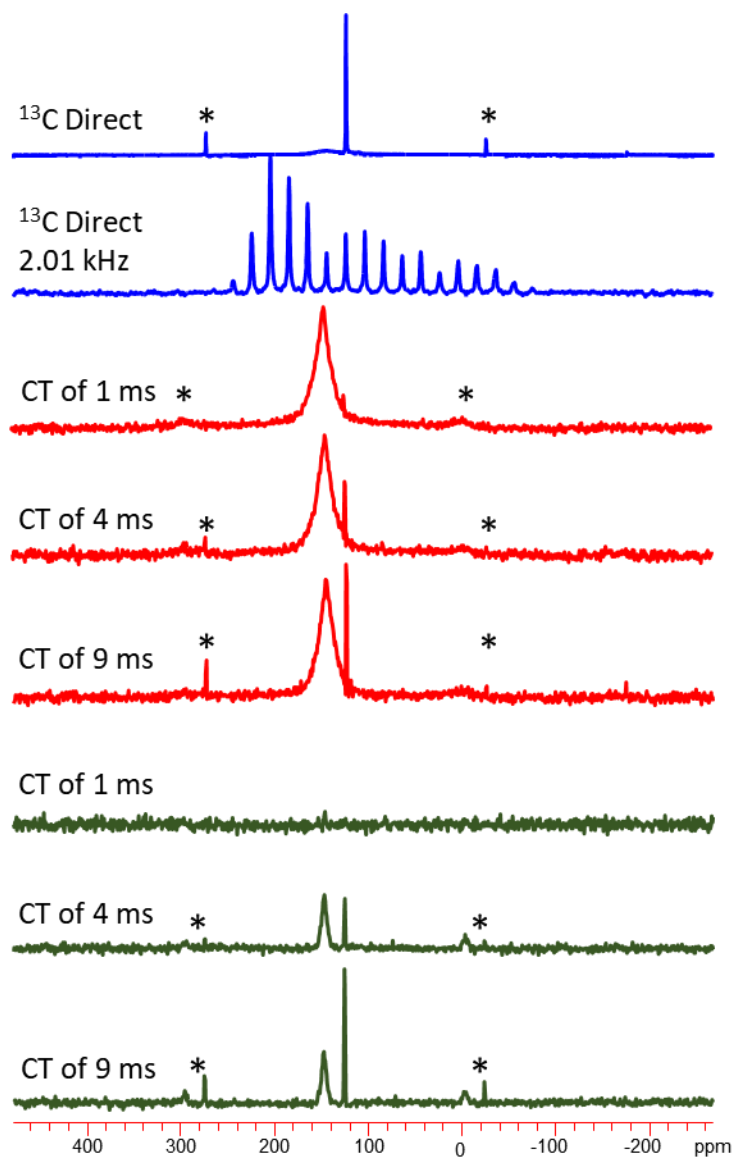
Figure 2.12: The experimental ^{13}C NMR spectra of $^{13}CO_2$ loaded SIFSIX-3-Zn, when subjected to MAS SSNMR experiments, are all depicted above. The blue spectra were collected via direct-excitation of ^{13}C nuclei, using between 2000 and 3000 scans and a 3 s pulse delay. The red spectra were collected using ^{1}H-^{13}C CP, between 1000 and 2000 scans and a 2 s pulse delay., The green spectra were collected using ^{19}F-^{13}C CP, 1000 scans and a 1 s pulse delay. The contact times used for CP are listed to the left of the spectra. The spinning rate of the sample is 15.000 kHz unless otherwise noted. Notable sideband locations at 15 kHz are indicated by asterisks.

^{1}H-^{13}C CP/MAS experiments were also performed on the ^{13}CO$_2$ loaded SIFSIX-3-Zn framework. Based on the SCXRD structure, there are four ^{1}H nuclei 3.438 Å from each adsorbed ^{13}C nucleus, and four ^{1}H nuclei 3.789 Å from each ^{13}C nucleus. This should result in a calculated dipolar coupling constant of 743.5 Hz between the adsorbed ^{13}C nucleus and the closest ^{1}H nucleus. As the protons within SIFSIX-3-Zn are directly bound to the carbon atoms in the pyrazine linker, the signal from the linker is dramatically enhanced. As the CT grows longer, the polarization transfer from ^{1}H to the adsorbed ^{13}C nuclei of ^{13}CO$_2$ becomes more efficient. The ^{13}CO$_2$ signal becomes more enhanced, clearly showing the effects of a stronger CT on the adsorbed ^{13}CO$_2$ molecule.

Similar results were also obtained using ^{19}F-^{13}C CP/MAS experiments on the ^{13}CO$_2$ loaded framework, though the signal from the linker is significantly diminished when using low CTs as there is no direct bond connecting the fluorine to the pyrazine. There are two fluorine atoms 2.958 Å from the adsorbed carbon nuclei based on structure obtained using SCXRD, and two fluorine atoms 3.746 Å from the adsorbed carbon nuclei. The dipolar interaction between one ^{13}C nucleus and a single proximate ^{19}F nucleus has a calculated value of 4369 Hz. The distance between fluorine atoms and the framework carbon nuclei is 3.309 Å, however longer CTs appear to have a greater effect on the adsorbed carbon resonance, likely due to the averaging effect of the CO$_2$ motion on the dipolar interaction.

A series of CT arrays (described in Figure 2.13) relating the area of the ^{13}CO$_2$ resonance to the contact time was constructed using identical acquisition parameters at a variety of CTs on a sample spinning at 10 kHz, using both ^{1}H-^{13}C and ^{19}F-^{13}C CP/MAS experiments. They were constructed at both 293 K and 223 K. The intensity of the resonance was determined through simulating the signal with a Lorentzian line fit.
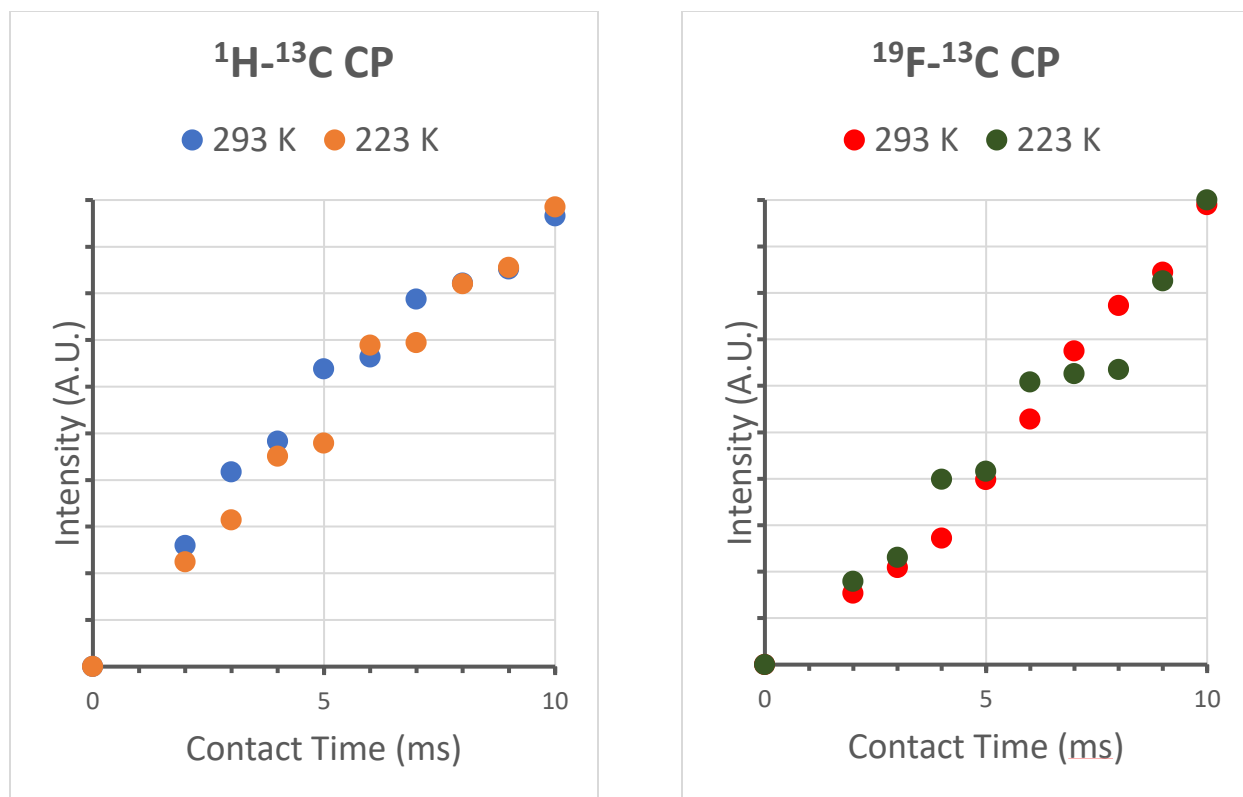
Figure 2.13: Two scatter plots displaying the relationship between relative signal intensity and contact time in ^1H-^{13}C and ^{19}F-^{13}C CP experiments on CO_2 loaded SIFSIX-3-Zn are shown above. The CT used appeared to be proportional to the intensity in all studied cases, suggesting that the dipolar interaction between the nuclei used were not changing notably.

During magnetization transfer, the magnetization of ^1H and ^{19}F relaxes with a characteristic time $T_{1\rho}$. This causes the resonance intensity to eventually plateau due to the effects of magnetization relaxation,[55] however this appears to require a CT of greater than 10 ms in the case of the guest ^{13}C nuclei, likely due to the mobility of the CO_2 within the pores. The consistent shape of the intensity vs. CT curve regardless of temperature suggests that the location of the CO_2 molecule relative to the framework atoms does not change significantly as the temperature is reduced from 293 K to 223 K. This means that the effects of motion on the dipolar interaction are not significantly changing as the temperature decreases. This is due to the low temperature

dependence of the motions as determined based on the ^{13}C SSNMR powder pattern, with the CO_2 being relatively immobile at both room temperature and low temperatures.

These experiments provide additional information on the framework interactions with the single CO_2 adsorption site within SIFSIX-3-Zn. This adsorption site is sufficiently close to both the pyrazine and SiF_6^{2-} linker dipolar interactions between the CO_2 and both the hydrogen and fluorine atoms occur. This is due to the narrowness of the channels in the ultramicroporous framework and the proximity between the guest molecule and the multiple fluorine and hydrogen nuclei extending into the channel. There is little relationship between the temperature and strength of the dipolar interaction, due to the low mobility of the CO_2 at all temperatures.

2.3.5 ^{13}C REDOR SSNMR of $^{13}CO_2$ loaded SIFSIX-3-Zn

REDOR based experiments using ^{1}H-dephasing were explored for their potential to investigate the strength of the dipolar coupling between the framework and guest molecules in more detail. CP experiments had already confirmed that such interactions occurred. REDOR experiments offer an alternative strategy to exploring the dipolar interaction.[55, 56] Using an initial excitation pulse on the ^{13}C spin and then multiple rotor synchronized dephasing pulses applied to a second spin, a reduced spectrum S_r is produced. The magnitude of the dephasing is dependant on the strength of the dipolar interaction and the length of the dephasing time.

A sample room temperature ^{1}H-dephased ^{13}C REDOR spectrum can be observed in Figure 2.14. The full spectrum (S_0), dephased spectrum (S_r), and difference spectrum (ΔS) are all depicted. The dephasing lasted for 28 rotor periods at a spinning speed of 10.000 kHz, for a total dephasing time of 0.0028 s. The ratio between the difference and full spectra (the $\Delta S/S_0$ value) is 0.12 after this dephasing time.
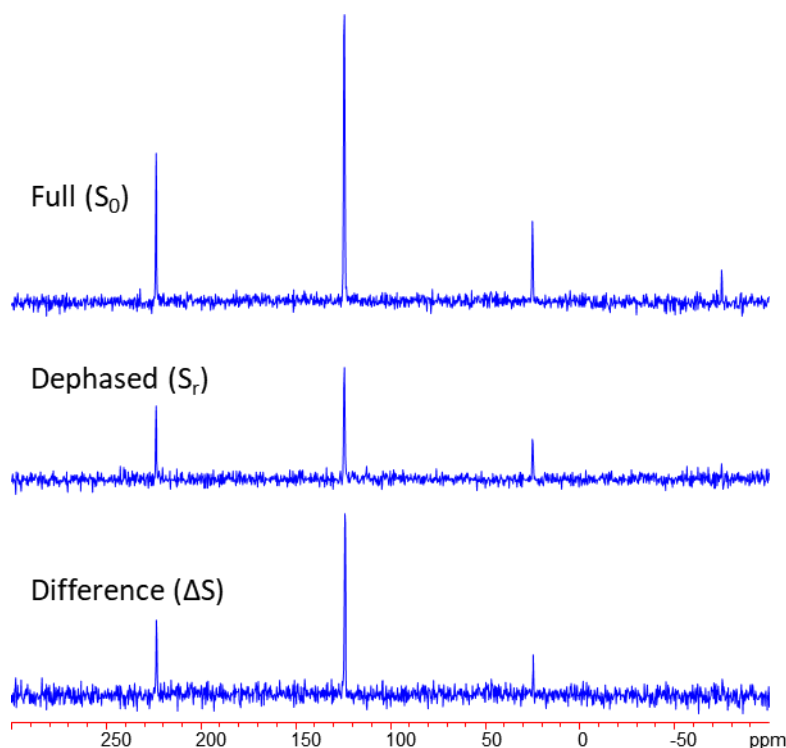
Figure 2.14: The experimental ^1H-dephased ^{13}C REDOR SSNMR spectra of $^{13}CO_2$ loaded SIFSIX-3-Zn are shown above. These spectra collected while spinning at 10.000 kHz with 400 scans and a 3.0 second recycle delay. The dephased spectrum was collected using a dephasing time of 0.02 s.

Full REDOR arrays were collected at 293 K and 223 K, using dephasing times from 0.001 s up to 0.025 s. This data was used to form a curve relating the maximum intensity of $\Delta S/S_0$ to the dephasing time, shown in Figure 2.15 on the left. The magnitude of the dephasing is slightly stronger at lower temperatures, likely a result of decreased CO_2 mobility at lower temperatures, resulting in less motional averaging and a stronger effective dipolar coupling. This difference was not detected in the CP SSNMR experiments, however the REDOR experiments possess greater sensitivity and provide a more quantitative description of the dipolar interaction.

REDOR experiments utilizing ^{19}F dephasing were also conducted on the SIFSIX-3-Zn framework. REDOR arrays were collected at 293 K and 223 K, using dephasing times up to 0.020

s. The resulting curve showing the relationship between $\Delta S/S_0$ and the dephasing time can be seen in Figure 2.15 on the right. The $\Delta S/S_0$ values were similar at 293 K and 223 K. Furthermore, at a given dephasing time, the $\Delta S/S_0$ is smaller than what was observed when using ^1H dephasing. This would be in part due to the lower gyromagnetic ratio of ^{19}F compared to ^1H, and in part due to the smaller number of ^{19}F nuclei than ^1H nuclei within the framework.
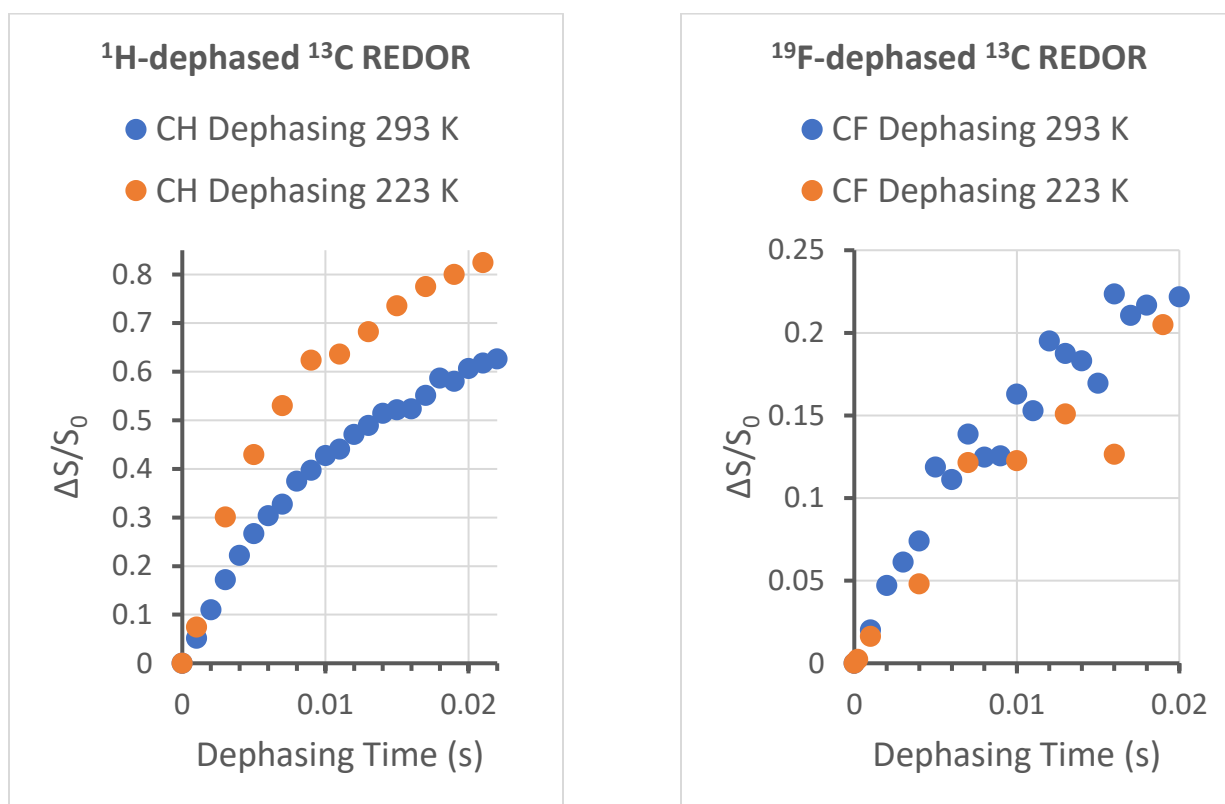
Figure 2.15: Scatter plots displaying the relationship between ΔS/S0 and the dephasing time for experimental ^1H-dephased ^{13}C REDOR and experimental ^{19}F-dephased ^{13}C REDOR SSNMR spectra of $^{13}CO_2$ loaded SIFSIX-3-Zn are depicted.

The effective dipolar interaction is significant as was determined through both REDOR and CP/MAS experiments. However, the CO_2 motion averages this interaction, despite the small motional angles, relatively low mobility, and low degree of temperature dependence that were

determined for CO_2 motion within SIFSIX-3-Zn through static ^{13}C SSNMR experiments. These results are also consistent with the results of ^{13}C SSNMR experiments using varying decoupling fields on the sample, which were unable to distinguish between samples when different decoupling fields were applied, despite the supposed proximity between the CO_2 molecule and the framework nuclei (Figure S2.2).

2.3.6 Static ^{67}Zn SSNMR of as made, water exposed, activated and $^{13}CO_2$ loaded SIFSIX-3-Zn

While CP and REDOR experiments provided information on the interactions between the guest molecules and the ^{19}F and ^{1}H nuclei, investigation of the local environment around the ^{67}Zn nuclei required the use of high field SSNMR. This is due to the low abundance (4.1%), low gyromagentic ratio (1.677×10^7 rad T^{-1} s^{-1}, or 2.669 MHz T^{-1}), and a moderate nuclear quadrupole moment (150 mbarn) of ^{67}Zn.[57] High field ^{67}Zn NMR experiments offer insight into the local environment of the Zn^{2+} ion within the SIFSIX-3-Zn framework. The Zn^{2+} ion is bound to four equatorial pyrazine linkers, and two axial SiF_6^{2-} pillars, in an octahedral fashion. Unlike ^{13}C, ^{67}Zn is a quadrupolar nucleus. The primary factors describing the QI, and by extension the ^{67}Zn NMR, are the quadrupolar coupling parameter (C_Q) and the asymmetry parameter (η_Q).

The C_Q value is a measure of the strength of the QI between the electric nuclear quadrupole moment and the electric field gradient (EFG) produced by the local environment.[55] The C_Q value is correlated with spherical symmetry about the nucleus, with rising C_Q values indicating less spherically symmetric environments, leading to broader SSNMR powder patterns. The η_Q value is a measure of the axial symmetry of the EFG tensor, and varies between 0 and 1.[55] A η_Q of 0 indicates a perfectly axially symmetric EFG tensor and the presence of a C_n rotational axis where $n \geq 3$, while a η_Q of 1 indicates low axial symmetry.

The ^{67}Zn SSNMR spectra can be observed in Figure 2.16. C_Q and η_Q parameters were obtained for the as made, activated, and CO_2 loaded phases of SIFSIX-3-Zn, with the as made phase containing methanol solvent in the pores. These parameters were obtained from experimental ^{67}Zn SSNMR powder patterns and were compared to results from computational methods using the CASTEP software package,[48] shown in Table 2.5.

Table 2.5: The observed and calculated ^{67}Zn QI parameters of SIFSIX-3-Zn samples are listed below. These parameters were obtained from analytical simulations of ^{67}Zn SSNMR spectra and calculated for the reported and geometry optimized structures of SIFSIX-3-Zn.

Sample	C_Q (MHz)	η_Q
As Made	16.0 (1)	0.04 (2)
Activated	13.5 (1)	0.03 (1)
CO_2 Loaded	13.6 (1)	0.03 (1)
Calculated, Activated	13.93	0.00
Calculated, Activated, Geometry optimized	15.50	0.00

The as made SIFSIX-3-Zn ^{67}Zn powder patterns correspond to large C_Q values, of 16.0 MHz, and near-zero η_Q values. This indicates a low degree of spherical symmetry about the Zn nucleus but a high degree of axial symmetry. Six-coordinate Zn centres usually have a high degree of spherical symmetry, with C_Q values as high as 16.0 MHz being unusual.[58] The low spherical symmetry is likely due to the presence of unequal numbers of multiple ligand types, with both pyrazine and SiF_6^{2-} ligands on the Zn^{2+} ion. The high axial symmetry is due to the C_4 rotation axis about the *c*-axis, formed by the four pyrazine linkers. The C_Q became smaller after activation when the adsorbed methanol was removed, with the C_Q dropping from 16.0 MHz to 13.5 MHz. The C_Q and η_Q values for the activated framework are in good agreement with the values obtained from

calculations using the reported empty structure,[2] with a difference of roughly 4% between experimental and calculated C_Q. Calculations for a geometry optimized framework of SIFSIX-3-Zn produced a higher C_Q value (15.50 MHz) that was more consistent with experimental results for the as made phase. This indicates that the reported SIFSIX-3-Zn structure is likely accurate for the activated SIFSIX-3-Zn phase.
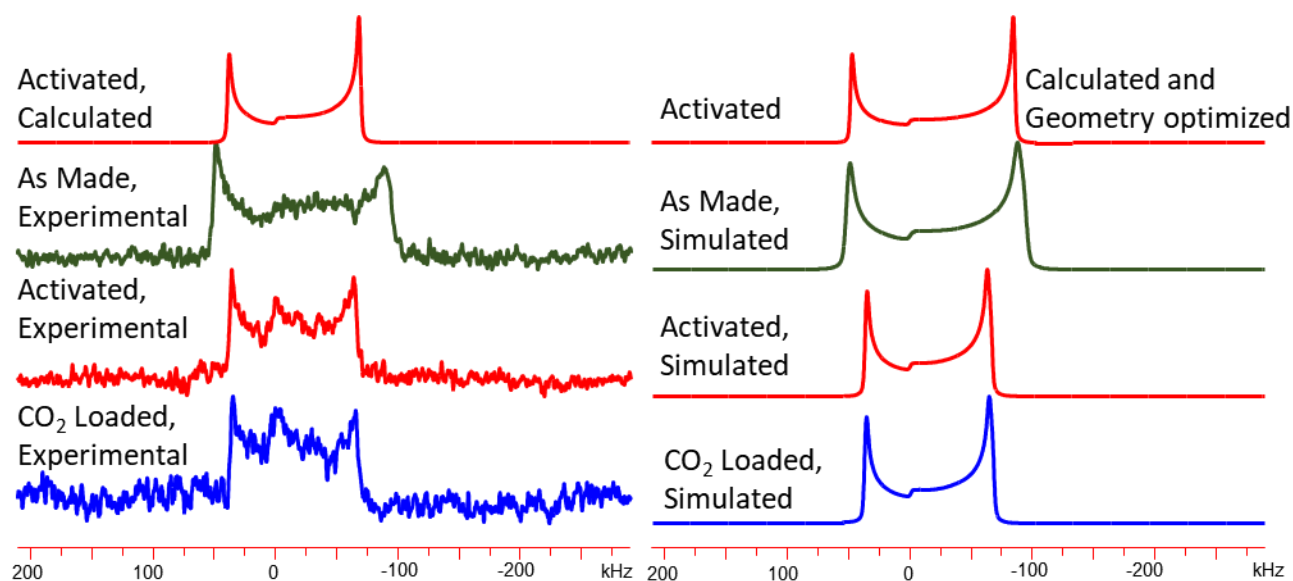
Figure 2.16: The experimental (left) and simulated (right) ^{67}Zn NMR spectra of as made, activated and CO_2 loaded SIFSIX-3-Zn are shown above. Between 224 000 and 400 000 scans were used with a recycle delay of 0.25 s.

While the bond angles around the Zn^{2+} remain 90° in all structures, the $Zn - Si$ and $Zn - N$ bond lengths change. The bond lengths about the Zn for the reported and geometry optimized activated structure are listed in Table 2.6. It can be seen that in the geometry optimized structure, there is a greater difference between the $Zn - Si$ and $Zn - N$ bond lengths, of 0.120 Å rather than 0.115 Å. This accounts for the slightly increased ^{67}Zn C_Q value in the geometry optimized

structure. This suggests that higher C_Q values are correlated with the difference between the Zn – F and Zn – N bond lengths.

Table 2.6: The Zn – F and Zn – N bond lengths are listed below for the geometry optimized and reported structure of SIFSIX-3-Zn. The calculated ^{67}Zn C_Q values are also listed for the purpose of comparison.

Activated Structure	Zn – F bond length (Å)	Zn – N bond length (Å)	Calculated C_Q (MHz)
Reported	2.057(1)	2.172(1)	13.93(1)
Geometry optimized	2.058(1)	2.178(1)	15.50(1)

The as made SIFSIX-3-Zn phase possesses a slightly higher ^{67}Zn C_Q value than the activated and CO_2 loaded phases, comparable to the calculated C_Q of the geometry optimized phase. The activated and CO_2 loaded phases should contain Zn – F bonds and Zn – N bonds that are more similar to each other in length, while the as made phase possesses Zn bonds that are more dissimilar in length.

After CO_2 loading, the experimental C_Q and η_Q remained near identical to those of the activated sample, indicating that CO_2 is not affecting the local structure about the Zn nucleus.

2.4   Conclusions

Using SCXRD, the structure of SIFSIX-3-Zn loaded with CO_2 has been determined. SIFSIX-3 frameworks are known to possess extremely high selectivity for adsorption of CO_2 gas, while possessing no OMSs to promote CO_2 adsorption. The CO_2 adsorption site has been precisely identified, positionally disordered across the inversion centre within the pores. The overall framework structure was also found to contract slightly compared to the empty framework, due to the presence of the CO_2 molecule. This was primarily due to the contraction of the pyrazine linker,

and the Zn – N and Zn – F – Si bonds due to interactions with the CO_2. Bond angles about the Zn and Si nuclei were unchanged. The pyrazine linkers were found to tilt more strongly into the channels, restricting available space for the guest molecules. The equatorial fluorine atoms were similarly found to extend further into the channels after CO_2 loading, further enhancing guest-host interactions.

To supplement these findings, a series of SSNMR experiments have been conducted on the ultramicroporous SIFSIX-3-Zn framework, to explore CO_2 motional behaviour and the interactions between CO_2 and the framework as CO_2 gas is loaded into the structure. ^{13}C SSNMR has shown that the CO_2 gas possesses a high level of immobility within the pores of SIFSIX-3-Zn, displaying only wobbling motions about a 19° α angle at 393 K, with a low degree of temperature dependence. [1]H-^{13}C and ^{19}F-^{13}C CP SSNMR experiments provided information on the dipolar interactions between the framework atoms and guest molecule, showing that such interactions existed. [1]H-^{13}C and ^{19}F-^{13}C REDOR and CP/MAS SSNMR experiments supported the previous CP experiments. The REDOR experiments confirmed a small degree of temperature dependence in the strength of the [1]H-^{13}C dipolar interactions. [67]Zn SSNMR experiments and calculations gave insight into the changes in the metal centre as guest molecules were evacuated and loaded into the framework, and suggested that the C_Q of the Zn nuclei became smaller after methanol evacuation from SIFSIX-3-Zn, due to changes in the Zn – F and Zn – C bond lengths. CO_2 loading did not change the C_Q value, indicating the guest CO_2 does not change the Zn environment to the degree the methanol molecule does.

This chapter illustrates the unusual behaviour of CO_2 guest molecules in SIFSIX-3-Zn, and the changes in the framework structure. It is hoped that continued study in these fields will increase the scientific community's understanding of guest adsorption, and of CO_2 adsorption in particular.

2.5   References

1.   Subramanian, S.; Zaworotko, M. J., POROUS SOLIDS BY DESIGN - ZN(4,4'-BPY)(2)(SIF$_6$) (N)CENTER-DOT-XDMF, A SINGLE FRAMEWORK OCTAHEDRAL COORDINATION POLYMER WITH LARGE SQUARE CHANNELS. *Angewandte Chemie-International Edition* **1995,** *34* (19), 2127-2129.

2.   Nugent, P.; Belmabkhout, Y.; Burd, S. D.; Cairns, A. J.; Luebke, R.; Forrest, K.; Pham, T.; Ma, S.; Space, B.; Wojtas, L.; Eddaoudi, M.; Zaworotko, M. J., Porous materials with optimal adsorption thermodynamics and kinetics for CO2 separation. *Nature* **2013,** *495* (7439), 80-84.

3.   Uemura, K.; Maeda, A.; Maji, T. K.; Kanoo, P.; Kita, H., Syntheses, Crystal Structures and Adsorption Properties of Ultramicroporous Coordination Polymers Constructed from Hexafluorosilicate Ions and Pyrazine. *European Journal of Inorganic Chemistry* **2009,** (16), 2329-2337.

4.   Nugent, P. S.; Rhodus, V. L.; Pham, T.; Forrest, K.; Wojtas, L.; Space, B.; Zaworotko, M. J., A Robust Molecular Porous Material with High CO_2 Uptake and Selectivity. *Journal of the American Chemical Society* **2013,** *135* (30), 10950-10953.

5.   Kumar, A.; Hua, C.; Madden, D. G.; O'Nolan, D.; Chen, K. J.; Keane, L. A. J.; Perry, J. J.; Zaworotko, M. J., Hybrid ultramicroporous materials (HUMs) with enhanced stability and trace carbon capture performance. *Chemical Communications* **2017,** *53* (44), 5946-5949.

6.   Mohamed, M. H.; Elsaidi, S. K.; Wojtas, L.; Pham, T.; Forrest, K. A.; Tudor, B.; Space, B.; Zaworotko, M. J., Highly Selective CO_2 Uptake in Uninodal 6-Connected "mmo" Nets Based upon MO42- (M = Cr, Mo) Pillars. *Journal of the American Chemical Society* **2012,** *134* (48), 19556-19559.

7.   Bhatt, P. M.; Belmabkhout, Y.; Cadiau, A.; Adil, K.; Shekhah, O.; Shkurenko, A.; Barbour, L. J.; Eddaoudi, M., A Fine-Tuned Fluorinated MOF Addresses the Needs for Trace CO_2 Removal and Air Capture Using Physisorption. *Journal of the American Chemical Society* **2016,** *138* (29), 9301-9307.

8.   Cadiau, A.; Belmabkhout, Y.; Adil, K.; Bhatt, P. M.; Pillai, R. S.; Shkurenko, A.; Martineau-Corcos, C.; Maurin, G.; Eddaoudi, M., Hydrolytically stable fluorinated metal-organic frameworks for energy-efficient dehydration. *Science* **2017,** *356* (6339), 731-735.

9.   Chui, S. S. Y.; Lo, S. M. F.; Charmant, J. P. H.; Orpen, A. G.; Williams, I. D., A chemically functionalizable nanoporous material Cu-3(TMA)(2)(H$_2$O)(3) (n). *Science* **1999,** *283* (5405), 1148-1150.

10.   Caskey, S. R.; Wong-Foy, A. G.; Matzger, A. J., Dramatic tuning of carbon dioxide uptake via metal substitution in a coordination polymer with cylindrical pores. *Journal of the American Chemical Society* **2008,** *130* (33), 10870-+.

11.   Burtch, N. C.; Jasuja, H.; Walton, K. S., Water Stability and Adsorption in Metal-Organic Frameworks. *Chemical Reviews* **2014,** *114* (20), 10575-10612.

12.   Canivet, J.; Fateeva, A.; Guo, Y. M.; Coasne, B.; Farrusseng, D., Water adsorption in MOFs: fundamentals and applications. *Chemical Society Reviews* **2014,** *43* (16), 5594-5617.

13.   Kanoo, P.; Reddy, S. K.; Kumari, G.; Haldar, R.; Narayana, C.; Balasubramanian, S.; Maji, T. K., Unusual room temperature CO_2 uptake in a fluoro-functionalized MOF: insight from Raman spectroscopy and theoretical studies. *Chemical Communications* **2012,** *48* (68), 8487-8489.

14.   Forrest, K. A.; Pham, T.; Hogan, A.; McLaughlin, K.; Tudor, B.; Nugent, P.; Burd, S. D.; Mullen, A.; Cioce, C. R.; Wojtas, L.; Zaworotko, M. J.; Space, B., Computational Studies of CO_2 Sorption and Separation in an Ultramicroporous Metal-Organic Material. *Journal of Physical Chemistry C* **2013,** *117* (34), 17687-17698.

15.   Pham, T.; Forrest, K. A.; McLaughlin, K.; Tudor, B.; Nugent, P.; Hogan, A.; Mullen, A.; Cioce, C. R.; Zaworotko, M. J.; Space, B., Theoretical Investigations of CO_2 and H_2 Sorption in an Interpenetrated Square-Pillared Metal-Organic Material. *Journal of Physical Chemistry C* **2013,** *117* (19), 9970-9982.

16.   Ziaee, A.; Chovan, D.; Lusi, M.; Perry, J. J.; Zaworotko, M. J.; Tofail, S. A. M., Theoretical Optimization of Pore Size and Chemistry in SIFSIX-3-M Hybrid Ultramicroporous Materials. *Crystal Growth & Design* **2016,** *16* (7), 3890-3897.

17.   D'Alessandro, D. M.; Smit, B.; Long, J. R., Carbon Dioxide Capture: Prospects for New Materials. *Angewandte Chemie-International Edition* **2010,** *49* (35), 6058-6082.

18.   Cavenati, S.; Grande, C. A.; Rodrigues, A. E., Adsorption equilibrium of methane, carbon dioxide, and nitrogen on zeolite 13X at high pressures. *Journal of Chemical and Engineering Data* **2004,** *49* (4), 1095-1101.

19.   Kumar, A.; Madden, D. G.; Lusi, M.; Chen, K. J.; Daniels, E. A.; Curtin, T.; Perry, J. J.; Zaworotko, M. J., Direct Air Capture of CO_2 by Physisorbent Materials. *Angewandte Chemie-International Edition* **2015,** *54* (48), 14372-14377.

20.   Madden, D. G.; Scott, H. S.; Kumar, A.; Chen, K. J.; Sanii, R.; Bajpai, A.; Lusi, M.; Curtin, T.; Perry, J. J.; Zaworotko, M. J., Flue-gas and direct-air capture of CO_2 by porous metal-organic materials. *Philosophical Transactions of the Royal Society a-Mathematical Physical and Engineering Sciences* **2017,** *375* (2084).

21.   Shekhah, O.; Belmabkhout, Y.; Chen, Z.; Guillerm, V.; Cairns, A.; Adil, K.; Eddaoudi, M., Made-to-order metal-organic frameworks for trace carbon dioxide removal and air capture. *Nature Communications* **2014,** *5*.

22.   Shekhah, O.; Belmabkhout, Y.; Adil, K.; Bhatt, P. M.; Cairns, A. J.; Eddaoudi, M., A facile solvent-free synthesis route for the assembly of a highly CO_2 selective and H_2S tolerant NiSIFSIX metal-organic framework. *Chemical Communications* **2015,** *51* (71), 13595-13598.

23.   Elsaidi, S. K.; Mohamed, M. H.; Schaef, H. T.; Kumar, A.; Lusi, M.; Pham, T.; Forrest, K. A.; Space, B.; Xu, W. Q.; Halder, G. J.; Liu, J.; Zaworotko, M. J.; Thallapally, P. K., Hydrophobic pillared square grids for selective removal of CO_2 from simulated flue gas. *Chemical Communications* **2015,** *51* (85), 15530-15533.

24.   Park, K. S.; Ni, Z.; Cote, A. P.; Choi, J. Y.; Huang, R. D.; Uribe-Romo, F. J.; Chae, H. K.; O'Keeffe, M.; Yaghi, O. M., Exceptional chemical and thermal stability of zeolitic imidazolate frameworks. *Proceedings of the National Academy of Sciences of the United States of America* **2006,** *103* (27), 10186-10191.

25.   Zhang, K.; Lively, R. P.; Zhang, C.; Chance, R. R.; Koros, W. J.; Sholl, D. S.; Nair, S., Exploring the Framework Hydrophobicity and Flexibility of ZIF-8: From Biofuel Recovery to Hydrocarbon Separations. *Journal of Physical Chemistry Letters* **2013,** *4* (21), 3618-3622.

26.   Zhao, A.; Samanta, A.; Sarkar, P.; Gupta, R., Carbon Dioxide Adsorption on Amine-Impregnated Mesoporous SBA-15 Sorbents: Experimental and Kinetics Study. *Industrial & Engineering Chemistry Research* **2013,** *52* (19), 6480-6491.

27.   Chen, S. S.; Lucier, B. E. G.; Boyle, P. D.; Huang, Y. N., Understanding The Fascinating Origins of CO_2 Adsorption and Dynamics in MOFs. *Chemistry of Materials* **2016,** *28* (16), 5829-5846.

28.   Zhang, J. P.; Liao, P. Q.; Zhou, H. L.; Lin, R. B.; Chen, X. M., Single-crystal X-ray diffraction studies on structural transformations of porous coordination polymers. *Chemical Society Reviews* **2014,** *43* (16), 5789-5814.

29.   Takamizawa, S.; Nakata, E.; Saito, T.; Kojima, K., Structural determination of physisorbed sites for CO2 and Ar gases inside an organometallic framework. *Crystengcomm* **2003,** *5*, 411-413.

30.   Takamizawa, S.; Takasaki, Y.; Miyake, R., Host-guest transformational correlations for a gas inclusion co-crystal on changing gas pressure and temperature. *Chemical Communications* **2009,** (43), 6625-6627.

31.   Zhang, Y.; Lucier, B. E. G.; Huang, Y. N., Deducing CO_2 motion, adsorption locations and binding strengths in a flexible metal-organic framework without open metal sites. *Physical Chemistry Chemical Physics* **2016,** *18* (12), 8327-8341.

32.   Wang, W. D.; Lucier, B. E. G.; Terskikh, V. V.; Wang, W.; Huang, Y. N., Wobbling and Hopping: Studying Dynamics of CO_2 Adsorbed in Metal-Organic Frameworks via O-17 Solid-State NMR. *Journal of Physical Chemistry Letters* **2014,** *5* (19), 3360-3365.

33.   Lucier, B. E. G.; Chan, H.; Zhang, Y.; Huang, Y. N., Multiple Modes of Motion: Realizing the Dynamics of CO Adsorbed in M-MOF-74 (M = Mg, Zn) by Using Solid-State NMR Spectroscopy. *European Journal of Inorganic Chemistry* **2016,** (13-14), 2017-2024.

34.   Lucier, B. E. G.; Zhang, Y.; Lee, K. J.; Lu, Y. J.; Huang, Y. N., Grasping hydrogen adsorption and dynamics in metal-organic frameworks using H-2 solid-state NMR. *Chemical Communications* **2016,** *52* (48), 7541-7544.

35.   Mason, J. A.; McDonald, T. M.; Bae, T. H.; Bachman, J. E.; Sumida, K.; Dutton, J. J.; Kaye, S. S.; Long, J. R., Application of a High-Throughput Analyzer in Evaluating Solid Adsorbents for Post-Combustion Carbon Capture via Multicomponent Adsorption of CO_2, N_2, and H_2O. *Journal of the American Chemical Society* **2015,** *137* (14), 4787-4803.

36.   Bakhmutov, V. I., Strategies for Solid-State NMR Studies of Materials: From Diamagnetic to Paramagnetic Porous Solids. *Chemical Reviews* **2011,** *111* (2), 530-562.

37.   Bruker-AXS *SAINT*, version 2013.8; Bruker-AXS Madison, WI 53711, USA, 2013.

38.   Bruker-AXS *SADABS*, version 2012.1; Bruker-AXS: Madison, WI 53711, USA, 2012.

39.   Sheldrick, G. M., SHELXT - Integrated space-group and crystal-structure determination. *Acta Crystallographica a-Foundation and Advances* **2015,** *71*, 3-8.

40.   Sheldrick, G. M., Crystal structure refinement with SHELXL. *Acta Crystallographica Section C-Structural Chemistry* **2015,** *71*, 3-8.

41.   Gabe, E. J.; Lepage, Y.; Charland, J. P.; Lee, F. L.; White, P. S., NRCVAX - AN INTERACTIVE PROGRAM SYSTEM FOR STRUCTURE-ANALYSIS. *Journal of Applied Crystallography* **1989,** *22*, 384-387.

42.   Aliev, A. E.; Harris, K. D. M.; Apperley, D. C., HIGH-RESOLUTION SOLID-STATE C-13 AND SI-29 NMR INVESTIGATIONS OF THE DYNAMIC PROPERTIES OF TETRAKIS(TRIMETHYLSILYL)SILANE. *Journal of the Chemical Society-Chemical Communications* **1993,** (3), 251-253.

43.   Ji, S. X.; Hoye, T. R.; Macosko, C. W., Primary amine (-NH2) quantification in polymers: functionality by F-19 NMR spectroscopy. *Macromolecules* **2005,** *38* (11), 4679-4686.

44.   Hayashi, S.; Hayamizu, K., CHEMICAL-SHIFT STANDARDS IN HIGH-RESOLUTION SOLID-STATE NMR (1) C-13, SI-29 AND H-1 NUCLEI. *Bulletin of the Chemical Society of Japan* **1991,** *64* (2), 685-687.

45.   Eichele, R. E. W. K. *WSolids1*, University of Tübingen: Germany, 2001.

46.   Vold, R. L.; Hoatson, G. L., Effects of jump dynamics on solid state nuclear magnetic resonance line shapes and spin relaxation times. *Journal of Magnetic Resonance* **2009,** *198* (1), 57-72.

47.   Beeler, A. J.; Orendt, A. M.; Grant, D. M.; Cutts, P. W.; Michl, J.; Zilm, K. W.; Downing, J. W.; Facelli, J. C.; Schindler, M. S.; Kutzelnigg, W., LOW-TEMPERATURE C-13 MAGNETIC-RESONANCE IN SOLIDS .3. LINEAR AND PSEUDOLINEAR MOLECULES. *Journal of the American Chemical Society* **1984,** *106* (25), 7672-7676.

48.   Clark, S. J.; Segall, M. D.; Pickard, C. J.; Hasnip, P. J.; Probert, M. J.; Refson, K.; Payne, M. C., First principles methods using CASTEP. *Zeitschrift Fur Kristallographie* **2005,** *220* (5-6), 567-570.

49.   Profeta, M.; Mauri, F.; Pickard, C. J., Accurate first principles prediction of O-17 NMR parameters in SiO_2: Assignment of the zeolite ferrierite spectrum. *Journal of the American Chemical Society* **2003,** *125* (2), 541-548.

50.   Kong, X. Q.; Scott, E.; Ding, W.; Mason, J. A.; Long, J. R.; Reimer, J. A., CO2 Dynamics in a Metal-Organic Framework with Open Metal Sites. *Journal of the American Chemical Society* **2012,** *134* (35), 14341-14344.

51.   Lu, Y. J.; Lucier, B. E. G.; Zhang, Y.; Ren, P. J.; Zheng, A. M.; Huang, Y. N., Sizable dynamics in small pores: CO_2 location and motion in the alpha-Mg formate metal-organic framework. *Physical Chemistry Chemical Physics* **2017,** *19* (8), 6130-6141.

52.   Baek, S. B.; Lee, H. C., C-13 NMR Study of CO_2 Adsorbed in Highly Flexible Porous Metal-Organic Frameworks. *Bulletin of the Korean Chemical Society* **2016,** *37* (4), 588-591.

53.   Masala, A.; Grifasi, F.; Atzori, C.; Vitillo, J. G.; Mino, L.; Bonino, F.; Chierotti, M. R.; Bordiga, S., CO_2 Adsorption Sites in UTSA-16: Multitechnique Approach. *Journal of Physical Chemistry C* **2016,** *120* (22), 12068-12074.

54.   Bovey, F. A., *NMR Data Tables for Organic Compounds*. Interscience Publishers: New York, USA, 1967.

55.   Duer, M. J., *Solid-State NMR Spectroscopy*. Blackwell Publishing Ltd: Oxford, United Kingdom, 2004; p 349.

56.   Gullion, T., Introduction to rotational-echo, double-resonance NMR. *Concepts in Magnetic Resonance* **1998,** *10* (5), 277-289.

57.   Pyykko, P., Year-2008 nuclear quadrupole moments. *Molecular Physics* **2008,** *106* (16-18), 1965-1974.

58.   Huang, Y. N.; Sutrisno, A., Recent Advances in Solid-State Zn-67 NMR Studies: From Nanoparticles to Biological Systems. *Annual Reports on Nmr Spectroscopy, Vol 81* **2014,** *81*, 1-46.

59.   Hoffner, F. M.; Delmotte, L.; Kessler, H., A F-19/SI-29 CP MAS NMR-STUDY OF MICROPOROUS SOLIDS SYNTHESIZED IN FLUORIDE MEDIUM. *Zeolites* **1993,** *13* (1), 60-63.

60.   Finney, W. F.; Wilson, E.; Callender, A.; Morris, M. D.; Beck, L. W., Reexamination of hexafluorosilicate hydrolysis by F-19 NMR and pH measurement. *Environmental Science & Technology* **2006,** *40* (8), 2572-2577.

61.   Pretsch, E.; Clerc, T.; Seibl, J.; Simon, W., Tables of Spectral Data for Structure Determination of Organic Compounds. 2 ed.; Springer-Verlag: Berlin, Heidelberg, 1989; p 416.

62.   Fulmer, G. R.; Miller, A. J. M.; Sherden, N. H.; Gottlieb, H. E.; Nudelman, A.; Stoltz, B. M.; Bercaw, J. E.; Goldberg, K. I., NMR Chemical Shifts of Trace Impurities: Common Laboratory Solvents, Organics, and Gases in Deuterated Solvents Relevant to the Organometallic Chemist. *Organometallics* **2010,** *29* (9), 2176-2179.

2.6   Appendix

Table S2.1: Acquisition parameters for VT static ^{13}C SSNMR of $^{13}CO_2$ loaded SIFSIX-3-Zn are shown below.

Sample	Temperature (K)	Acquisitions	Decoupled Nuclei	Pulse Delay (s)	90° Pulse Width (μs)
SIFSIX-3-Zn, CO$_2$ Loaded	393 K	749	^{1}H	5	3.00
	373 K	838	^{1}H	5	3.00
	353 K	706	^{1}H	5	3.00
	333 K	1110	^{1}H	5	3.00
	313 K	762	^{1}H	5	3.00
	293 K	4083	^{1}H	15	3.00
	273 K	623	^{1}H	5	3.00
	253 K	626	^{1}H	5	3.00
	233 K	782	^{1}H	5	3.00
	213 K	653	^{1}H	5	3.00
	193 K	671	^{1}H	5	3.00
	173 K	603	^{1}H	5	3.00
	153 K	622	^{1}H	5	3.00
	293 K	4665	^{19}F	10	2.75
	293 K	1681	None	10	2.75
	293 K	1460	^{1}H and ^{19}F	10	2.75

Table S2.2: Acquisition parameters for static CP SSNMR of $^{13}CO_2$ loaded SIFSIX-3-Zn are shown below.

Temperature	CP	Acquisitions	Pulse Delay (s)	90° Pulse Width (μs)
293 K	^{1}H-^{13}C	7200	2	6.90
135 K	^{1}H-^{13}C	1800	2	13.5
293 K	^{19}F-^{13}C	1000	2	9.50

Table S2.3: Acquisition parameters for MAS ^{13}C direct-excitation and CP SSNMR of $^{13}CO_2$ loaded SIFSIX-3-Zn are shown below.

Spin Rate (Hz)	CP	Acquisitions	Pulse Delay (s)	90° Pulse Width (µs)
15 000	None	2950	20	3.70
2010	None	2000	3	3.70
15 000	^{1}H-^{13}C	1400	2	4.50
15 000	^{19}F-^{13}C	1000	2	5.20

Table S2.4: Acquisition parameters for MAS direct-excitation and CP SSNMR of SIFSIX-3-Zn using additional nuclei are shown below.

Spin Rate (Hz)	Nuclei	Acquisitions	Pulse Delay (s)	90° Pulse Width (µs)
15 000	^{1}H	60	5	8.75
15 000	^{19}F	30	10	6.25
15 000	^{1}H-^{29}Si	4000	6.6	1.00

Table S2.5: The observed ^{13}C chemical shift parameters of CO_2 adsorbed within room temperature SIFSIX-3-Zn, when using different decoupling fields, are listed below.These parameters were obtained from analytical simulations of static ^{13}C SSNMR spectra using WSolids.[45]

Decoupling	δ_{iso} (ppm)	Ω (ppm)	κ
^{1}H	124 (1)	306 (2)	0.98 (2)
^{19}F	123 (1)	306 (3)	0.97 (3)
None	122 (1)	308 (2)	0.96 (2)
^{1}H and ^{19}F	123 (1)	308 (2)	0.95 (2)
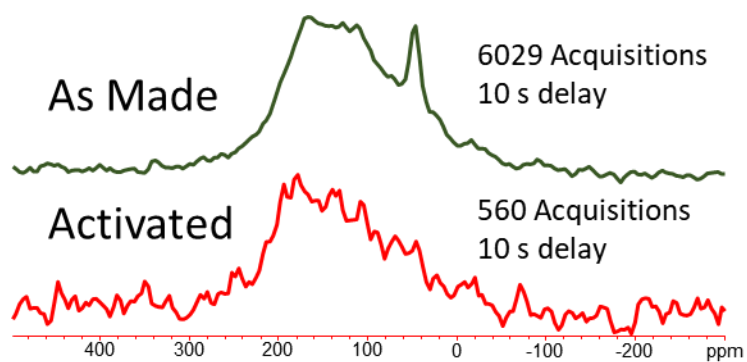
Figure S2.1: The experimental ^{13}C SSNMR spectra of as made and activated SIFSIX-3-Zn. The number of scans and recycle delays used are listed on the experimental spectra.
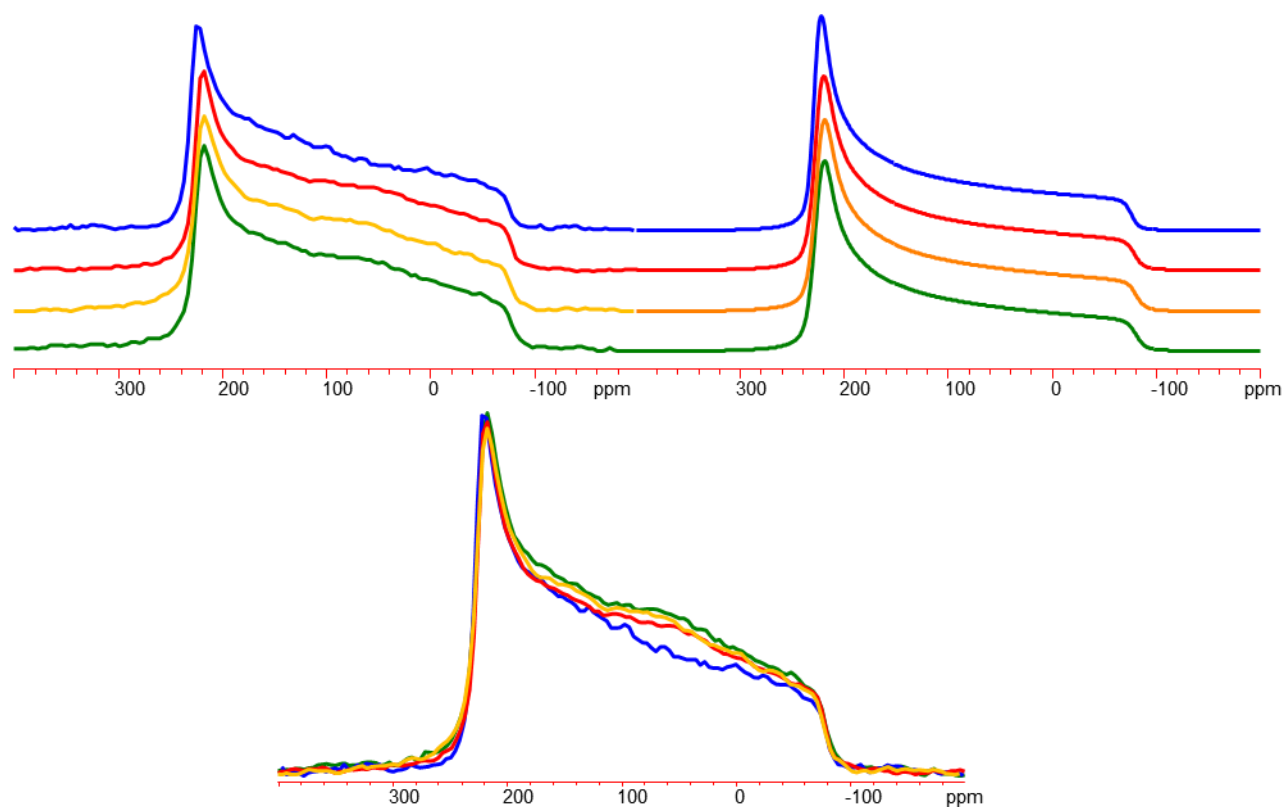
Figure S2.2: On top, the experimental (left) and simulated (right) ^{13}C NMR spectra of $^{13}CO_2$ loaded SIFSIX-3-Zn with different combinations of decoupling fields are displayed. ^{1}H decoupling is shown in blue, ^{19}F decoupling is shown in red, non-decoupled is shown in orange, double decoupling is shown in green. On the bottom, the overlapping experimental spectra are shown.
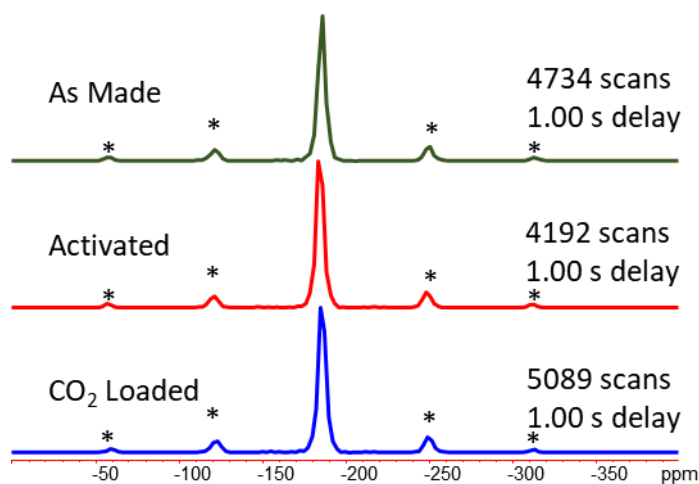
Figure S2.3: The experimental ^1H-^{29}Si CP spectra of as made, activated and CO_2 loaded SIFSIX-3-Zn. The scan numbers and recycle delays are listed on the experimental spectra. All the spectra were collected while spinning at 5 kHz. Spinning sidebands are denoted by asterisks.
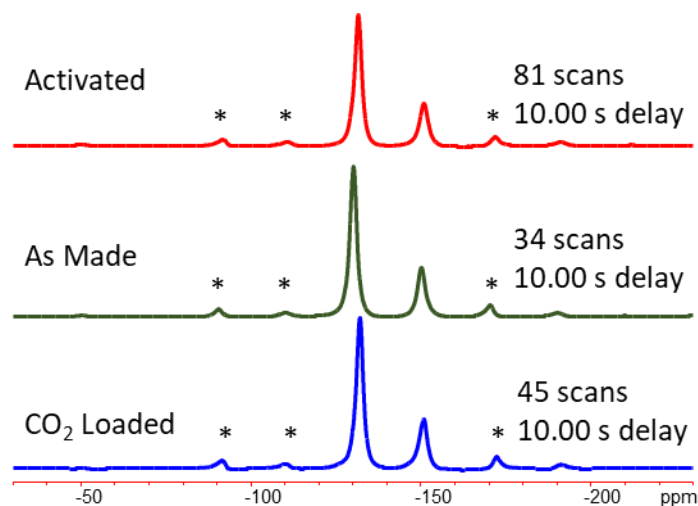
Figure S2.4: The experimental ^{19}F spectra of as made, activated and CO_2 loaded SIFSIX-3-Zn are depicted above. The scan numbers and recycle delays are listed on the experimental spectra. All the spectra were collected while spinning at 15 kHz. Asterisks denote notable spinning sidebands.
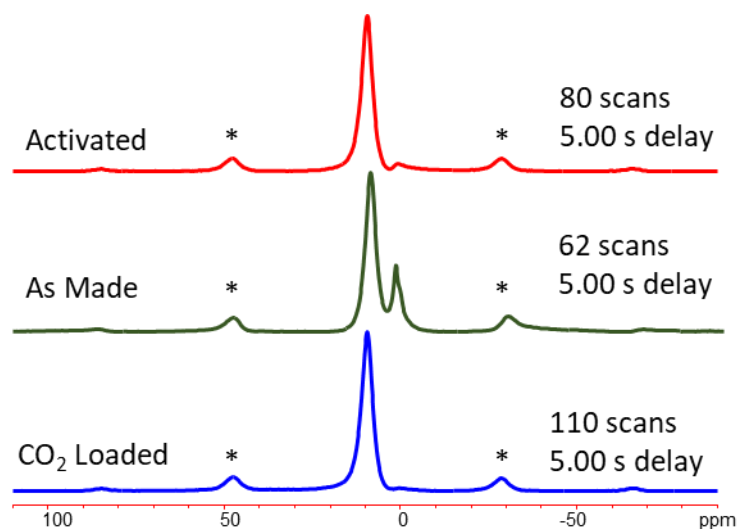
Figure S2.5: The experimental ^1H spectra of as made, activated and CO_2 loaded SIFSIX-3-Zn. The scan numbers and recycle delays are listed on the experimental spectra. All the spectra were collected while spinning at 15 kHz. Spinning sidebands are denoted by asterisks.

2.6.1 SSNMR using additional nuclei in SIFSIX-3-Zn.

MAS SSNMR experiments were conducted using ^1H, ^{19}F and ^{29}Si nuclei. Experiments were conducted on the as made, activated, and CO_2 loaded phases of SIFSIX-3-Zn.

The collected ^1H-^{29}Si CP spectra can be seen in Figure S2.3. The spectra are characterized by a single resonance at approximately 185 ppm. This chemical shift value is comparable to those obtained in previous NMR studies of hexafluorosilicates.[59]

The collected ^{19}F spectra can be seen in Figure S2.4. The spectra feature two distinct resonances, one at -131 ppm and a less intense resonance at -150 ppm. The more intense resonance is assigned to the four equatorial fluorine atoms within the SiF_6^{2-} linker in the framework, while the less intense resonance is assigned to the two axial fluorine atoms in the SiF_6^{2-} linker. The fluorine atom in SiF_6^{2-} has a previously reported CS of -130.5 ppm,[60] while the CS of the fluorine

atom in NaSiF$_6$ is reported as -152 ppm.[59] This suggests consistency between experimental and literature values for these chemical shifts.

The ^{1}H spectra are depicted in Figure S2.5, and characterized by a single resonance at 9.4 ppm, corresponding the proton on the pyrazine linker. The proton in the pyrazine molecule has a reported CS of 8.63 ppm.[61] The as made framework also contains two notable resonances at 2.2(2) ppm and 1.1(2) ppm. These resonances are due to the protons in the guest methanol, which have reported CS values of 3.49 ppm for the methyl protons and 1.09 ppm for the hydroxyl proton.[62] Given the 1.3 ppm difference between experimental and literature CS values for the methyl protons, it seems likely that these protons are interacting strongly with the SIFSIX-3-Zn framework.

The chemical shift values of the silicon, fluorine and hydrogen atoms does not appear to be affected by the presence or absence of methanol or CO_2 molecules within the framework pores, suggesting that there is little change in their chemical environment due to interactions between these nuclei and guest molecules. The number of unique nuclei identified is consistent with the known structure of SIFSIX-3-Zn in all cases.

Chapter 3 : Studying Carbon Dioxide Adsorption within the Amine Functionalized ZnAtzOx Framework

3.1   Introduction

Due to the known impacts of carbon dioxide on the greenhouse effect, and the consequences thereof,[1] there has been much research into the field of carbon capture from flue-gas and air.[2, 3] Chemisorbent alkanolamines currently remain the preferred choice for CO_2 capture applications over physisorbent materials.[4, 5] However, solid physisorbent MOF materials are an attractive alternative due to the lower energy requirements and lack of equipment corrosion.[6] Amine-functionalized physisorbents, such as the UiO-66-NH_2 metal-organic framework (MOF),[7] are known to exhibit increased adsorption enthalpy, uptake, and selectivity for carbon dioxide versus their nonfunctionalized counterparts.[8, 9] The addition of highly polar ligands such as NH_2 enhances the affinity of the MOF for polarizable gases such as CO_2, and enhances selectivity against N_2 molecules.[10-13] Given this knowledge, the study of amine-functionalized MOFs for CO_2 adsorption is a promising path for the improvement of solid physisorbents for CO_2 adsorption applications.

One such material is a series of porous zinc-aminotriazolato-oxalate MOFs referred to as ZnAtzOx, depicted in Figures 3.1, 3.2 and 3.3.[14] This structure is made up of zinc-3-amino-1,2,4-triazolate layers that are pillared into three dimensions by oxalate units, creating 3.5×4.0 Å channels along the *a*-axis, which are crosslinked by smaller channels running along the *b* and *c*-axes. The ZnAtzOx framework exhibits high selectivity for CO_2 adsorption against other gases such as H_2 and N_2 due to its narrow ultramicropores and amine functionality.[14, 15] The effects of ultramicropores of less than 7 Å across on CO_2 selectivity is well demonstrated in structures such as the SIFSIX-3 materials, and discussed in more detail in the previous chapter.[16] Crystallographic

and computational studies of the original ZnAtzOx phase found that each pore contains two partially occupied CO_2 binding sites; one is located near the amine group while the other is found closer to the oxalate group.[17] The two binding sites lead to a maximum observed occupancy of approximately 1.3 CO_2 molecules per unit cell. A similar series has also been synthesized by replacing the oxalate linkers in ZnAtzOx with 1,4-benzenedicarboxylate ligands to produce the CALF series of MOFs, though this series was not found to be viable for CO_2 capture applications.[18]
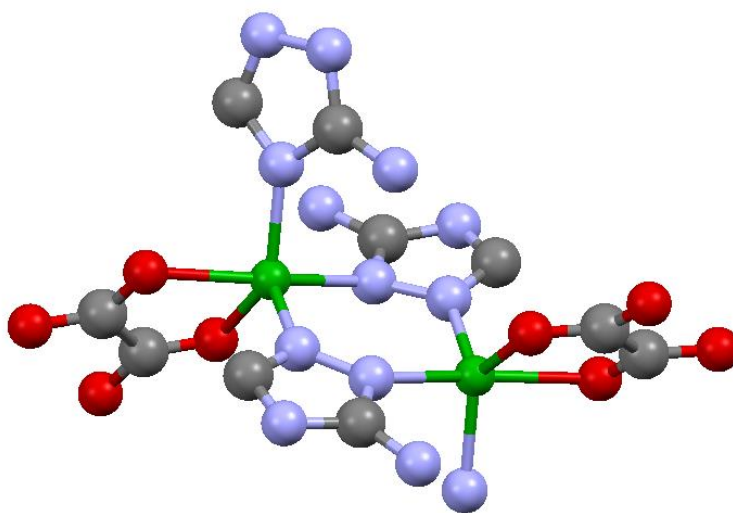
Figure 3.1: Zn_2Atz_2 nodes in the $ZnAtzOx(H_2O)$ framework are depicted above. Each five-coordinate zinc centre is coordinated to an oxalate linker via a bidentate interaction. Each zinc is in turn coordinated to three separate aminotriazolato linkers. This forms two-dimensional zinc-aminotriazolato layers pillared into three dimensions by oxalate linkers. For all figures in this chapter, the atom colours are green for Zn, grey for C, red for O, and blue for N.

ZnAtzOx was originally synthesized in 2009 solvothermally using methanol.[14] However, in 2016 it was detailed how the choice of solvent dramatically affected the CO_2 uptake of the structure.[19] A series of topologically related ZnAtzOx frameworks were synthesized solvothermally using water (Figure 3.3), ethanol (Figure 3.4), propanol and butanol. The CO_2

uptakes of these different phases varied dramatically; the water synthesized structure, which will be referred to here as ZnAtzOx(H$_2$O), had an uptake of over 5 mmol g^{-1} of CO$_2$ at a pressure of 800 mmHg, while the original phase adsorbed less than 4 mmol g^{-1} of CO$_2$ at the same pressure. The propanol synthesized structure, in contrast, appeared to be non-porous.
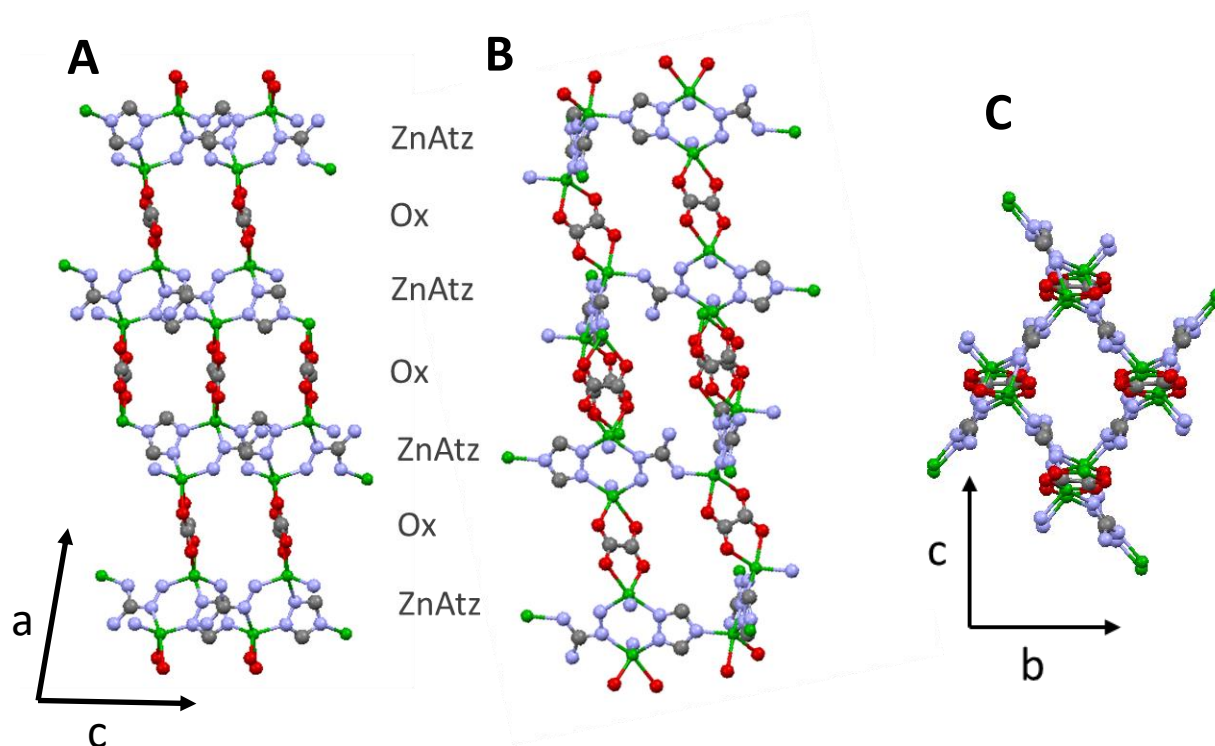
Figure 3.2: The pores of the ZnAtzOx(H$_2$O) framework are illustrated from a perspective that lies along the crystallographic b-axis (A), [0 1 1] axis (B), and a-axis (C). The alternating zinc-aminotriazolato and oxalate layers can be seen in the left two views of the structure. The exact shape of the pore differs depending on the phase of the MOF, where the synthesis medium can be methanol, water, ethanol or propanol.

The CO$_2$ uptake vs. partial pressure curve for ZnAtzOx(H$_2$O) features a sharp increase in CO$_2$ uptake at a *P/P$_0$* level of 0.2 at 273 K. This indicates that the anomalously high uptake of this phase is due to a CO$_2$ assisted gate-opening mechanism, where the guest molecules induce a structural modification that creates additional adsorption sites within the framework. The effects

of this gate-opening are significant, with the maximum occupancy of CO_2 molecules per unit cell increasing from 1.3 to 2.25.
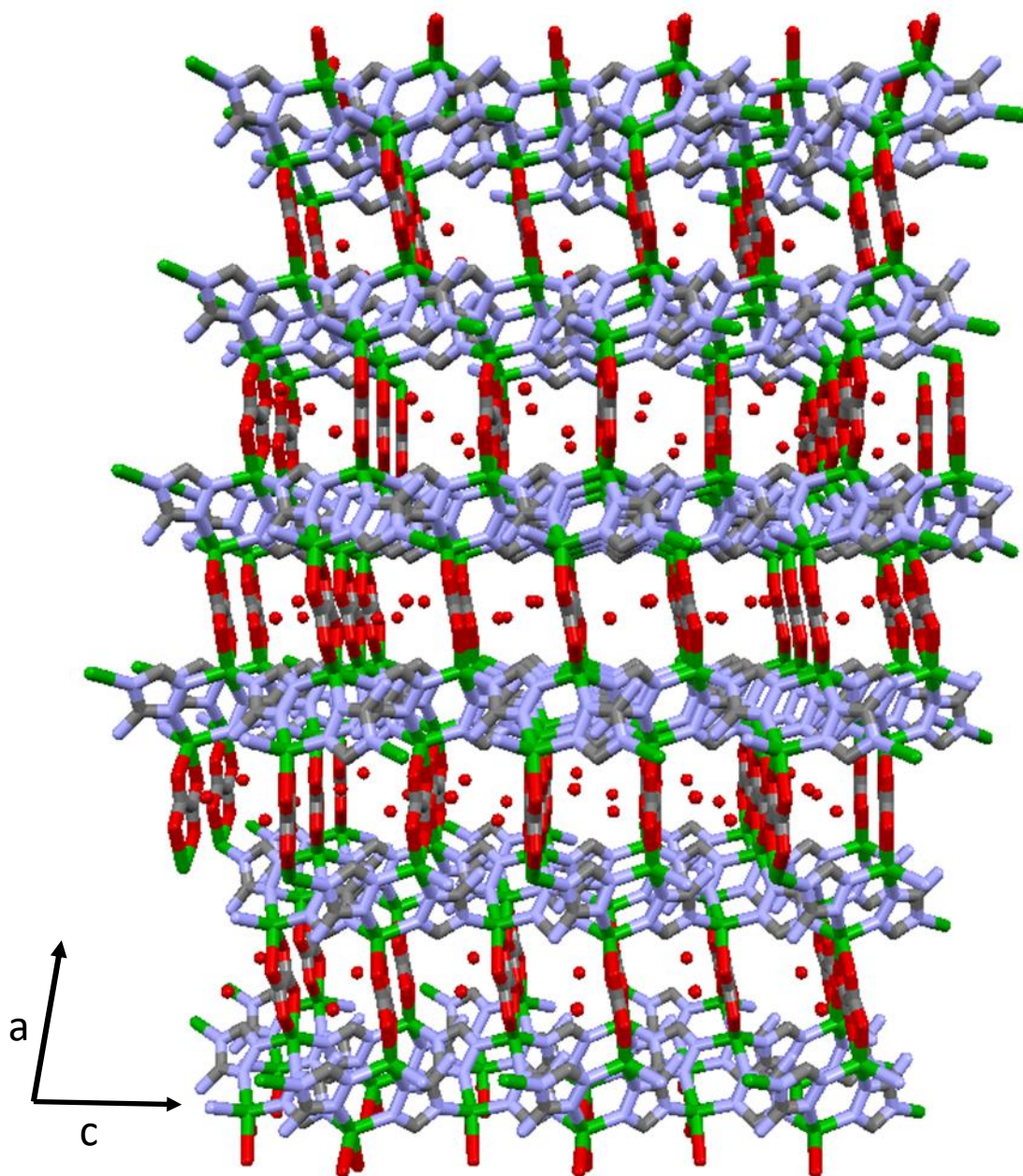
Figure 3.3: The ZnAtzOx(H₂O) framework is illustrated from a perspective that lies along the crystallographic b-axis. Water molecules occupy the pore and their O nuclei are depicted in the figure above. The structure contains two similar H₂O adsorption sites 3.0 to 4.0 Å from the oxalate and amino-triazolate linkers.
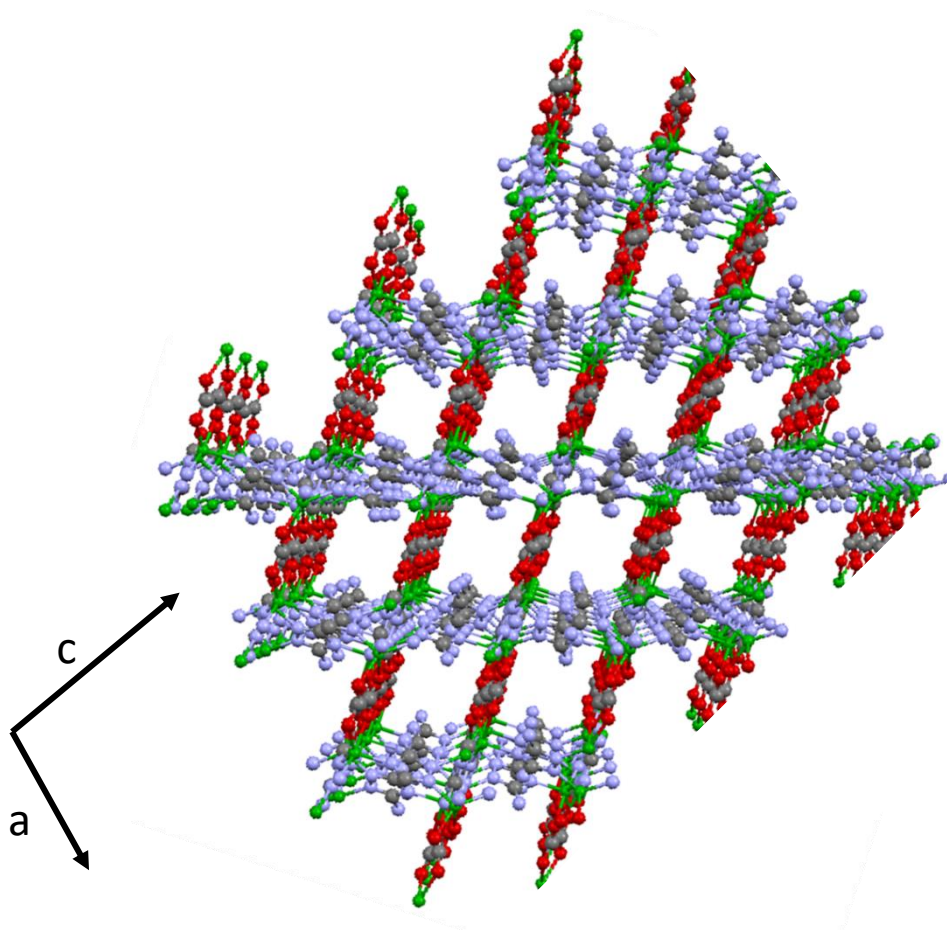
Figure 3.4: The ZnAtzOx(EtOH) framework is illustrated from a perspective that lies along the crystallographic b-axis. Ethanol molecules occupying the pore are not shown.

The cause of this gate-opening is thought to be the asymmetrical bonding of the oxalate linkers. Within $ZnAtzOx(H_2O)$, the bonds between the Zn^{2+} centre and the oxygen atoms of the oxalate linker are more symmetrically arranged than in other ZnAtzOx phases. This symmetric arrangement of relatively weak bonds facilitates a swivelling motion of the oxalate pillars. The zinc oxalate units are illustrated in Figure 3.5. This is supported by PXRD experiments showing that no major structural change occurs within the framework after gate-opening. This indicates that

subtle molecular motions such as linker rotation must have been the cause of the observed gate-opening.[19]
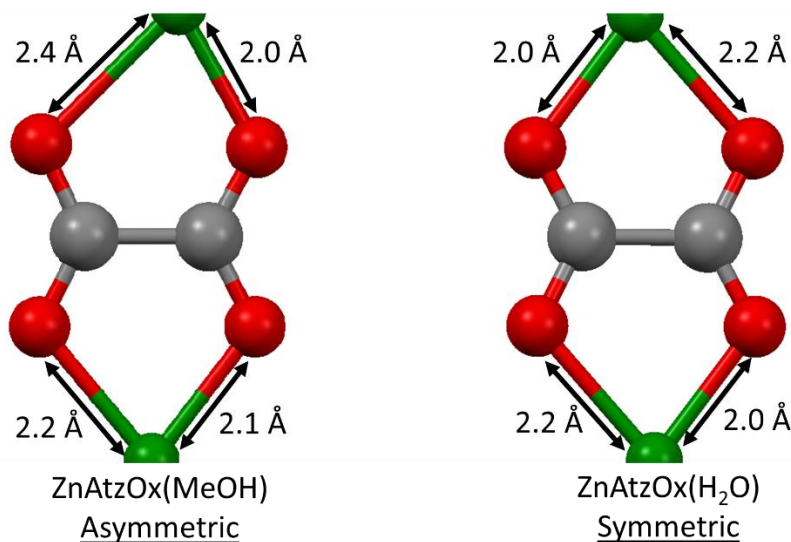
Figure 3.5: A comparison of the zinc-oxalate units in ZnAtzOx(MeOH) and ZnAtzOx(H₂O) is shown. It has been argued that the symmetrical Zn – O bonds within ZnAtzOx(H₂O) allow for gate-opening to occur, as the oxalate units are able to more easily swivel.

Comparing the room temperature adsorption isotherms can help gauge the selectivity for CO_2 adsorption over N_2 in ZnAtzOx(H_2O).[19] Selectivity was assessed by comparing the ratio of CO_2 and N_2 adsorption in adsorption isotherms, divided by the ratio of CO_2 and N_2 partial pressures. The selectivity determined by this method, at low partial pressures of 0.15 bar CO_2 and 0.75 bar N_2, was found to exceed the selectivity observed in other highly selective frameworks such as SIFSIX-3-Zn[16] and SIFSIX-3-Cu;[20] the ZnAtzOx family of structures may be a viable solid CO_2 capture material at low CO_2 pressures, and therefore it is of interest to understand the behaviour and interactions of CO_2 within the material.

The factors behind the carbon dioxide selectivity within ZnAtzOx(H_2O) can be investigated using solid-state nuclear magnetic resonance (SSNMR), which is a key tool for

studying interactions between guest molecules and host frameworks. It is also possible to determine whether the phase of ZnAtzOx has a noticeable effect on the types of CO_2 motion present within the framework. Much like the previously discussed SIFISIX-3-Zn, ZnAtzOx(H_2O) is an ultramicroporous framework, although its structure is very different from that of the SIFSIX frameworks. The strong selectivity of certain ultramicroporous frameworks for CO_2 adsorption warrants a thorough investigation of the interactions between such frameworks and their guests.

3.2   Experimental

3.2.1   Synthesis of ZnAtzOx

ZnAtzOx phases were synthesized solvothermally using methods described in the literature.[19] A typical synthesis of ZnAtzOx(H_2O) or ZnAtzOx(EtOH) is as follows: oxalic acid (0.09 g, 1 mmol, Sigma-Aldrich, 98%), 3-amino-1,2,4-triazole (0.42 g, 5 mmol, Sigma-Aldrich, ≥95%) and zinc carbonate basic (0.11g, 1 mmol, Alfa Aesar, 97%) were added to either (i) a 3 mL butanol and 3 mL water solvent mixture or (ii) a 5 mL ethanol and 1 mL water solvent mixture in a Teflon-lined stainless steel autoclave. The solution was stirred for 30 min at room temperature, and then heated at 180 °C for two days. Upon cooling, a colourless crystalline product was collected using vacuum filtration, washed with methanol and water, and dried at 90 °C in air for three hours.

3.2.2   Powder X-ray diffraction

The identities and purities of the material were confirmed using powder X-ray diffraction (PXRD). The PXRD patterns were recorded on an Inel CPS powder diffractometer operating with Cu Kα radiation. Experimental and simulated PXRD patterns are depicted in Figure 3.6. The experimental PXRD patterns are consistent with the calculated patterns from known crystal

structures and with previously determined experimental PXRD patterns of the materials, and suggest phase purity of the samples.[19] There are slight discrepancies in reflection intensities when contrasting the experimental and calculated ZnAtzOx(EtOH) patterns, likely due to preferred orientation effects. Similar discrepancies in reflection intensities were observed in the previously reported PXRD pattern of the material,[19] therefore the identity of the material can still be confirmed.
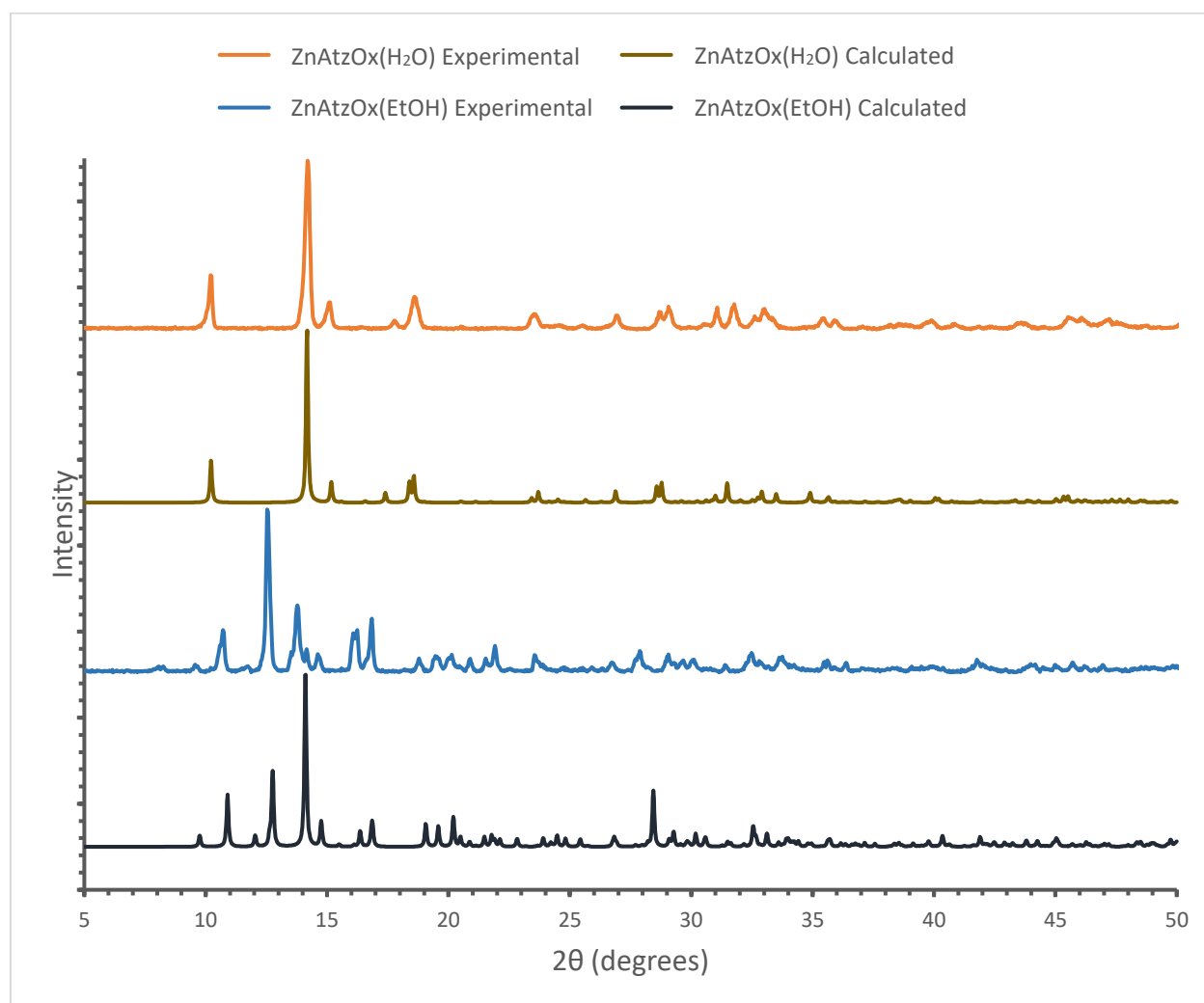
Figure 3.6: The experimental and calculated ZnAtzOx PXRD patterns are depicted above.

3.2.3 Sample activation and gas loading

The activation process removes solvent molecules from the framework pores. A Schlenk line was used for activation. Samples were placed into the bottom of an L-shaped glass tube, and a thin layer of glass wool was used to secure the sample in place. The ZnAtzOx samples were activated under dynamic vacuum at 150 ± 10 °C for 12 hours. CO_2 gas was released into the line, with a measured total volume of 82.7 mL, as the CO_2 pressure was monitored. The sample was then loaded with a known quantity of CO_2 while the glass tube was immersed in liquid nitrogen. The loaded sample within the glass tube was then flame sealed off from the Schlenk line to trap guest molecules in a closed space with the sample prior to SSNMR experiments.

A 0.25 molar ratio of CO_2 to Zn^{2+} was used when loading samples with carbon dioxide. ^{13}C labelled CO_2 (Sigma-Aldrich, 99 atom % ^{13}C, <3 atom % ^{18}O) was used to load samples for ^{13}C SSNMR experiments.

3.2.4 SSNMR experiments

^{13}C and ^{1}H SSNMR experiments were performed at the University of Western Ontario in London, Ontario, using a Varian Infinity Plus SSNMR spectrometer equipped with an Oxford 9.4 T wide-bore magnet. Static ^{13}C experiments were conducted with a 5 mm HX Varian/Chemagnetics probe, while ^{13}C and ^{1}H magic-angle spinning (MAS) experiments were conducted with a 4 mm HXY Varian/Chemagnetics probe.

^{13}C spectra were referenced to tetramethylsilane (TMS) using the methylene carbon in ethanol as a secondary reference, which has a chemical shift (CS) of 58.05 ppm.[21] All direct-excitation ^{13}C SSNMR experiments were performed using the DEPTH-echo pulse sequence to minimize spectral distortions and interference from the background probe signal.[22] The Hartmann-Hahn match in ^{1}H-^{13}C cross polarization (CP) experiments was calibrated using solid adamantane

(Sigma-Aldrich, 98+%). ^{1}H spectra were referenced to TMS using the CH$_2$ sites in solid adamantane (Sigma-Aldrich, 98+%) as a secondary reference with a CS of 1.85 ppm.[23, 24] Direct-excitation ^{1}H experiments were performed using a one pulse sequence. Additional parameters for individual spectral acquisitions are described in Tables S3.1, S3.2, S3.3 and S3.4. All experiments were performed using a 30 kHz ^{1}H decoupling field.

^{67}Zn experiments were conducted at 21.1 T on a Bruker II Avance spectrometer at the National Ultrahigh-field NMR facility for Solids in Ottawa, Canada, with a home-built 7 mm HX probe, using a solid-echo (*i.e.*, 90 °- 90 ° echo) pulse sequence. The spectra were referenced to 1.0 M aqueous Zn(NO$_3$)$_2$, at 0 ppm.

Frequency switched Lee-Goldburg (FSLG) Heteronuclear correlation (HETCOR) experiments were conducted at 21.1 T using the same Bruker II Avance spectrometer described above. Experiments were performed using a 4 mm HCN Bruker probe in high speed ZrO$_2$ Bruker rotors, spinning at 18 kHz. 32 points were used across the indirect (^{1}H) dimension, with 512 scans for each point. A short contact time of 500 μs was used to prevent unwanted long-range correlations. Spectra were referenced to TMS using solid adamantane as a secondary reference with a chemical shift of 1.85 ppm.[23] The Hartman-Hahn match in ^{1}H-^{13}C CP experiments was calibrated using glycine.

3.2.5 Spectral simulations

The WSolids[25] computer software was used to analytically simulate all static ^{13}C SSNMR spectra and obtain apparent powder pattern parameters. The ^{13}C patterns are broadened and dominated by the CS anisotropy (CSA), while the ^{67}Zn patterns are dominated by the quadrupolar interaction (QI). WSolids calculated the powder pattern of a static powder sample showing effects of the CSA or QI. ^{13}C SSNMR patterns were calculated through inputting the orthogonal

components of the CS tensor (δ_{11}, δ_{22} and δ_{33}). ^{67}Zn SSNMR patterns were calculated through inputting the electric field gradient (EFG) parameters (C_Q and η_Q). By comparing the known experimental powder patterns to a calculated pattern, the experimental powder pattern parameters for ^{13}C (δ_{iso}, Ω and κ) and ^{67}Zn (C_Q and η_Q) can be determined. The errors in pattern parameters were estimated by bidirectional variation of the parameters from the best-fit value.

The EXPRESS[26] computer software was used to simulate the effects of motion on ^{13}C SSNMR powder patterns. EXPRESS describes motion in terms of discrete (Markovian) jumps at specified rates between sites. A motional model can then be described by the number, orientation, and populations of sites, as well as the nature of the connections and rates of jumps. The motion results in a predictable averaging of CS tensor components. Given the known powder pattern parameters of solid CO_2 (δ_{iso} = 126 ppm, Ω = 335 ppm, and κ = 1),[27] and assuming a linear geometry for the CO_2 molecule, powder patterns produced by specific types and rates of motion were calculated across 4096 powder increments using the ZCW powder averaging procedure and compared to the experimental powder pattern.

3.2.6 Theoretical calculations

Gauge-including projector augmented wave (GIPAW) quantum chemical calculations were performed by Dr. Victor Terskikh with the NMR module of the CASTEP software package version 4.4 within Materials Studio.[28, 29] The unit cell parameters and atomic coordinates for ZnAtzOx(H_2O) were taken from the reported crystal structure at 173 K.[19] Geometry optimization was performed prior to calculations. The activated structure was generated by removing H_2O molecules from the reported as made ZnAtzOx(H_2O) structure, and calculations were performed with and without geometry optimization on the activated structure. Calculations were performed with a plane-wave cut-off energy of 300 eV and on-the-fly generated ultrasoft pseudopotentials.

3.3   Results and Discussion

3.3.1   Static variable temperature ^{13}C SSNMR of $^{13}CO_2$ loaded ZnAtzOx(H$_2$O)

The motional behaviour of the CO_2 molecules in the ZnAtzOx(H$_2$O) pores was assessed using static ^{13}C SSNMR experiments. These experiments conducted on ZnAtzOx(H$_2$O) revealed a similar lack of CO_2 mobility as that within SIFSIX-3-Zn. Variable temperature (VT) ^{13}C SSNMR experiments were conducted on $^{13}CO_2$ loaded ZnAtzOx(H$_2$O). ZnAtzOx synthesized in H$_2$O was previously found to have the highest CO_2 uptake of all the ZnAtzOx framework phases studied, being able to hold 2.25 molecules of CO_2 per functional unit.[19] The experimental and simulated SSNMR powder patterns can be seen in Figure 3.7, and the CS parameters of the simulated patterns can be seen in Table 3.1. Only a single crystallographically unique CO_2 adsorption site can be identified from the NMR results.

The Ω of the powder pattern ranges from 256(4) ppm at 393 K, to 311(3) ppm at 153 K. The κ value ranges from 0.69(3) to 0.94(2) over the same temperature range. The adsorbed $^{13}CO_2$ in ZnAtzOx(H$_2$O) is relatively immobile, though not to the extent observed in SIFSIX-3-Zn, where Ω and κ values were 315 ppm and 1.00 respectively at 153 K. Though ZnAtzOx(H$_2$O) displays a greater degree of temperature dependence for CO_2 motions than what was observed in SIFSIX-3-Zn, it is nevertheless not so much as what has been observed in previously studied MOFs.[22, 30-32] The temperature dependence of the κ parameter is a notable difference from the CO_2 behaviour in SIFSIX-3-Zn, where it was near 1.0 even at high temperatures. This is indicative of additional motions occurring in the framework, which are quantified below.

At temperatures of 373 K and below, additional spectral intensity can be observed in the ^{13}C powder pattern at approximately 150 ppm. This may be indicative of an additional CO_2 adsorption site, or may simply be due to ^{13}C nuclei present in the linkers, which have expected chemical shift values between 161 ppm and 140 ppm.[33, 34]
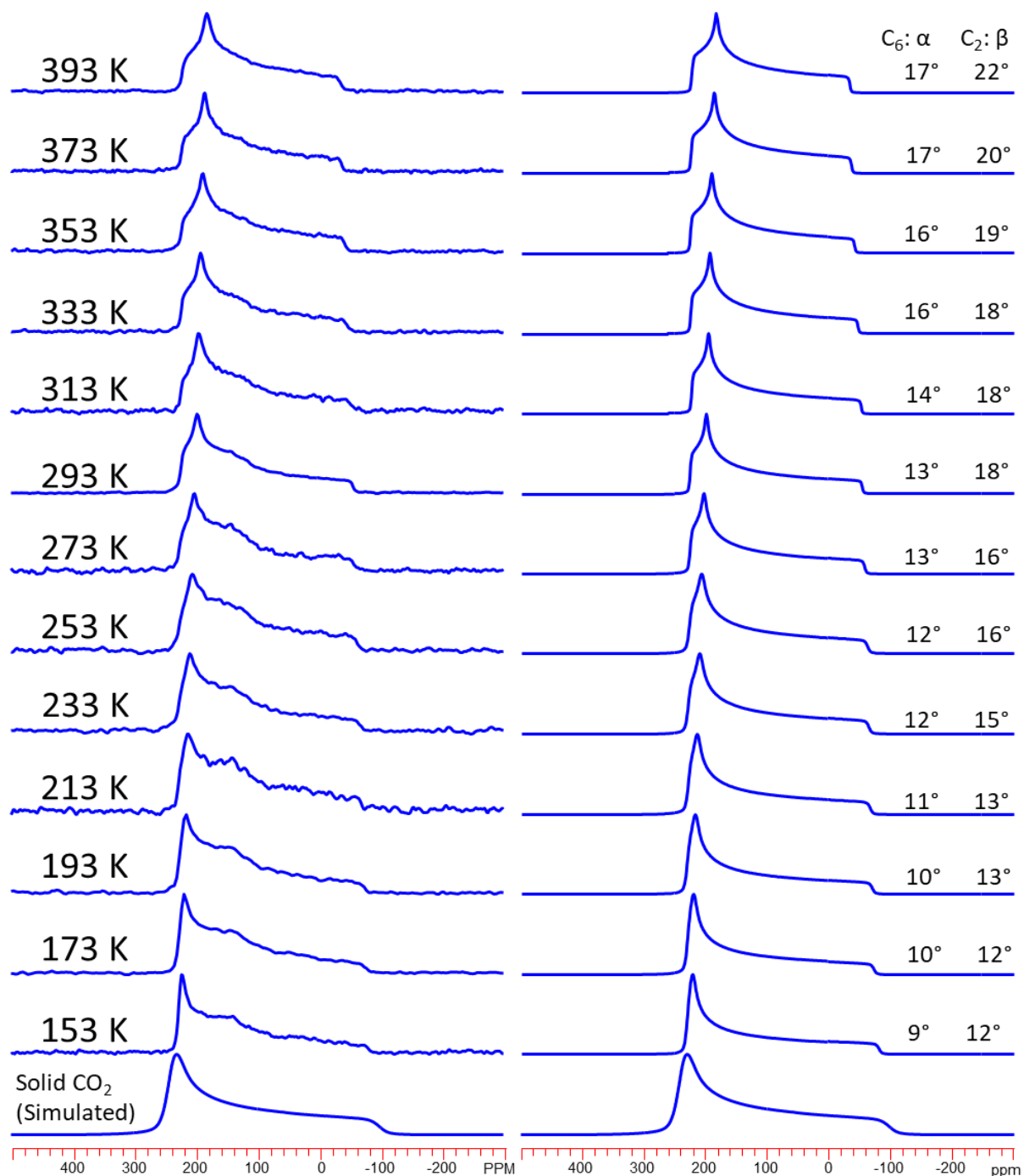
Figure 3.7: The experimental (left) and simulated (right) ^{13}C NMR spectra of $^{13}CO_2$-loaded ZnAtzOx(H_2O) are shown at temperatures varying from 393 K to 153 K. The spectra were collected using between 800 and 1000 scans and a 6 s recycle delay, except at 293 K where 3000 scans and a 20 s recycle delay was used. The C_6 rotational motion and C_2 hopping motion of CO_2 is described by the α and β angles listed on the simulated spectra. simulated spectra of solid CO_2 depicted on the bottom for reference.[27]
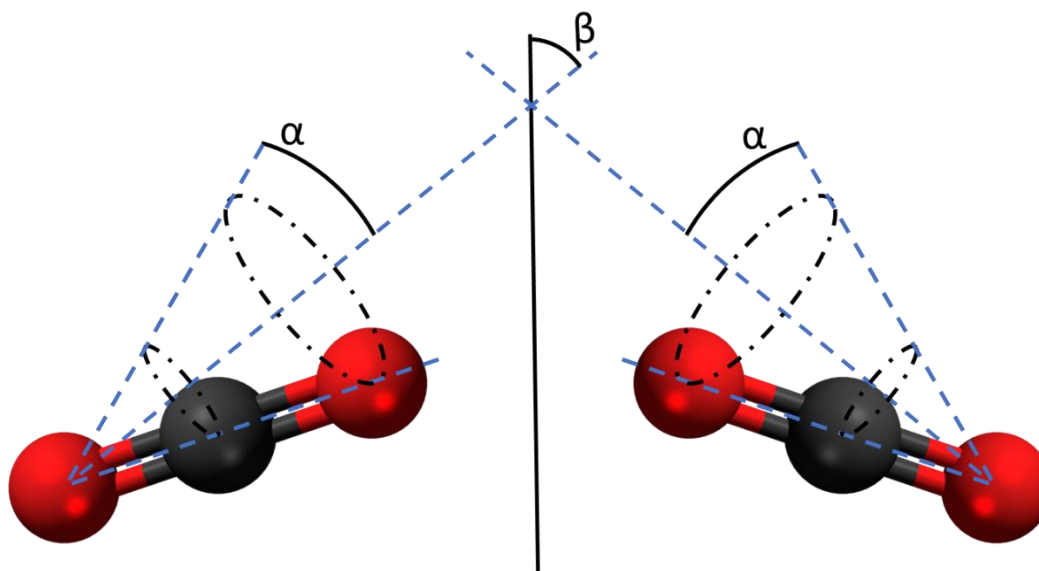
Figure 3.8: The wobbling and two-fold (C_2) hopping motions of a CO_2 molecule are shown above, and are described by the angles α and β respectively. For the purpose of EXPRESS[26] simulations, the wobbling motions are modelled as a six-fold (C_6) rotation. In practice, the molecule would be rotating about a continuous cone.

EXPRESS[26] simulations confirm the presence of C_2 hopping motions between equivalent adsorption sites, in addition to the wobbling motions modelled as C_6 rotation that were also observed in SIFSIX-3-Zn. These combined motions are depicted in Figure 3.8. The presence of hopping motions is likely due to the more open and interconnected nature of the pores in ZnAtzOx and fewer ^{1}H nuclei extending into the channel, rather than the narrow and confined 1-dimensional channels observed in SIFSIX-3-Zn containing numerous ^{1}H and ^{19}F nuclei proximate to the adsorbed CO_2. Both wobbling and hopping motions were observed at all temperatures. As in SIFSIX-3-Zn, the motional rate was found to exceed 10^7 Hz at all temperatures. The α angle, describing the C_6 wobbling, gradually increases from 9° to 17° as the temperature rises from 153

K to 393 K. The β angle, describing the C_2 hopping, similarly shows a gradual increase from 12°

to 22°.

Table 3.1: The observed ^{13}C chemical shift parameters of CO_2 adsorbed within ZnAtzOx(H_2O) are listed below. These parameters were obtained from analytical simulations of static ^{13}C SSNMR spectra using WSolids.[25]

Temperature (K)	δ$_{iso}$ (ppm)	Ω (ppm)	κ
393	124 (1)	256 (4)	0.69 (3)
373	125 (2)	259 (3)	0.71 (3)
353	125 (2)	265 (4)	0.74 (2)
333	124 (2)	270 (5)	0.77 (2)
313	123 (1)	275 (5)	0.80 (3)
293	124 (1)	278 (3)	0.81 (2)
273	124 (2)	282 (3)	0.84 (2)
253	124 (2)	288 (3)	0.86 (2)
233	125 (2)	292 (3)	0.87 (2)
213	126 (2)	295 (3)	0.90 (2)
193	126 (2)	299 (3)	0.91 (2)
173	126 (2)	301 (3)	0.93 (2)
153	124 (2)	311 (3)	0.94 (2)

3.3.2 ^{13}C direct MAS and CP/MAS SSNMR of $^{13}CO_2$ loaded ZnAtzOx(H_2O)

^{13}C MAS SSNMR experiments can help identify adsorption sites present within the porous

structure, in the event of changes in the chemical environment of the adsorbed CO_2. Combining

CP with MAS can provide direct evidence of dipolar interactions between the framework and guest

molecule.

MAS SSNMR experiments were performed on the $^{13}CO_2$ loaded ZnAtOx(H$_2$O) MOF. ^{13}C MAS and ^{1}H-^{13}C CP/MAS spectra are shown in Figure 3.9. In the ^{13}C MAS spectra, a sharp isotropic signal can be observed at 124 (1) ppm. This is identical the δ_{iso} obtained from static ^{13}C spectra on this CO_2 loaded structure. This signal can be assigned to $^{13}CO_2$ adsorbed within the framework.[27] No other strong ^{13}C resonances were identified at other chemical shift values, consistent with the static ^{13}C spectra.
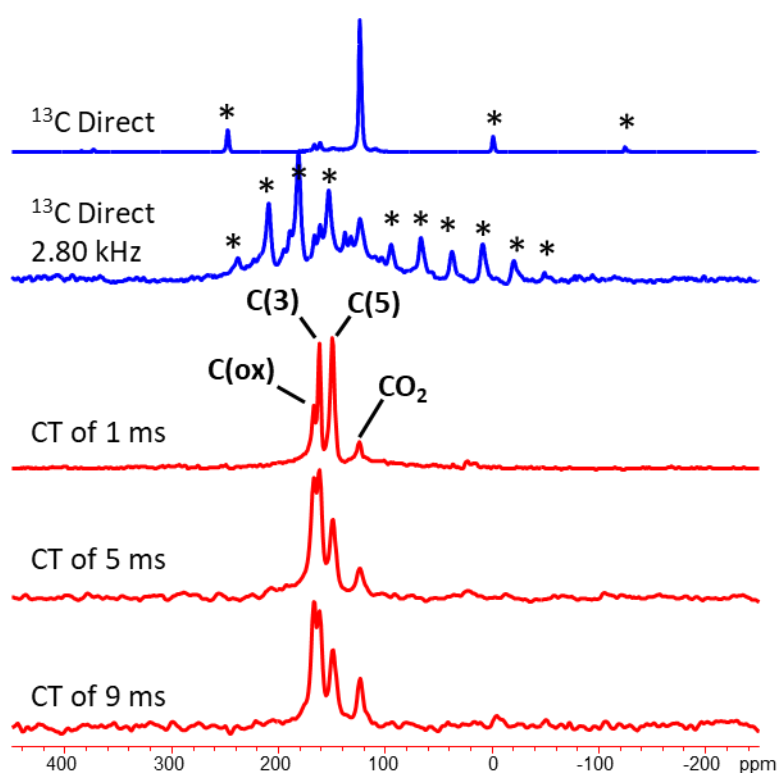
Figure 3.9: The experimental ^{13}C MAS SSNMR spectra of $^{13}CO_2$ loaded ZnAtzOx(H$_2$O) are all depicted above. The blue spectra were collected via direct excitation of ^{13}C nuclei using a one pulse sequence with approximately 400 scans and a 5 s pulse delay. The red spectra were collected using ^{1}H-^{13}C CP/MAS experiments, with 360 scans and a 10 s pulse delay. The contact times used for CP are listed to the left of the spectra. The MAS and CP/MAS spinning rate is 12.500 kHz unless otherwise noted. The notable sideband locations are indicated by asterisks.

Additional less intense resonances can be observed in ^{1}H-^{13}C CP/MAS spectra, which are centered at 168(1) ppm, 162(1) ppm, and 150(1) ppm. These resonances originate from ^{13}C nuclei within the oxalate and 3-amino-1,2,4-triazolate linkers present in the framework. Oxalic acid has a documented ^{13}C chemical shift of 160.77 ppm,[33] and 3-amino-1,2,4-triazole has reported ^{13}C chemical shifts of 154.7 ppm for C(3) and 140.5 ppm for C(5).[34]

Resonance assignments are indicated in Figure 3.9. The framework ^{13}C resonance intensities increases dramatically with the use of CP, as the framework ^{13}C nuclei are directly attached to ^{1}H. The resonance at 168 ppm most likely corresponds to the oxalate carbon, here referred to as C(ox), at it is the most distant from ^{1}H atoms within the framework, and is most enhanced by the use of a longer contact time (CT). Longer CTs allow for the enhancement of resonances from ^{13}C nuclei more distant from the ^{1}H nuclei. This is because the dipolar interaction mediating CP experiments is inversely related to the internuclear distance cubed, and as such requires the use of longer CTs to observe the full effects of CP. The resonance at 150 ppm likely corresponds to the C(5) atom within the 3-amino-1,2,4-triazolate linker, as it is directly bound to a ^{1}H atom, and its signal is not enhanced through the use of longer CTs.

The resonance from adsorbed ^{13}CO$_2$ was also enhanced with the use of CP, and with the use of longer CTs. This enhancement was much less notable versus that observed for the framework carbon nuclei, as it is not connected to the protons through chemical bonds. Qualitatively, the use of longer CTs appears to lead to a greater ^{13}CO$_2$ resonance intensity up to a CT of 9 ms. This suggests a degree of proximity between some of the guest carbon nuclei and framework protons and the presence of dipolar interactions between both nuclei.

Spinning sidebands from the adsorbed CO$_2$ signal are observed at 12 500 Hz intervals, which is a well-known phenomenon and is consistent with the spinning rate used when collecting

the spectra. A slow spinning (2800 Hz) MAS SSNMR spectrum was also collected for $^{13}CO_2$ loaded $ZnAtzOx(H_2O)$. The observed δ_{iso} was unchanged in this spectrum, though the spinning sidebands were brought closer to the central resonance and trace out the CSA-dominated static powder pattern (see Figure 3.6 above).

3.3.3 ^{13}C REDOR SSNMR of $^{13}CO_2$ loaded $ZnAtzOx(H_2O)$

^1H-dephased, ^{13}C REDOR-based experiments were used to investigate dipolar coupling strength between the framework and guest molecules in $ZnAtzOx(H_2O)$ to complement the information obtained in CP/MAS experiments. This is done through the use multiple rotor synchronized dephasing pulses applied to the ^1H spin, producing a reduced ^{13}C spectrum S_r. The magnitude of the dephasing will vary based on the strength of the dipolar interaction and the length of the dephasing time. The difference ΔS between the reduced and full S_0 ^{13}C spectra can be measured as a function of the dephasing time. The effects of dephasing on signal intensity should be predictable for a given dipolar coupling strength, allowing for an assessment of the strength of the dipolar coupling interaction.[35]

A room temperature ^1H-dephased ^{13}C REDOR spectrum of $ZnAtzOx(H_2O)$ can be found in Figure 3.10. The full spectrum (S_0), dephased spectrum (S_r), and difference spectrum (ΔS) are all depicted. The dephasing was performed for 28 rotor periods at a spinning speed of 10.000 kHz, for a total dephasing time of 0.0028 s. No dephasing effects were observed on the $^{13}CO_2$ resonance in the dephased spectrum, despite of the use of a relatively lengthy dephasing time.[36] However, dephasing effects were observed for the resonances at 166 ppm and 160 ppm. These resonances, as discussed above, correspond to the oxalate carbon and the C(3) carbon of 3-amino-1,2,4-triazole respectively. These carbon atoms are expected to be located 3.414 Å and 1.960 Å, respectively, from the nearest framework protons, based on the reported framework structure.[19] The spatial

proximity, and resulting dipolar coupling, strongly affects the magnitude of the observed dephasing. Due to the dramatic difference in the observed dephasing effect, effective proximity between the framework proton and guest carbon nuclei is lower than the effective proximity between the framework proton and framework carbon nuclei. Similar results were obtained when performing REDOR experiments at 223 K.
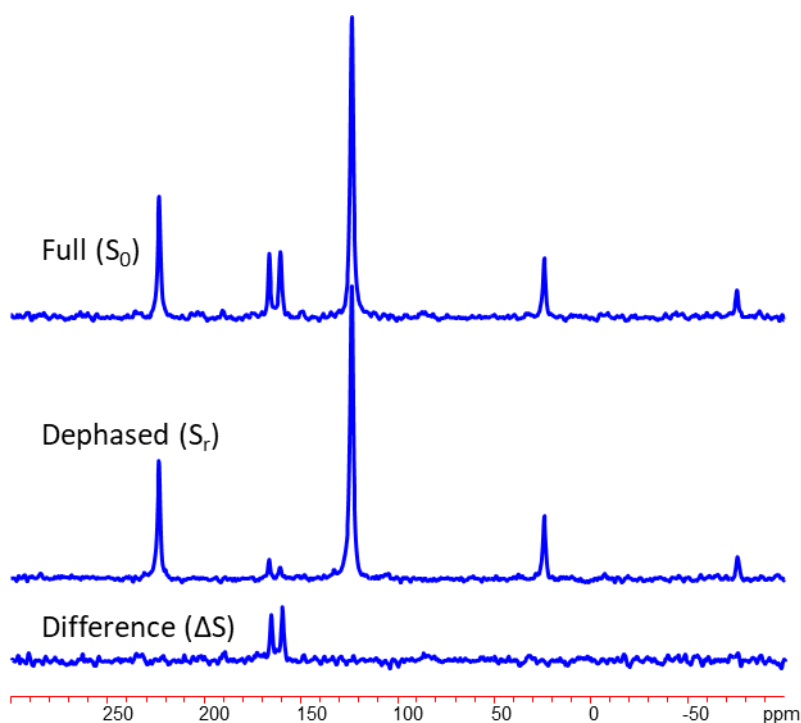
Figure 3.10: The room temperature experimental ^{1}H-dephased ^{13}C REDOR SSNMR spectra of ^{13}CO$_2$ loaded ZnAtzOx(H$_2$O) are shown above. These spectra were collected while spinning at 10 kHz with 44 scans and a 25 second recycle delay. The dephased spectrum was collected using a dephasing time of 0.0028 s.

Though REDOR-based experiments were able to provide evidence of dipolar interactions within SIFSIX-3-Zn, this is not the case in ZnAtzOx(H$_2$O). The CO$_2$ molecules possess greater

mobility, as was evidenced by static ^{13}C SSNMR patterns. Additionally, the ^{1}H-^{13}C CP experiments only weakly increased the signal of the adsorbed ^{13}C nuclei within ZnAtzOx(H$_2$O).

The nature of the pores in ZnAtzOx(H$_2$O) reduces dipolar coupling effects to the point that they are no longer detected through REDOR dephasing. The smaller number of nuclei extending into the pore proximate to the CO$_2$ adsorption site in ZnAtzOx likely contributes to the weaker observed effects than in SIFSIX-3-Zn. This suggests only weak host-guest interactions with CO$_2$ at room temperature and temperatures of 223 K. This illustrates the importance of pore nature and guest motion on host-guest interactions within ultramicroporous frameworks.
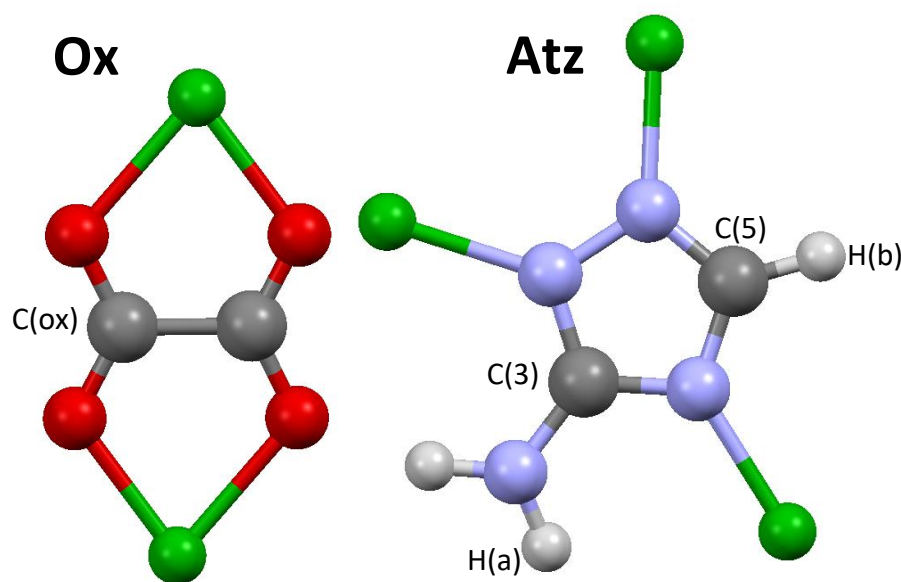
Figure 3.11: The structures of the oxalate (Ox) and 3-Amino-1,2,4-triazolate (Atz) linkers are shown above. The Atz linker contains two carbon nuclei, referred to here as C(3) and C(5), which are proximate to ^{1}H nuclei H(a) and H(b). The Ox also contains two chemically equivalent carbon nuclei, C(ox), which are distant from any ^{1}H nuclei.

3.3.4   Two-dimensional ^{1}H-^{13}C HETCOR SSNMR of ZnAtzOx(H$_2$O)

Two-dimensional correlation spectroscopy allows for the ^{1}H and ^{13}C signals obtained using MAS SSNMR to be correlated with one another. This was done using FSLG-HETCOR experiments at 21.1 T, to determine the proximity of heteronuclei to one another. FSLG-HETCOR essentially functions as two-dimensional CP SSNMR, correlating nuclei based on the strength of their dipolar interactions, increasing spectrum resolution, and increasing the separation of overlapping peaks. For this purpose, it is useful to understand in more detail the linker chemistry in ZnAtzOx(H$_2$O). Each Atz linker, shown in Figure 3.11, contains two carbon nuclei, C(3) and C(5), two ^{1}H nuclei bound to the amine group, H(a), and one ^{1}H nucleus bound to the Atz ring, H(b). Each Ox linker contains two chemically identical carbon nuclei, C(ox) and no ^{1}H nuclei.
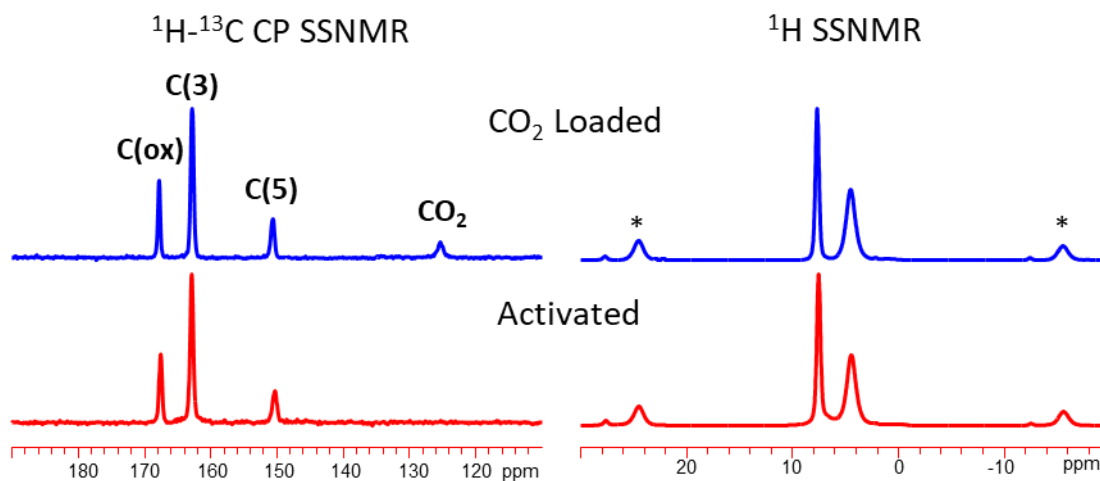
Figure 3.12: The experimental one-dimensional ^{1}H-^{13}C CP and ^{1}H SSNMR spectra of CO$_2$ loaded (blue) and activated (red) ZnAtzOx(H$_2$O) are shown above. Previously assigned carbon resonances are labelled. Asterisks indicate spinning sidebands. A contact time of 5 ms was used for CP spectra. CP spectra were collected using 512 scans and a recycle delay of 10 s. ^{1}H spectra were collected using 32 scans and a recycle delay of 10 s.

One-dimensional ^{1}H-^{13}C CP SSNMR spectra and one dimensional ^{1}H SSNMR spectra are shown in Figure 3.12. ^{13}C resonance assignments are discussed above, based on literature chemical shifts of oxalic acid and 3-amino-1,2,4-triazole and based on the effects of ^{1}H-^{13}C CP experiments. The one-dimensional ^{1}H SSNMR spectra had resonances at 4.5(1) ppm and 7.7(1) ppm. Literature ^{1}H chemical shifts of 3-amino-1,2,4-triazole include a resonance at 5.78 ppm from the protons on amine group and a resonance at 7.48 ppm from the proton on the ring.[37]
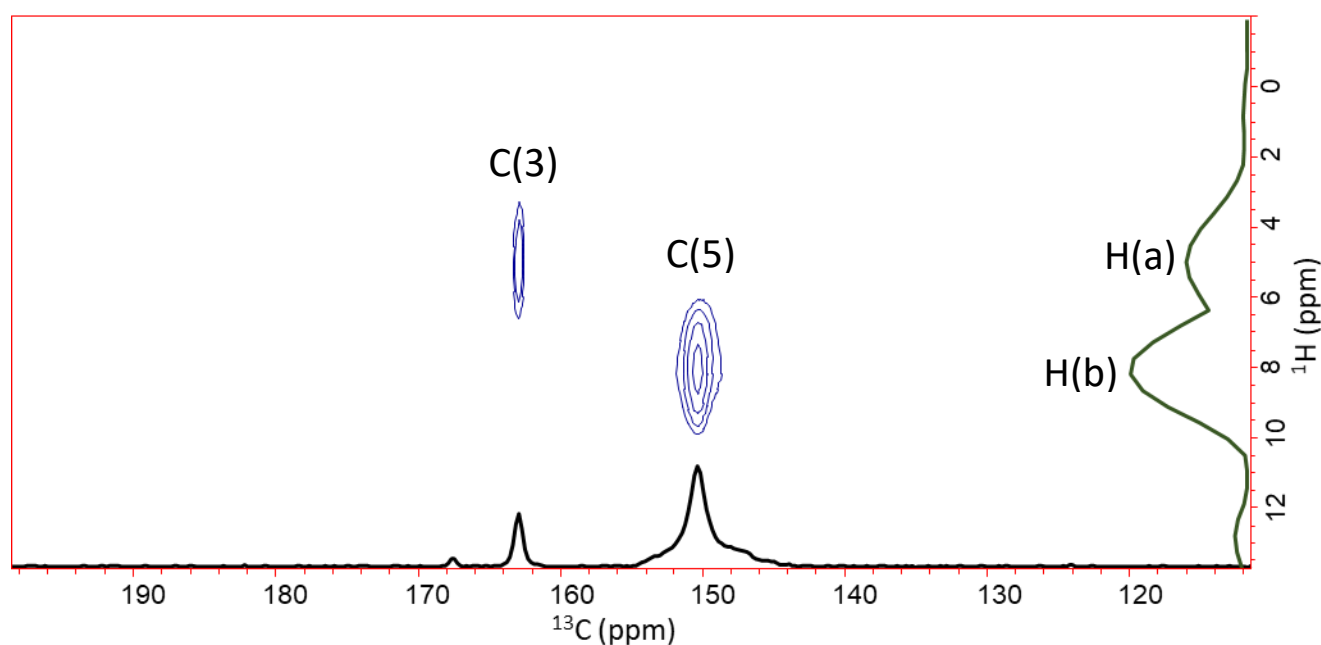
Figure 3.13: The 2D FSLG-HETCOR spectrum of activated ZnAtzOx(H₂O) is shown above. The spectrum was collected at 293 K while spinning at 18 kHz using 32 points across the indirect dimension, 400 scans and a 5 second recycle delay. A contact time of 500 μs was used for the HETCOR experiment. The one-dimensional ^{1}H-^{13}C CP spectrum is projected along the bottom in black, while the one-dimensional ^{1}H spectrum is projected along the right in green.

The 2D HETCOR spectrum for the activated phase is shown in Figure 3.13. This spectrum correlates the ^{1}H resonance at 4.5 ppm with the ^{13}C resonance at 162 ppm, from C(3), suggesting

this ^{1}H resonance corresponds to H(a). The ^{1}H resonance at 7.7 ppm is likewise correlated to the ^{13}C resonance at 150 ppm, from C(5), meaning the ^{1}H resonance corresponds H(b). These assignments are consistent with the literature ^{1}H chemical shifts of 3-amino-1,2,4-triazole. The ^{1}H resonances can therefore be assigned with certainty.
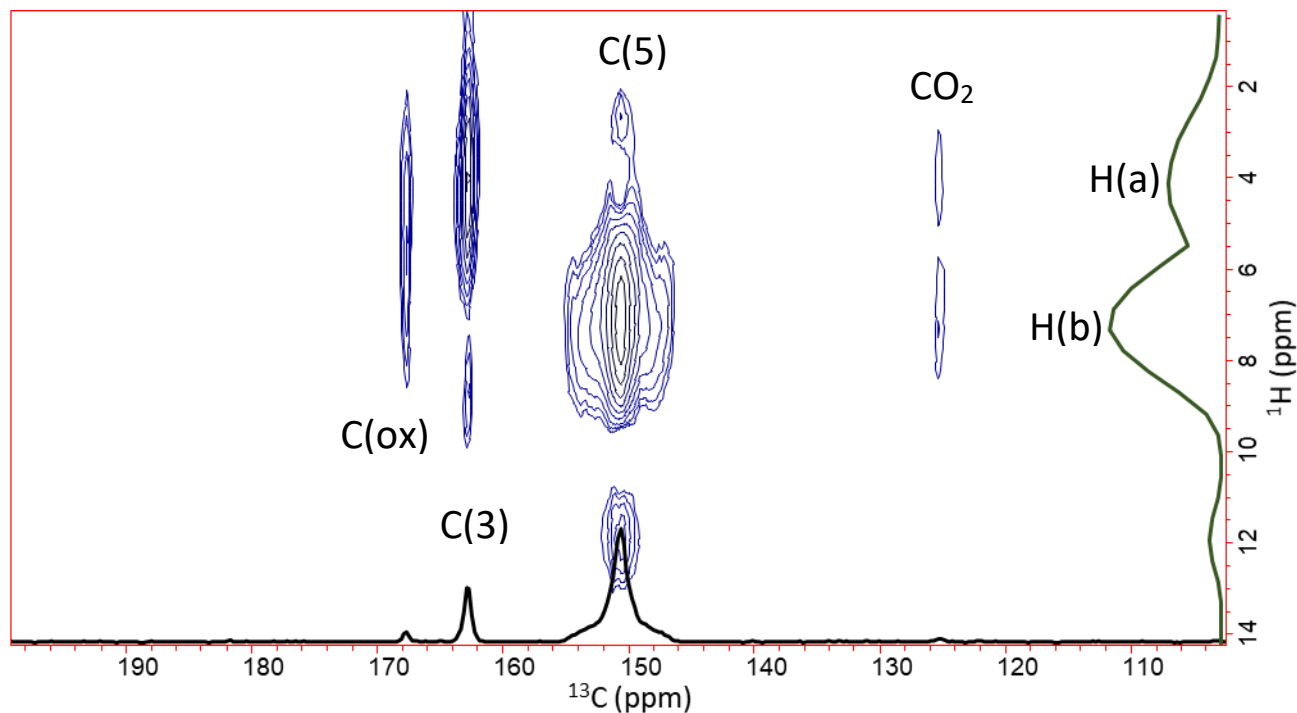
Figure 3.14: The 2D FSLG-HETCOR spectrum of $^{13}CO_2$ loaded ZnAtzOx(H$_2$O) is shown above. The spectrum was collected at 293 K while spinning at 18 kHz using 32 points across the indirect dimension, 400 scans and a 5 second recycle delay. A contact time of 500 µs was used for the HETCOR experiment. The one-dimensional ^{1}H-^{13}C CP spectrum is projected along the bottom in black, while the one-dimensional ^{1}H spectrum is projected along the right in green.

FSLG-HETCOR should also function through space to link framework ^{1}H nuclei to the adsorbed ^{13}C nuclei within guest CO_2 molecules. This can be seen in Figure 3.14, depicting the 2D HETCOR spectrum of $^{13}CO_2$ loaded ZnAtzOx(H$_2$O). The correlation between guest ^{13}C and

framework ^{1}H is significantly weaker than the correlations between framework ^{13}C and ^{1}H. This is unsurprising given the weak dipolar interactions that were observed through CP/MAS and REDOR experiments. The ^{13}C resonance at 125(1) ppm from the adsorbed CO_2 appears weakly correlated to both ^{1}H framework signals. This suggests the adsorbed $^{13}CO_2$ molecule is not selectively proximate to either the H(a) or the H(b), but is rather somewhat proximate to both sites at 293 K. The CO_2 is therefore too mobile within $ZnAtzOx(H_2O)$ to possess a strong specific adsorption site at room temperature.

3.3.5   Static ^{67}Zn SSNMR of as made, activated and CO_2 loaded $ZnAtzOx(H_2O)$

The Zn centres can be investigated using high field NMR, in order to assess changes in the metal centre of the MOF as guest molecules are evacuated and loaded into the framework. Investigation of the electric field gradient (EFG) about the ^{67}Zn nuclei was performed using ^{67}Zn SSNMR at an ultrahigh magnetic field of 21.1 T on as made, activated and CO_2 loaded $ZnAtzOx(H_2O)$ samples. The $ZnAtzOx(H_2O)$ framework possesses two distinct Zn environments, referred to here as Zn(1) and Zn(2).[19] The experimental powder pattern was therefore simulated as two distinct Zn sites, to determine the quadrupolar coupling parameter (C_Q) and asymmetry parameter (η_Q) values. The experimental and simulated $ZnAtzOx(H_2O)$ spectra are shown in Figure 3.15. The C_Q and η_Q were also calculated using the CASTEP software package.[28] The C_Q and η_Q values that were determined experimentally and through calculations are shown in Table 3.2.

The C_Q and η_Q values obtained from experimental spectra were in moderate agreement with those obtained from theoretical calculations. A crystal structure for the activated framework was not available in the literature, and was modeled by removing H_2O molecules from the reported structure of the as made framework.[19] When geometry optimization was performed on this

framework, the computed C_Q and η_Q values were found to be similar to experimental results from the activated structure.

A comparison of the experimental and calculated static ^{67}Zn SSNMR spectra is shown in Figure 3.15. The overall shape of experimental and calculated spectra are similar. Though the samples studied were confirmed to be ZnAtzOx(H_2O), there were nevertheless some differences between calculated and experimental C_Q and η_Q values. This may be due to localized disorder about individual ^{67}Zn nuclei affecting the symmetry of the EFG.

Table 3.2: The observed and calculated ^{67}Zn CS parameters of ZnAtzOx(H_2O) samples are listed below. These parameters were obtained from analytical simulations of ^{67}Zn SSNMR spectra, and calculated for the reported and geometry optimized structures of ZnAtzOx(H_2O).

Sample	C_Q (MHz)	η_Q
Activated, Experimental – Zn(1)	5.8 (2)	0.6 (1)
Activated, Experimental, – Zn(2)	6.5(3)	0.6(1)
As Made, Experimental – Zn(1)	5.8 (2)	0.8(2)
As Made, Experimental – Zn(2)	6.5(3)	0.9(1)
CO_2 Loaded, Experimental – Zn(1)	5.8 (2)	0.6 (1)
CO_2 Loaded, Experimental, – Zn(2)	6.5(3)	0.6(1)
Activated, Calculated, Unoptimized – Zn(1)	4.56	0.549
Activated, Calculated, Unoptimized – Zn(2)	8.952	0.945
Activated, Calculated, Optimized – Zn(1)	5.788	0.667
Activated, Calculated, Optimized – Zn(2)	7.467	0.524
As Made, Calculated, Optimized – Zn(1)	7.217	0.449
As Made, Calculated, Optimized – Zn(2)	6.970	0.924

Overall, the EFG of the ^{67}Zn nuclei appears to possess a low C_Q values and a high η_Q, with experimental C_Q values of 5.8 MHz for Zn(1) and 6.5 MHz for Zn(2), and an η_Q of greater than

0.4 for all Zn sites. Five-coordinate Zn is often highly asymmetrical, resulting in higher C_Q values than what was observed for ZnAtzOx(H_2O).[38] The activated structure and CO_2 loaded structure produced identical ^{67}Zn SSNMR patterns, suggesting that the presence of CO_2 does not affect the EFG or local electric environment about the Zn nucleus; CO_2 has little to no effect on the local Zn environment and it seems that Zn plays no direct role in CO_2 adsorption within this system.
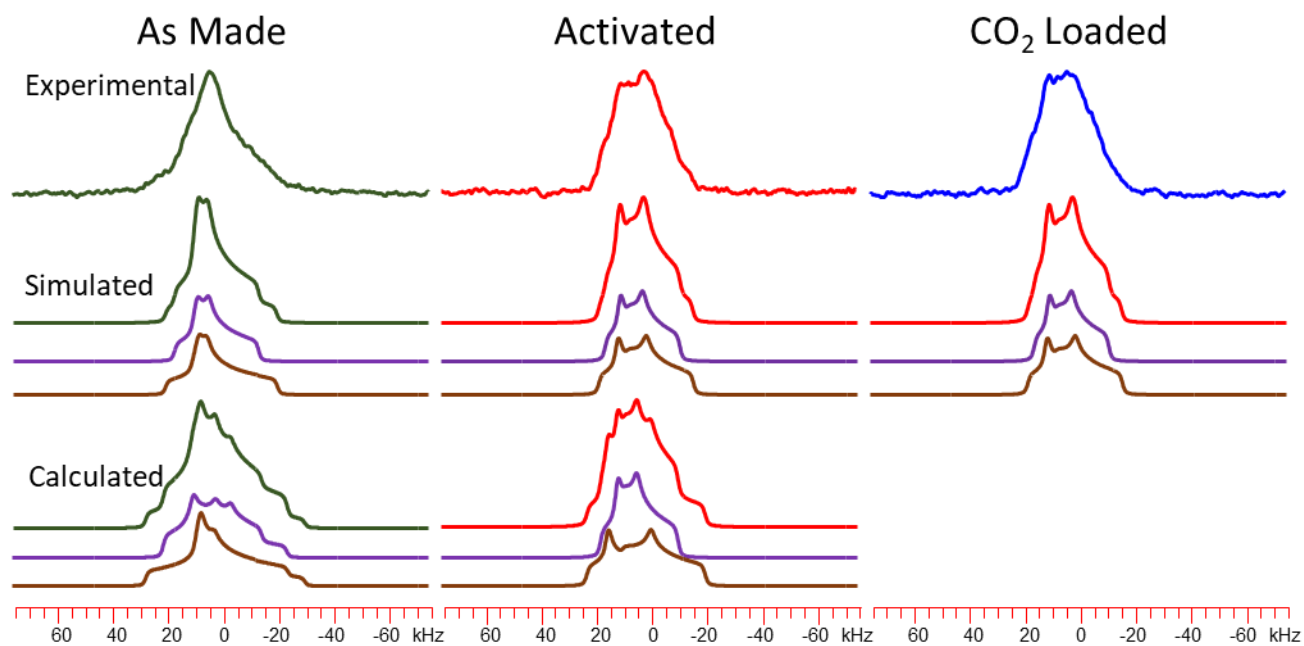
Figure 3.15: The experimental, simulated and calculated static ^{67}Zn NMR spectra of as made, activated and CO_2 loaded ZnAtzOx(H_2O) are shown above, as acquired at a magnetic field of 21.1 T. 160 000 scans were used with a recycle delay of 0.5 s. A calculated spectra for the CO_2 loaded phase was not constructed, due to the lack of a SCXRD structure for the CO_2 loaded phase. Simulated and calculated patterns for Zn(1) are shown in purple, while patterns for Zn(2) are shown in brown.

Looking at the distribution of bond lengths and angles about the Zn^{2+} ions can offer insight into why the C_Q and η_Q values change in different phases of this MOF. Larger parameter

distributions should increase the value of the C_Q parameter. Both Zn sites possess a distorted trigonal-bipyramidal geometry. A comparison of the sites is shown in Figure 3.16.

Zn(1), As Made, C_Q of 7.217 MHz

Zn(2), As Made, C_Q of 6.970 MHz

Zn(1), Activated, C_Q of 5.788 MHz

Zn(2), Activated, C_Q of 7.467 MHz
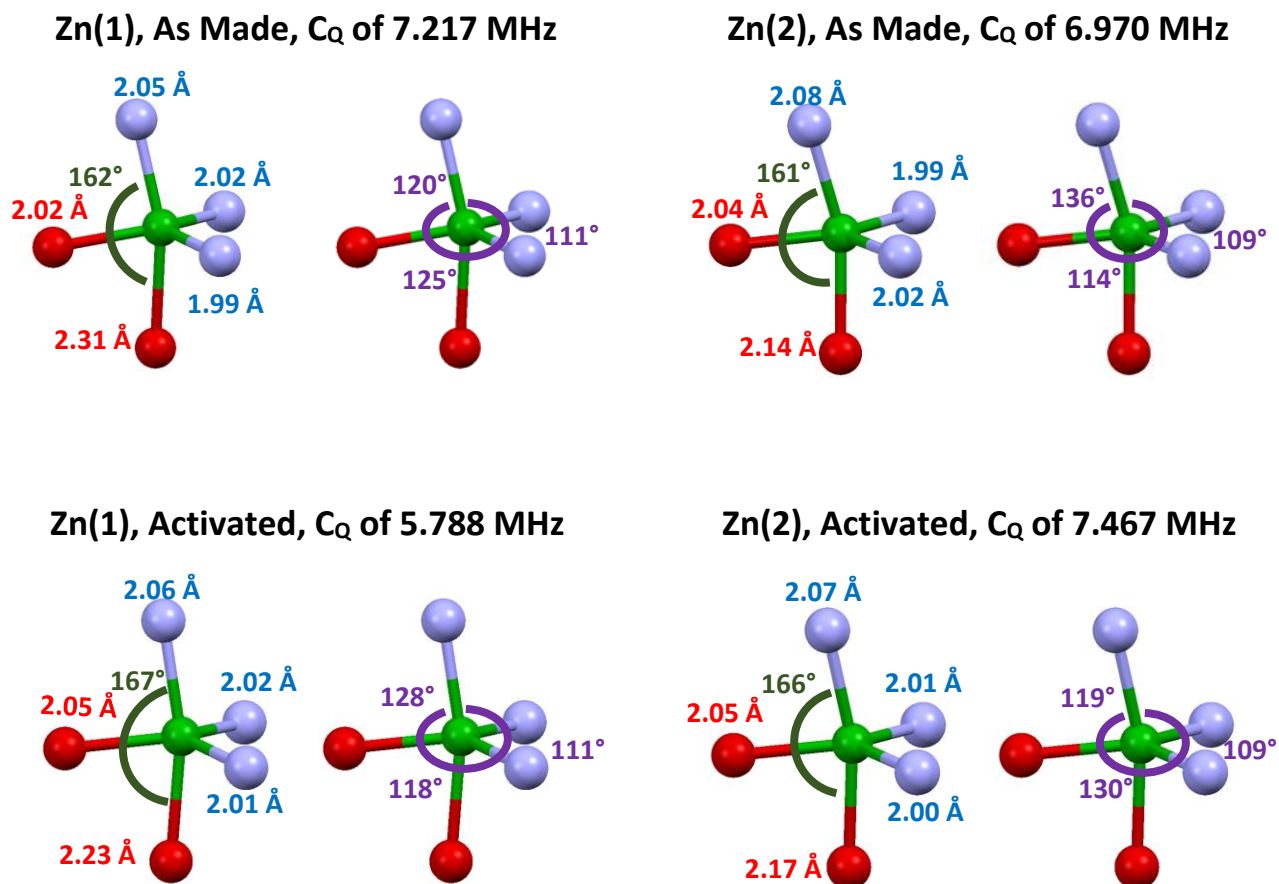
Figure 3.16: The local geometry of the Zn sites in the geometry optimized ZnAtzOx(H₂O) structures are shown above, along with their calculated C_Q values. The Zn – O bond lengths are shown in red, and the Zn – N bond lengths are shown in blue. The angle between axial Zn – O and Zn – N bonds is shown in green. The angles between equatorial Zn – O and Zn – N bonds are shown in purple.

The lack of a symmetrical rotation axis about the various Zn nuclei is consistent with the high η_Q values determined for each site, listed in Table 3.2. When looking at bond lengths and

angles, there is mostly little change in the measured values between different Zn sites and MOF phases. However, the bond length between Zn and the axial oxygen atom contracts and elongates significantly when comparing different sites and phases.

Calculations suggest that after activation, Zn(1) should experience large decrease in C_Q from the as made form, while Zn(2) should experience moderate increase in C_Q.

This can be related to changes in the axial Zn – O bond length. The Zn(1) axial Zn – O bond length decreases by 0.083 Å after activation, correlated with a decreasing C_Q. The Zn(2) axial Zn – O bond length increases by 0.32 Å after activation, correlated with an increasing C_Q. This suggests the axial Zn – O bond length is generally linked to C_Q values, with a greater bond length leading to a higher C_Q value. The angles between axial Zn – O and Zn – N, shown in green in Figure 3.16, also increases slightly after activation for both sites (from 162° and 161° to 167° and 166°), reducing the distortion on the trigonal bipyramidal structure. This can be expected to cause an overall decrease in C_Q.

However, the C_Q values of Zn(2) seem notably higher than those of Zn(1) given the shorter axial Zn – O bond lengths. Aside from these bond lengths, the most notable difference in geometries between sites is the equatorial bond angle distribution. A greater angle distribution distors the trigonal bipyramidal structure, and can be expected to increase the C_Q parameter. These angles are listed in purple in Figure 3.16.

Within Zn(1), the equatorial bond angles in the as made phase have a value of 118.97° ± 6.98°, while the Zn(2) angles have a value of 119.59° ± 14.03°, with a much larger variance. Similarly in the activated phase, the equatorial bond angles are 119.05° ± 8.33° for Zn(1) and 119.42° ± 10.37° for Zn(2). The consistently greater variance in equatorial bond angles for the

Zn(2) site explains the higher C_Q values for Zn(2) given the shorter axial Zn – O bond lengths, as this greater variance distorts the trigonal bipyramidal geometry.

This highlights the importance of the axial Zn – O bond lengths and equatorial bond angle distributions on the spherical symmetry of the EFG about ^{67}Zn within the ZnAtzOx(H_2O). In both Zn sites, the change in the axial Zn – O bond length distributions was correlated with a corresponding change in the C_Q parameter. When comparing different Zn sites, the greater bond angle distribution in Zn(2) appeared to be responsible for higher C_Q values.

3.3.6 Static VT ^{13}C SSNMR of $^{13}CO_2$ loaded ZnAtzOx(EtOH)

ZnAtzOx(H_2O) is known to possess the highest CO_2 uptake among ZnAtzOx phases, though it is not the only phase of the MOF known to adsorb CO_2. The ethanol synthesized phase, here referred to as ZnAtzOx(EtOH), possesses a significantly lower CO_2 uptake than ZnAtzOx(H_2O).[19] The difference in CO_2 uptake is thought to result from changes in the oxalate linker bonds altering the shape of the pore to be less condusive to CO_2 adsorption. This dramatic change in adsorption performance from subtle changes in the framework structure can be better understood with the aid of SSNMR experiments, providing insight into the guest behaviours present in ultramicroporous MOFs.

Static VT ^{13}C SSNMR experiments were performed on the ZnAtzOx framework synthesized solvothermally within ethanol, to determine whether subtle pore shape differences between ZnAtzOx phase was affecting CO_2 motional behaviour as well as the maximum CO_2 uptake of the framework. The experimental and simulated powder patterns can be seen in Figure 3.17, and CS parameters of the simulated powder patterns are listed in Table 3.3. These experiments identified two distinct CO_2 adsorption sites within the framework, with a third site

becoming apparent at lower temperatures. All simulated patterns had δ_{iso} values characteristic of the CO_2 carbon nuclei, identical to the δ_{iso} of ^{13}C resonances in ZnAtzOx(H_2O).
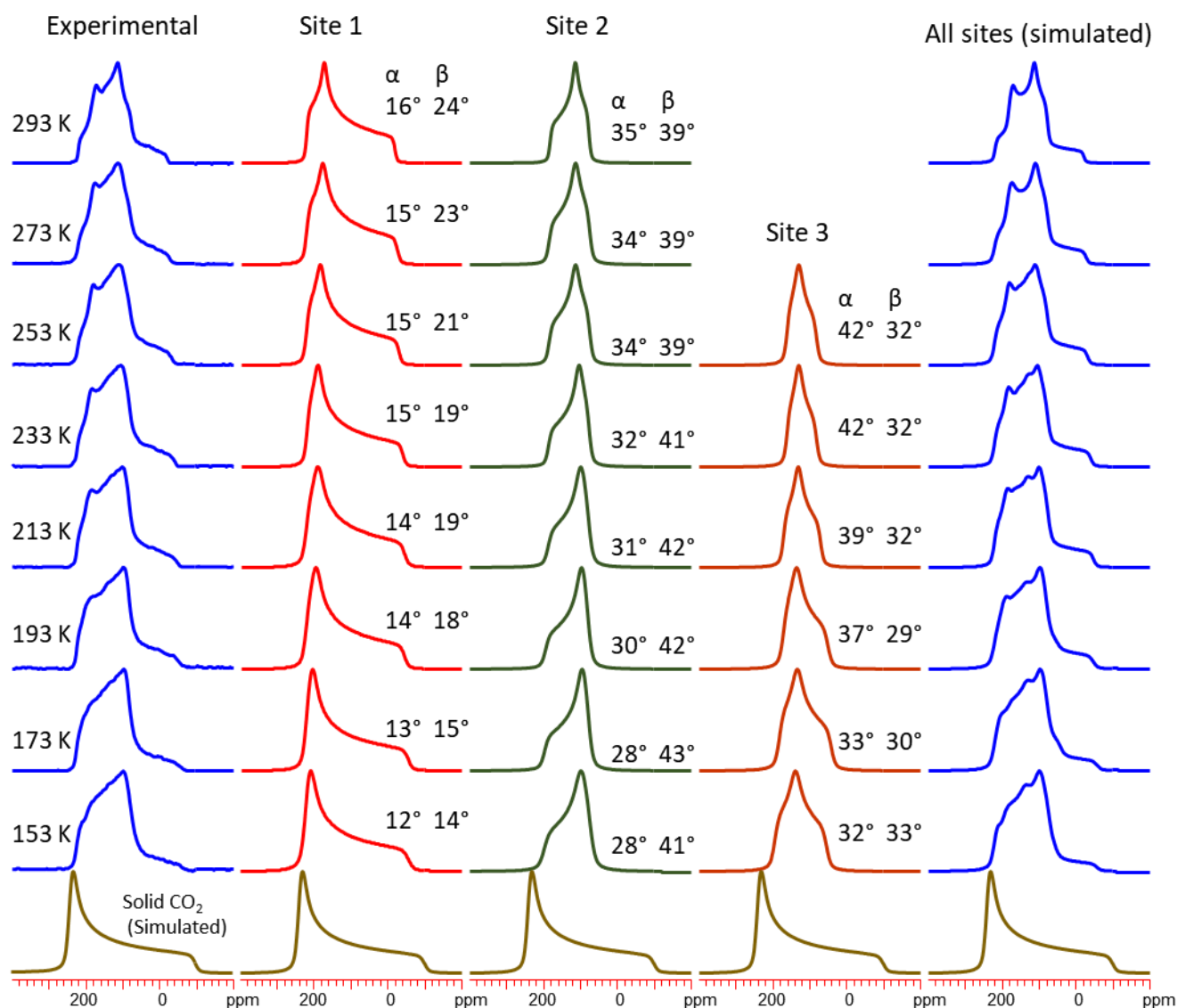
Figure 3.17: The experimental (left) and simulated site 1 (middle) and site 2 (right) ^{13}C NMR spectra of $^{13}CO_2$-loaded ZnAtzOx(EtOH) are shown at temperatures varying from 293 K to 153 K. Spectra were collected using between 100 and 200 scans and a 10 s recycle delay, except at 293 K where 6000 scans and a 10 s recycle delay was used. The C_6 rotational motion and C_2 hopping motion of CO_2 is described by the α and β angles listed on the simulated spectra. Simulated spectra of solid CO_2 depicted on the bottom for reference.[27]

WSolids[25] simulations of the adsorption site in ZnAtzOx(H_2O) quantified the Ω value as 278(3) ppm and the κ value as 0.81(2) for the ^{13}C SSNMR powder pattern of adsorbed [13]CO_2 guest molecules at 293 K. This was determined to correspond to an α of 13° and a β of 18°. However, for [13]CO_2 adsorbed within ZnAtzOx(EtOH), the primary adsorption site possessed Ω and κ values at 293 K of 240(3) ppm and 0.60(2) respectively. This indicates notable differences in CO_2 motional behaviour within the two structures. Therefore, not only was the solvent induced phase change significantly affecting the CO_2 uptake capacity, but also affecting the motional behaviour of CO_2 within the framework pores.

A third CO_2 adsorption site does not become apparent until temperatures of 253 K and lower. At 253 K this new site comprises approximately 10% of the pattern intensity, a Ω of 80(20) ppm and a κ of 0.2(2). The intensity and Ω values increase as the temperature decreases, with the apparent parameters at 153 K being 25% of the pattern intensity and 140(10) ppm. This suggests that the binding energy within the third site is too weak to adsorb CO_2 at higher temperatures. An alternative possiblity structural changes within the MOF at low temperatures may be opening an additional third adsorption CO_2 site and perhaps restrict the occupation of sites 1 and 2.

EXPRESS[26] simulations confirm the presence of both C_6 wobbling motions and C_2 hopping motions for the CO_2 located at all adsorption sites. These motional angles were determined with an estimated error of 2°. The CO_2 in these sites display greater α and β angles than the CO_2 adsorbed in ZnAtzOx(H_2O). The motional rate was found to exceed 10^7 Hz in all cases. In site 1, the α angle gradually increases from 12° to 16° as the temperature rises from 153 K to 293 K. The β angle shows a gradual increase from 14° to 24°. These angles are slightly greater than those describing the CO_2 motions in ZnAtzOx(H_2O). The motional angles for CO_2 within the second site are significantly greater, with α angles between 28° and 35°, and β angles between 39°

and 43°. The greater degree of motion suggests weaker guest – host interactions within the second adsorption site. The CO_2 within the third site exhibits similarly large motional angles, with α angles between 32° and 42° and β angles between 29° and 33°.

Table 3.3: The observed ^{13}C chemical shift parameters of CO_2 adsorbed within ZnAtzOx(EtOH) are listed below, for all CO_2 adsorption sites. These parameters were obtained from analytical simulations of static ^{13}C SSNMR spectra using WSolids.[25]

Temperature (K)	δ_{iso}, Site 1 (ppm)	Ω, Site 1 (ppm)	$^1\kappa$, Site 1	δ_{iso}, Site 2 (ppm)	Ω, Site 2 (ppm)	κ, Site 2
293	125 (2)	240 (3)	0.60 (2)	125 (2)	105 (5)	-0.3 (1)
273	124 (2)	247 (3)	0.64 (2)	125 (2)	110 (5)	-0.3 (1)
253	125 (2)	251 (3)	0.70 (2)	125 (2)	110 (5)	-0.3 (1)
233	123 (2)	260 (3)	0.73 (3)	123 (2)	110 (5)	-0.5 (1)
213	122 (2)	267 (5)	0.76 (3)	122 (2)	110 (5)	-0.6 (1)
193	124 (2)	267 (5)	0.80 (3)	124 (2)	115 (5)	-0.7 (1)
173	124 (2)	277 (5)	0.88 (5)	124 (2)	120 (5)	-0.7 (1)
153	127 (2)	275 (5)	0.95 (5)	124 (2)	125 (5)	-0.6 (1)

Temperature (K)	δ_{iso}, Site 3 (ppm)	Ω, Site 3 (ppm)	κ, Site 3	Intensity, Site 1	Intensity, Site 2	Intensity, Site 3
333				30%	70%	0%
313	-	-	-	40%	60%	0%
293	-	-	-	50%	50%	0%
273	-	-	-	50%	50%	0%
253	125 (5)	80 (20)	0.2 (2)	55%	35%	10%
233	125 (5)	80 (20)	0.2 (2)	55%	30%	15%
213	125 (5)	100 (10)	0.2 (1)	55%	30%	15%
193	120 (5)	120 (10)	0.4 (1)	50%	35%	15%
173	120 (5)	140 (10)	0.3 (1)	40%	35%	25%
153	130 (5)	140 (10)	0.2 (1)	30%	45%	25%

Despite the similar framework structure in ZnAtzOx(H_2O) and ZnAtzOx(EtOH), the motional behaviour of the adsorbed CO_2 changes notably between the two frameworks. The slight changes in pore dimensions create changes in the strength of the adsorption interaction, in addition to changing the overall framework uptake as has been previously reported.[19]

3.3.7 ^{13}C direct MAS $^{13}CO_2$ loaded ZnAtzOx(EtOH)

Direct excitation ^{13}C MAS SSNMR experiments were performed on ZnAtzOx(EtOH) at 293 K to help characterize the CO_2 adsorption sites within the framework. The resulting spectrum can be seen in Figure 3.18.
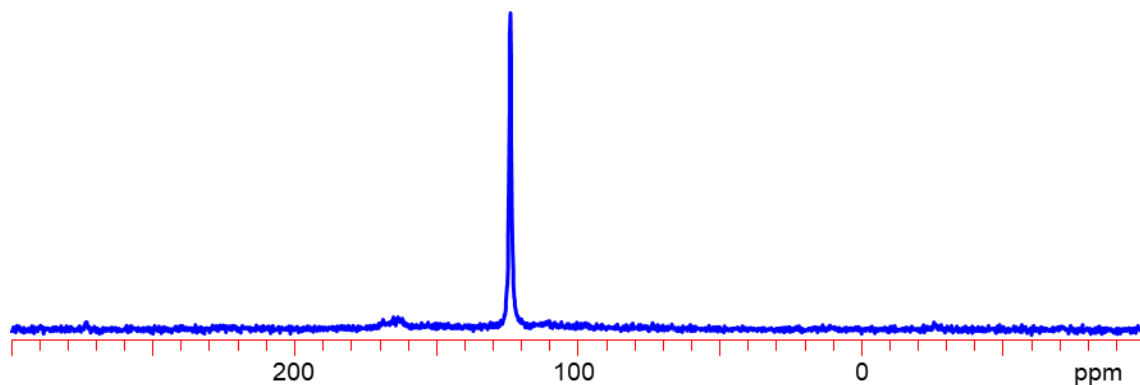
Figure 3.18: The experimental ^{13}C MAS SSNMR spectrum of $^{13}CO_2$ loaded ZnAtzOx(EtOH) is depicted above. The spectrum was collected via direct excitation of ^{13}C nuclei using a one pulse sequence with approximately 100 scans and a 10 s pulse delay. The MAS spinning rate is 15.000 kHz.

A sharp signal can be observed at 124(1) ppm, corresponding to ^{13}C nuclei within the adsorbed $^{13}CO_2$ molecules. There is also a weak resonance from the carbon within the linkers, observed between 160 and 170 ppm. These results are almost identical to those that were obtained after similar experiments on ZnAtzOx(H_2O), which is expected given the similarities of both structures.

While two CO_2 adsorption sites were identified in the static room temperature ^{13}C SSNMR spectra of ZnAtzOx(EtOH), only a single unique adsorbed ^{13}C resonance was identified in MAS experiments. This suggests the two adsorption sites are chemically equivalent, likely due to weak interactions between the guest CO_2 and the host ZnAtzOx(EtOH) framework. This is consistent with static ^{13}C SSNMR powder patterns of the CO_2 loaded framework, where the δ_{iso} values for both sites were found to be identical.

3.4   Conclusions

Using static and MAS SSNMR experiments on the water synthesized ZnAtzOx MOF, CO_2 motional behaviour and guest-host interactions have been explored. Similar to the previously discussed SIFSIX-3-Zn MOF, the ultramicroporous nature of ZnAtzOx leads to well-defined CO_2 motions with a relatively low temperature dependence within the framework. The nature of the channels within ZnAtzOx lead to notably more CO_2 mobility within the framework than was observed within SIFSIX-3-Zn, and both CO_2 hopping and rotational wobbling motions could be quantified using EXPRESS simulations.[26]

^1H-^{13}C CP/MAS SSNMR experiments reveal the magnitude of dipolar coupling and proximity between the two nuclei, suggesting the existence of weak dipolar interactions between the guest ^{13}C and framework ^1H nuclei. FSLG-HETCOR experiments found these interactions were not strongly directed towards one framework ^1H nucleus over another, and that the CO_2 does not possess a strong specific room temperature adsorption site. Additional ^{67}Zn SSNMR experiments and calculations also revealed insight into the changes in Zn nuclei symmetry as water was evacuated from the framework, with an increase in the C_Q value for the Zn(1) site and an decreasing C_Q value for the Zn(2) site after activation of the as made structure. This is likely due

to the changes in bond angle and bond length distributions about the nuclei, particularly the axial Zn – O bond lengths.

As ultramicroporous MOFs like ZnAtzOx and SIFSIX-3-M are subjected to increasing interest due to their unusually high CO_2 selectivity and CO_2 uptakes, it has become important to understand how CO_2 interacts with these frameworks, and to make sense of the trends in CO_2 motions. SSNMR experiments have provided information on these structures not available through other experimental methods, and illustrate that a sharp contrast exists between CO_2 behaviour in these highly selective ultramicroporous MOFs and CO_2 within selective microporous or mesoporous MOFs.

3.5   References

1.   Stocker, T. F.; Qin, D.; Plattner, G.-K.; Tignor, M.; Allen, S. K.; Boschung, J.; Nauels, A.; Xia, Y.; Bex, V.; Midgley, P. M., *Climate Change 2013: The Physical Science Basis. Contribution of Working Group I to the Fifth Assessment Report of the Intergovernmental Panel on Climate Change*. Cambridge University Press: Cambridge, United Kingdom and New York, NY, USA, 2013; p 1535.
2.   Goeppert, A.; Czaun, M.; Prakash, G. K. S.; Olah, G. A., Air as the renewable carbon source of the future: an overview of CO_2 capture from the atmosphere. *Energy & Environmental Science* **2012,** *5* (7), 7833-7853.
3.   Pires, J. C. M.; Martins, F. G.; Alvim-Ferraz, M. C. M.; Simoes, M., Recent developments on carbon capture and storage: An overview. *Chemical Engineering Research & Design* **2011,** *89* (9), 1446-1460.
4.   Shakerian, F.; Kim, K. H.; Szulejko, J. E.; Park, J. W., A comparative review between amines and ammonia as sorptive media for post-combustion CO_2 capture. *Applied Energy* **2015,** *148*, 10-22.
5.   Mumford, K. A.; Wu, Y.; Smith, K. H.; Stevens, G. W., Review of solvent based carbon-dioxide capture technologies. *Frontiers of Chemical Science and Engineering* **2015,** *9* (2), 125-141.
6.   Ben-Mansour, R.; Habib, M. A.; Bamidele, O. E.; Basha, M.; Qasem, N. A. A.; Peedikakkal, A.; Laoui, T.; Ali, M., Carbon capture by physical adsorption: Materials, experimental investigations and numerical modeling and simulations - A review. *Applied Energy* **2016,** *161*, 225-255.
7.   Kandiah, M.; Nilsen, M. H.; Usseglio, S.; Jakobsen, S.; Olsbye, U.; Tilset, M.; Larabi, C.; Quadrelli, E. A.; Bonino, F.; Lillerud, K. P., Synthesis and Stability of Tagged UiO-66 Zr-MOFs. *Chemistry of Materials* **2010,** *22* (24), 6632-6640.
8.   Madden, D. G.; Scott, H. S.; Kumar, A.; Chen, K. J.; Sanii, R.; Bajpai, A.; Lusi, M.; Curtin, T.; Perry, J. J.; Zaworotko, M. J., Flue-gas and direct-air capture of CO_2 by porous metal-organic materials. *Philosophical Transactions of the Royal Society a-Mathematical Physical and Engineering Sciences* **2017,** *375* (2084).

9.   Cavka, J. H.; Jakobsen, S.; Olsbye, U.; Guillou, N.; Lamberti, C.; Bordiga, S.; Lillerud, K. P., A new zirconium inorganic building brick forming metal organic frameworks with exceptional stability. *Journal of the American Chemical Society* **2008,** *130* (42), 13850-13851.

10.   Cmarik, G. E.; Kim, M.; Cohen, S. M.; Walton, K. S., Tuning the Adsorption Properties of UiO-66 via Ligand Functionalization. *Langmuir* **2012,** *28* (44), 15606-15613.

11.   Yang, W. B.; Davies, A. J.; Lin, X.; Suyetin, M.; Matsuda, R.; Blake, A. J.; Wilson, C.; Lewis, W.; Parker, J. E.; Tang, C. C.; George, M. W.; Hubberstey, P.; Kitagawa, S.; Sakamoto, H.; Bichoutskaia, E.; Champness, N. R.; Yang, S. H.; Schroder, M., Selective CO2 uptake and inverse CO_2/C_2H_2 selectivity in a dynamic bifunctional metal-organic framework. *Chemical Science* **2012,** *3* (10), 2993-2999.

12.   Bae, Y. S.; Farha, O. K.; Hupp, J. T.; Snurr, R. Q., Enhancement of CO_2/N_2 selectivity in a metal-organic framework by cavity modification. *Journal of Materials Chemistry* **2009,** *19* (15), 2131-2134.

13.   Deria, P.; Li, S.; Zhang, H. D.; Snurr, R. Q.; Hupp, J. T.; Farha, O. K., A MOF platform for incorporation of complementary organic motifs for CO_2 binding. *Chemical Communications* **2015,** *51* (62), 12478-12481.

14.   Vaidhyanathan, R.; Iremonger, S. S.; Dawson, K. W.; Shimizu, G. K. H., An amine-functionalized metal organic framework for preferential CO_2 adsorption at low pressures. *Chemical Communications* **2009,** (35), 5230-5232.

15.   Erucar, I.; Keskin, S., High CO_2 Selectivity of an Amine-Functionalized Metal Organic Framework in Adsorption-Based and Membrane-Based Gas Separations. *Industrial & Engineering Chemistry Research* **2013,** *52* (9), 3462-3472.

16.   Nugent, P.; Belmabkhout, Y.; Burd, S. D.; Cairns, A. J.; Luebke, R.; Forrest, K.; Pham, T.; Ma, S.; Space, B.; Wojtas, L.; Eddaoudi, M.; Zaworotko, M. J., Porous materials with optimal adsorption thermodynamics and kinetics for CO_2 separation. *Nature* **2013,** *495* (7439), 80-84.

17.   Vaidhyanathan, R.; Iremonger, S. S.; Shimizu, G. K. H.; Boyd, P. G.; Alavi, S.; Woo, T. K., Direct Observation and Quantification of CO_2 Binding Within an Amine-Functionalized Nanoporous Solid. *Science* **2010,** *330* (6004), 650-653.

18.   Vaidhyanathan, R.; Martens, I.; Lin, J. B.; Iremonger, S. S.; Shimizu, G. K. H., Larger pores via shorter pillars in flexible layer coordination networks. *Canadian Journal of Chemistry* **2016,** *94* (4), 449-452.

19.   Banerjee, A.; Nandi, S.; Nasa, P.; Vaidhyanathan, R., Enhancing the carbon capture capacities of a rigid ultra-microporous MOF through gate-opening at low CO_2 pressures assisted by swiveling oxalate pillars. *Chemical Communications* **2016,** *52* (9), 1851-1854.

20.   Shekhah, O.; Belmabkhout, Y.; Chen, Z.; Guillerm, V.; Cairns, A.; Adil, K.; Eddaoudi, M., Made-to-order metal-organic frameworks for trace carbon dioxide removal and air capture. *Nature Communications* **2014,** *5*.

21.   Gottlieb, H. E.; Kotlyar, V.; Nudelman, A., NMR chemical shifts of common laboratory solvents as trace impurities. *Journal of Organic Chemistry* **1997,** *62* (21), 7512-7515.

22.   Zhang, Y.; Lucier, B. E. G.; Huang, Y. N., Deducing CO_2 motion, adsorption locations and binding strengths in a flexible metal-organic framework without open metal sites. *Physical Chemistry Chemical Physics* **2016,** *18* (12), 8327-8341.

23.   Hayashi, S.; Hayamizu, K., CHEMICAL-SHIFT STANDARDS IN HIGH-RESOLUTION SOLID-STATE NMR (1) C-13, SI-29 AND H-1 NUCLEI. *Bulletin of the Chemical Society of Japan* **1991,** *64* (2), 685-687.

24.   Pretsch, E.; Clerc, T.; Seibl, J.; Simon, W., Tables of Spectral Data for Structure Determination of Organic Compounds. 2 ed.; Springer-Verlag: Berlin, Heidelberg, 1989; p 416.

25.   Eichele, R. E. W. K. *WSolids1*, University of Tübingen: Germany, 2001.

26.   Vold, R. L.; Hoatson, G. L., Effects of jump dynamics on solid state nuclear magnetic resonance line shapes and spin relaxation times. *Journal of Magnetic Resonance* **2009,** *198* (1), 57-72.

27.   Beeler, A. J.; Orendt, A. M.; Grant, D. M.; Cutts, P. W.; Michl, J.; Zilm, K. W.; Downing, J. W.; Facelli, J. C.; Schindler, M. S.; Kutzelnigg, W., LOW-TEMPERATURE C-13 MAGNETIC-RESONANCE IN SOLIDS .3. LINEAR AND PSEUDOLINEAR MOLECULES. *Journal of the American Chemical Society* **1984,** *106* (25), 7672-7676.

28.   Clark, S. J.; Segall, M. D.; Pickard, C. J.; Hasnip, P. J.; Probert, M. J.; Refson, K.; Payne, M. C., First principles methods using CASTEP. *Zeitschrift Fur Kristallographie* **2005,** *220* (5-6), 567-570.

29.   Profeta, M.; Mauri, F.; Pickard, C. J., Accurate first principles prediction of O-17 NMR parameters in SiO_2: Assignment of the zeolite ferrierite spectrum. *Journal of the American Chemical Society* **2003,** *125* (2), 541-548.

30.   Chen, S. S.; Lucier, B. E. G.; Boyle, P. D.; Huang, Y. N., Understanding The Fascinating Origins of CO_2 Adsorption and Dynamics in MOFs. *Chemistry of Materials* **2016,** *28* (16), 5829-5846.

31.   Wang, W. D.; Lucier, B. E. G.; Terskikh, V. V.; Wang, W.; Huang, Y. N., Wobbling and Hopping: Studying Dynamics of CO_2 Adsorbed in Metal-Organic Frameworks via O-17 Solid-State NMR. *Journal of Physical Chemistry Letters* **2014,** *5* (19), 3360-3365.

32.   Kong, X. Q.; Scott, E.; Ding, W.; Mason, J. A.; Long, J. R.; Reimer, J. A., CO_2 Dynamics in a Metal-Organic Framework with Open Metal Sites. *Journal of the American Chemical Society* **2012,** *134* (35), 14341-14344.

33.   Pouchert, C. J.; Behnke, J., *The Aldrich library of ^{13}C and ^1H FT NMR spectra*. 1 ed.; Aldrich Chemical Co.: Milwaukee, USA, 1993; Vol. 1, p 4300.

34.   Banfi, D.; Patiny, L., www.nmrdb.org: Resurrecting and processing NMR spectra on-line. *Chimia* **2008,** *62* (4), 280-281.

35.   Gullion, T., Introduction to rotational-echo, double-resonance NMR. *Concepts in Magnetic Resonance* **1998,** *10* (5), 277-289.

36.   Li, S. H.; Su, Y. C.; Hong, M., Intramolecular H-1-C-13 distance measurement in uniformly C-13, N-15 labeled peptides by solid-state NMR. *Solid State Nuclear Magnetic Resonance* **2012,** *45-46*, 51-58.

37.   Bovey, F. A., *NMR Data Tables for Organic Compounds*. Interscience Publishers: New York, USA, 1967.

38.   Huang, Y. N.; Sutrisno, A., Recent Advances in Solid-State Zn-67 NMR Studies: From Nanoparticles to Biological Systems. *Annual Reports on Nmr Spectroscopy, Vol 81* **2014,** *81*, 1-46.

3.6   Appendix

Table S3.1: Acquisition parameters for VT static ^{13}C SSNMR of $^{13}CO_2$ loaded ZnAtzOx(H₂O) are shown below.

Sample	Temperature (K)	Acquisitions	Decoupled Nucleus	Pulse Delay (s)	90° Pulse Width (μs)
ZnAtzOx(H₂O), CO₂ Loaded	393 K	801	^{1}H	6	2.67
	373 K	824	^{1}H	6	2.67
	353 K	838	^{1}H	6	2.67
	333 K	915	^{1}H	6	2.67
	313 K	800	^{1}H	6	2.67
	293 K	3394	^{1}H	20	2.67
	273 K	826	^{1}H	6	2.67
	253 K	812	^{1}H	6	2.67
	233 K	800	^{1}H	6	2.67
	213 K	803	^{1}H	6	2.67
	193 K	801	^{1}H	6	2.67
	173 K	816	^{1}H	6	2.67
	153 K	827	^{1}H	6	2.67

Table S3.2: Acquisition parameters for MAS ^{13}C direct-excitation and CP SSNMR of $^{13}CO_2$ loaded ZnAtzOx(H₂O) are shown below.

Spin Rate (Hz)	CP nuclei	Acquisitions	Pulse Delay (s)	90° Pulse Width (μs)
12 500	None	400	5	4.00 (^{13}C)
2800	None	400	5	4.00 (^{13}C)
12 500	^{1}H-^{13}C	360	10	4.25 (^{1}H)

Table S3.3: Acquisition parameters for ^1H-^{13}C REDOR SSNMR of ZnAtzOx(H$_2$O) are shown below.

Sample	Spinning Speed (Hz)	Acquisitions	Pulse Delay (s)	90° Pulse ^{13}C Width (µs)	90° Pulse ^1H Width (µs)
ZnAtzOx(H$_2$O), CO$_2$ Loaded	10 000	56	30	4.00	4.70
ZnAtzOx(H$_2$O)	15 000	1700	2	4.00	4.88

Table S3.4: Acquisition parameters for ^1H-^{13}C HETCOR SSNMR of ZnAtzOx(H$_2$O) are shown below.

Sample	Spinning Speed (Hz)	Acquisitions	Pulse Delay (s)	Contact Time (µs)
ZnAtzOx(H$_2$O), CO$_2$ Loaded	18 000	512	5	500
ZnAtzOx(H$_2$O)	18 000	512	5	500

Chapter 4 : Studying Water Adsorption within the Ultramicroporous SIFSIX-3-Zn and ZnAtzOx frameworks, Preliminary Results

4.1   Introduction

One of the biggest challenges in using physisorbent materials to capture CO_2 is their sensitivity to moisture in gaseous mixtures. While open metal sites (OMSs) are highly selective adsorption sites for CO_2 against the adsorption of non polar gases such as H_2, N_2 and CH_4, OMSs are also often promising adsorption sites for gaseous H_2O.[1] In addition to competing for adsorption sites, H_2O can block diffusion pathways within the pores[2] or even cause a complete collapse of the framework.[1] This collapse can occur through two primary mechanisms: ligand displacement or hydrolysis.[3, 4] As such the presence of water in post-combustion flue gas is a significant barrier for the implementation of physisorbent materials in carbon capture applications.

The water content of flue-gas varies, though it has been previously found to be about 5% to 7% by volume from a coal burning power plant.[5] Completely dehydrating the gas before CO_2 capture would significantly increase the cost of implementation of carbon capture technologies.[2] The presence of moisture is also a concern in shifted gas, for pre-combustion capture applications, or in air, for direct air capture applications.[6] This means development of solid CO_2 adsorbing materials which functions in the presence of moisture, and understanding how frameworks interact with moisture, is a key area of metal-organic framework (MOF) design.

For example, Mg-MOF-74,[7] considered one of the most promising MOFs for CO_2 adsorption, displays CO_2 uptake behaviour that is strongly inhibited by the presence of moisture.[8] The water in this case adsorbs most strongly to the OMS within the MOF, the same adsorption site used by CO_2. Temperature programmed desorption experiments found that in moist simulated flue gas, the measured CO_2 desorbed per g by Mg-MOF-74 was only a quarter of that measured in dry

simulated flue gas, with almost half of desorbed analyte by mass being H_2O.[9] Keeping the MOF in accelerated storage conditions for two weeks resulted in its maximum CO_2 uptake dropping by two thirds due to the presence of moisture.[9]
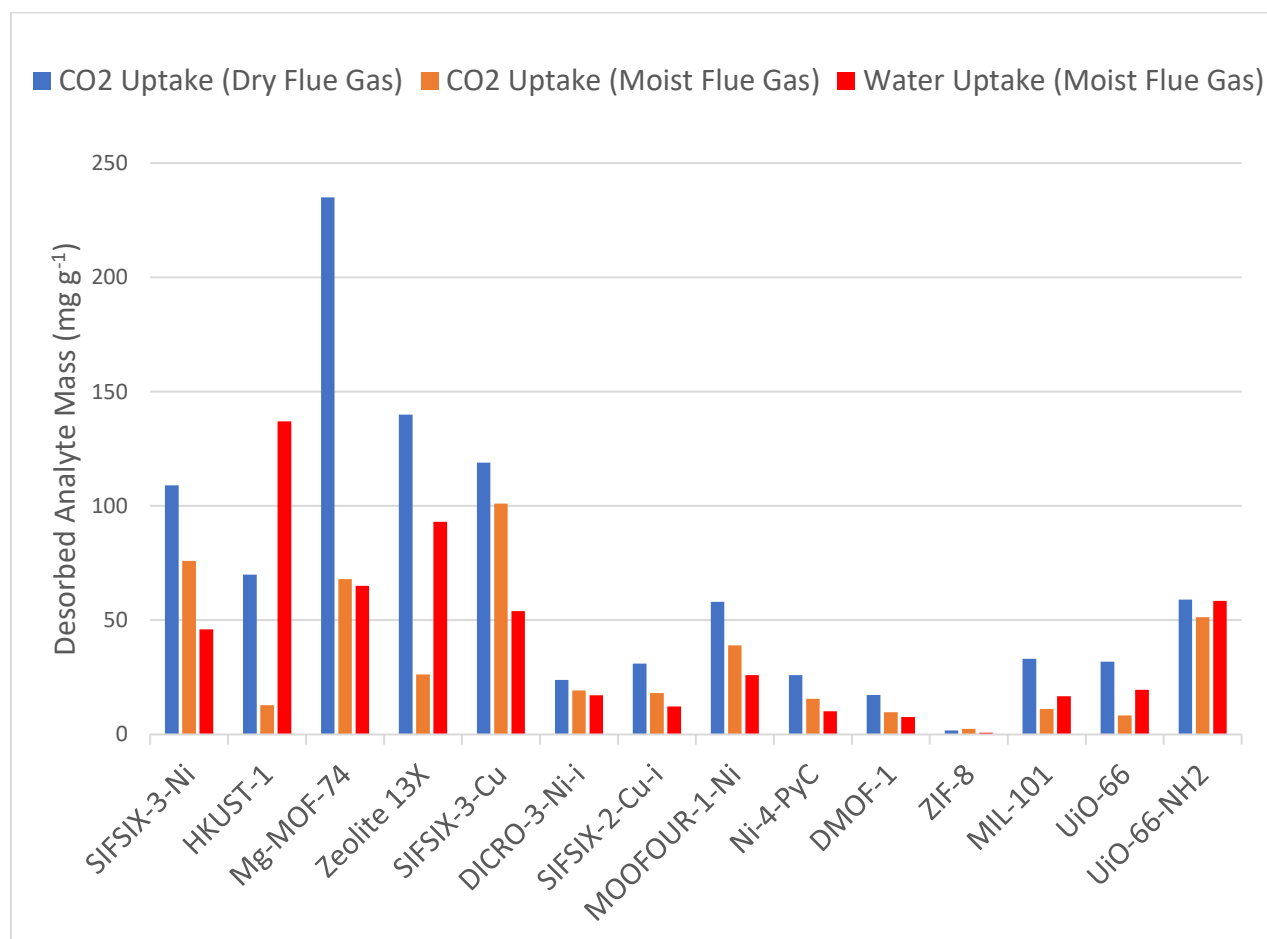
Figure 4.1: The masses of desorbed analyte per mass of adsorbent, collected from physisorbent materials exposed to simulated moist and simulated dry flue gas are depicted on this graph. The analytes, H_2O and CO_2, are measured in mg of analyte per g of sorbent. While Mg-MOF-74 adsorbed the most CO_2 in dry flue gas, it was overtaken by SIFSIX-3-Ni and SIFSIX-3-Cu when moisture was introduced. This data was obtained from refences 9 and 10.

Similar temperature programmed desorption experiments indicated there was a notable drop in CO_2 desorbed by other porous frameworks, as shown in Figure 4.1.[9, 10] Frameworks including SIFSIX-3-Ni, HKUST-1, Zeolite 13X, SIFSIX-3-Cu, MIL-101 and UiO-66 all desorbed between 15% and 82% less CO_2 per g in experiments with moist simulated flue gas compared to dry simulated flue gas. The ZIF-8 framework proved to be unaffected by the presence of moisture, but possessed an exceptionally low maximum CO_2 uptake. SIFSIX-3-Ni and SIFSIX-3-Cu possessed the highest CO_2 uptake capacity in moist simulated flue gas of all tested solid physisorbents, due to their highly selective ultramicropores.[11-13] SIFSIX-3-Ni also had a negligible drop in surface area and maximum CO_2 uptake after being left in accelerated storage conditions for two weeks.[9]

UiO-66-NH_2 was another tested MOF that showed only a small drop in CO_2 desorbed when exposed to moist flue gas, despite adsorbing H_2O. Amine functionalized MOFs are known to possess an increased affinity for CO_2 while still being more easily regenerated than chemisorbent materials.[10, 14] The selectivity of highly selective ultramicropores and amine groups for CO_2 adsorption over water adsorption makes understanding the guest-host interactions involved desirable.

A better understanding of the effects of water adsorption on CO_2 adsorption can be obtained using solid-state nuclear magnetic resonance spectroscopy (SSNMR). The motions of water molecules within M-MOF-74 materials have already been studied using these techniques.[15] It was found that within Mg-MOF-74, D_2O was strongly adsorbed at OMSs, at temperatures up to 293 K, where it exhibited π flip-flop motions in the fast-motion regime. At lower temperatures, the motional rate was found to slow to 1.5×10^6 Hz.

Very different behaviour was observed in the case of Zn-MOF-74. The spectra consisted of a broad pattern similar to what was observed in Mg-MOF-74, as well as a narrow resonance suggesting the presence of weakly coordinated D_2O molecules. This supported additional TGA measurements and calculated hydration energies suggesting the water was more weakly coordinated within Zn-MOF-74 than Mg-MOF-74.[16, 17]

Though SIFSIX-3-Ni and SIFSIX-3-Cu have both been reported as being highly selective for CO_2 in the presence of water, SIFSIX-3-Zn exhibits very different behaviour. Initial breakthrough experiments suggested the presence of moisture had little effect on the selectivity for CO_2 of the framework.[11] However, multicomponent adsorption experiments conducted later suggested a much more significant change in CO_2 uptake of SIFSIX-3-Zn due the presence of water.[18] Repeated experiments obtained multiple values for the CO_2 uptake capacity in the presence of moisture, with the uptake dropping as low as 0.0 mmol g^{-1}. This was determined to be due to a previously reported phase transition which occurs within the framework when exposed to increasing H_2O partial pressures.[11]

The factors and mechanism behind this phase change are not well understood, though a recent report on water vapor sorption in SIFSIX materials discussed the phase change in SIFSIX-3-Ni.[19] Powder X-ray diffraction (PXRD) was used to determine the structure of SIFSIX-3-Ni after a humidity-induced phase change. It was found that water would cleave the bond between the nickel cation and SiF_6^{2-} anion, in favour of the formation of an aqua complex. It is likely a similar interaction occurs in SIFSIX-3-Zn. The study also found that SIFSIX materials with larger pores, such as SIFSIX-14-Cu-I, were more susceptible to hydrolysis than the structures with smaller pores, such as SIFSIX-3-M materials. A better understanding of H_2O adsorption within SIFSIX-

3-M materials through SSNMR studies, as well as H_2O and CO_2 coadsorption, will help shed light on the effects of H_2O on ultramicroporous physisorbent structures.

Given this unusual behaviour compared to more traditional physisorbents such as Mg-MOF-74, it is of interest to study water adsorption in ultramicroporous materials to better understand the effects of water on MOFs. SIFSIX-3-Zn[11, 20] was studied for it's similarities and differences compared to other SIFSIX-3-M materials, in both structure and CO_2 adsorption behaviour. The lack of a paramagnetic metal centre means it can be more easily studied through SSNMR techniques, as unpaired electrons give rise to strong local magnetic fields that complicate structural analyses.[21]

ZnAtzOx(H_2O) was also studied due to its similarly ultramicroporous nature, and its known stability when the material is occupied by water molecules.[22] This structure was first reported in 2016 and has not had it's water adsorption behaviour studied previously, but it possesses a known strong selectivity for CO_2 adsorption over other gases, high CO_2 uptake, and is known to possess H_2O in its pores in the as made phase. Additionally, ZnAtzOx(H_2O) contains amine groups thought to promote CO_2 adsorption, much like the UiO-66-NH_2 MOF which was found to perform well in the presence of moisture.[10] This amine functionalization combined with ultramicropores and high CO_2 uptake make ZnAtzOx(H_2O) an promising porous structure. Studying water adsorption in this structure will offer insight into how the framework interacts with guest molecules within its pores. The results of these experiments are preliminary; further research needs to be conducted before publication can be considered, to develop a more comprehensive understanding of the systems and to ensure the accuracy of conclusions.

4.2   Experimental

4.2.1   Synthesis of SIFSIX-3-Zn and ZnAtzOx(H$_2$O)

SIFSIX-3-Zn and ZnAtzOx(H$_2$O) were synthesized solvothermally using methods described in the literature.[20, 22]

A typical SIFSIX-3-Zn synthesis is as follows: a 10 mL solution of pyrazine (0.48 g, 6 mmol, Alfa Aesar, 98%) in methanol was decanted into a separate 10 mL solution of zinc hexafluorosilicate hydrate (0.62 g, 3 mmol, Sigma-Aldrich, 99%) in methanol. The resulting 20 mL solution was left at room temperature for 3 days, after which yellow crystals were collected and dried at 90 °C in air for three hours. Prior to activation and guest loading, SIFSIX-3-Zn samples were solvent exchanged in a methanol solution for three days, as done in the literature.[11] The methanol solution was replaced daily.

A typical synthesis of ZnAtzOx(H$_2$O) is as follows: oxalic acid (0.09 g, 1 mmol, Sigma-Aldrich, 98%), 3-amino-1,2,4-triazole (0.42 g, 5 mmol, Sigma-Aldrich, ≥95%) and zinc carbonate basic (0.11g, 1 mmol, Alfa Aesar, 97%) were added to a 3 mL butanol and 3 mL water solvent mixture in a Teflon-lined stainless steel autoclave. The solution was stirred for 30 min at room temperature, and then heated at 180 °C for two days. Upon cooling, a colourless crystalline product was collected using vacuum filtration, washed with methanol and water, and dried at 90 °C in air for three hours.

4.2.2   Powder X-ray diffraction

The identities and purities of the product were confirmed using PXRD. Patterns were recorded on an Inel CPS powder diffractometer operating with Cu Kα radiation (λ = 1.5418 Å). Experimental and simulated PXRD patterns are depicted in Figure 4.2. The experimental PXRD patterns are consistent with patterns calculated from reported crystal structures,[11, 22] and are also

consistent with previously determined experimental PXRD patterns of the materials.[11, 22] After synthesis, the PXRD patterns were used to confirm phase purity of the samples. The PXRD pattern of H_2O loaded SIFSIX-3-Zn was used to confirm the guest induced phase change at a given loading level. At a ratio of 0.8 H_2O to Zn there was no observed phase change in the PXRD pattern. At a ratio of 2.5 H_2O to Zn a phase change was observed. Very slight impurities appear to arise in the ZnAtzOx(H_2O) PXRD pattern after H_2O loading, likely due to a slight framework decomposition after the evacuation and loading process, however this is not expected to affect the results of SSNMR experiments.
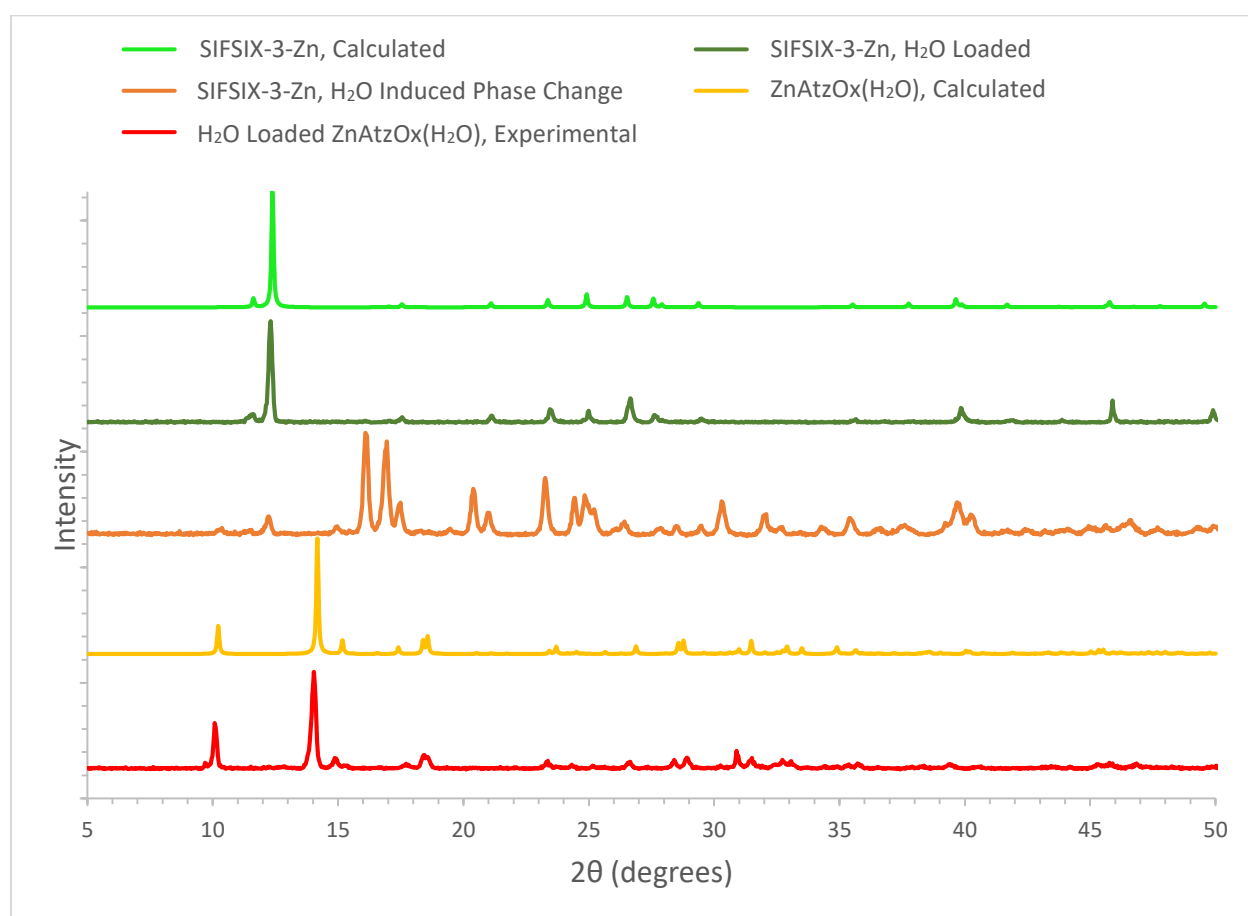
Figure 4.2: The experimental and calculated SIFSIX-3-Zn and ZnAtzOx(H₂O) PXRD patterns are depicted above.

4.2.3 Sample activation, gas loading, and thermal gravimetric analysis

The activation process removes solvent molecules from the framework pores. A Schlenk line was used for activation. Samples were placed into the bottom of an L-shaped glass tube, and a thin layer of glass wool was used to secure the sample in place. SIFSIX-3-Zn samples were activated under dynamic vacuum (< 1 mbar) at 80 ± 10 °C for twenty-four hours. The ZnAtzOx samples were activated under dynamic vacuum at 150 ± 10 °C for twelve hours. D_2O or $^{13}CO_2$ gas was then released into the line, which has a measured total volume of 82.7 mL, as the gas pressure was monitored simultaneously. Samples were then loaded with a known quantity of D_2O (Cambridge Isotope Laboratories, Inc., 99.9%) or CO_2 while the bottom of the L-shaped tube was immersed in liquid nitrogen to trap guests within the MOF. The loaded MOF sample within the glass tube was then flame sealed off from the Schlenk line prior to SSNMR experiments.

Due to the condensation of D_2O vapour within the Schlenk line, it is difficult to gauge the loading level with certainty based on changes in pressure. Thermal gravimetric analysis (TGA) was used to determine the loading level of D_2O or H_2O within framework samples. The TGA curves for samples were measured under dry N_2 flow using a Mettler Toledo TGA/SDTA851e instrument. For each TGA experiment, 5 to 10 mg of the sample was placed within a ceramic crucible. A temperature range between 25 °C and 800 °C and a heating rate of 10 °C/min were utilized. The resulting TGA curves can be seen in Figure 4.3.

TGA experiments on H_2O loaded SIFSIX-3-Zn revealed a weight loss of 4% between 50 to 150 °C, corresponding to an H_2O loading of 0.8 mols of H_2O per mol of Zn in SIFSIX-3-Zn. Samples at this loading level were used for SSNMR experiments.

TGA experiments on H_2O loaded ZnAtzOx(H_2O) revealed a weight loss of 7% between 50 to 150 °C, corresponding to an H_2O loading of 0.7 mols of H_2O per mol of Zn in ZnAtzOx(H_2O). Samples at this loading level were used for SSNMR experiments.

A 0.25 molar ratio of CO_2 to Zn^{2+} was used when SIFSIX-3-Zn and ZnAtzOx(H_2O) samples with carbon dioxide. [13]C labelled CO_2 (Sigma-Aldrich, 99 atom % [13]C, <3 atom % [18]O) was used to load samples for ^{13}C SSNMR experiments. For coadsorption experiments, samples were first loaded with [13]CO$_2$ and then exposed afterwards to D_2O.
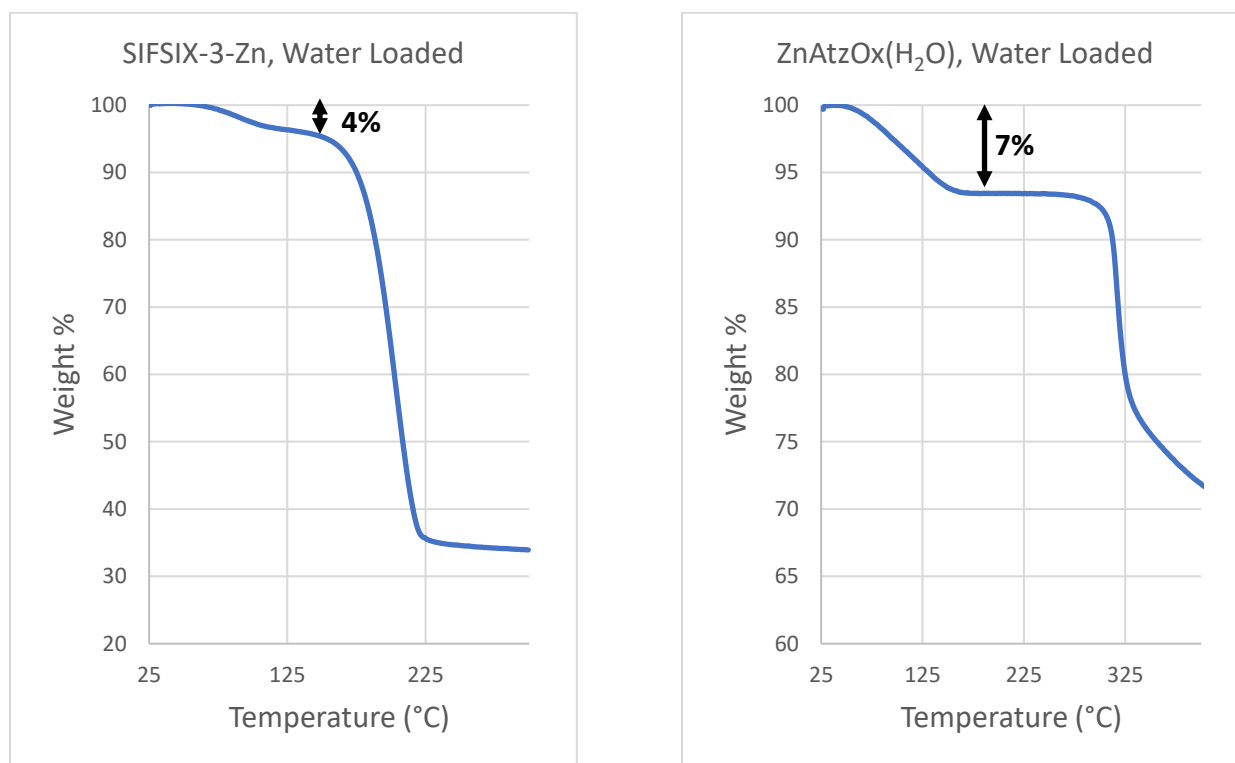
Figure 4.3: The experimental TGA curves for water loaded SIFSIX-3-Zn and ZnAtzOx(H₂O) samples used in SSNMR experiments are shown above.

4.2.4   SSNMR experiments

^{2}H and ^{13}C SSNMR experiments were performed at the University of Western Ontario in London, Ontario, using a Varian Infinity Plus SSNMR spectrometer equipped with an Oxford 9.4 T wide-bore magnet. All experiments were conducted with a 5 mm HX Varian/Chemagnetics probe.

^{2}H experiments referenced using liquid D_2O as a secondary standard at 4.8 ppm, relative to $(CD_3)_4Si$.[23] ^{2}H spectra were collected using a quadrupole echo pulse sequence. ^{13}C spectra were referenced to tetramethylsilane (TMS) using the methylene carbon in ethanol as a secondary reference, which has a chemical shift (CS) of 58.05 ppm.[24] All direct-excitation ^{13}C SSNMR experiments were performed using the DEPTH-echo pulse sequence to minimize the probe background signal.[25] All experiments were performed using a 30 kHz ^{1}H decoupling field.

Additional acquisition parameters for specific spectra are listed in Tables S4.1, S4.2 and S4.3.

4.2.5   Spectral simulations

The WSolids[26] computer software was used to analytically simulate all static ^{2}H and ^{13}C SSNMR spectra and obtain apparent powder pattern parameters. The ^{2}H patterns are dominated by the quadrupolar interaction (QI), while the ^{13}C patterns are broadened and dominated by the CS anisotropy (CSA). WSolids calculated the powder pattern of a static powder sample showing effects of the QI or CSA. ^{2}H SSNMR patterns were calculated through inputting the electric field gradient (EFG) parameters (C_Q and η_Q). ^{13}C SSNMR patterns were calculated through inputting the orthogonal components of the CS tensor (δ_{11}, δ_{22} and δ_{33}). By comparing the known experimental powder patterns to a calculated pattern, the experimental powder pattern parameters

for ^{13}C (δ_{iso}, Ω and κ) and ^{2}H (C_Q and η_Q) can be determined. The errors in pattern parameters were estimated by bidirectional variation of the parameters from the best-fit value.

The EXPRESS[27] computer software was used to simulate the effects of motion on the ^{2}H and ^{13}C SSNMR powder patterns. EXPRESS describes motion in terms of discrete (Markovian) jumps at specified rates between sites. A motional model can then be described by the number, orientation, and populations of sites, as well as the nature of the connections and rates of jumps. The motion results in a predictable averaging of CS tensor components. For ^{2}H patterns, given the known D – O – D bond angle of 104.5°,[28] the inputted C_Q value could be varied to produce the motionally averaged ^{2}H line shape that matches the experimentally observed ^{2}H NMR spectrum. The static η_Q value is assumed to be zero, due to the axial symmetry of the D_2O molecule. In the case of ^{13}C patterns, given the known powder pattern parameters of solid CO_2 ($\delta_{iso} = 126$ ppm, $\Omega = 335$ ppm, and $\kappa = 1$),[29] and assuming a linear geometry for the CO_2 molecule. powder patterns produced by specific types and rates of motion were calculated. All patterns were calculated across 4096 powder increments using the ZCW powder averaging procedure and compared to the experimental powder patterns.

4.3   Results and Discussion

4.3.1   Static variable temperature ^{2}H SSNMR of D_2O loaded SIFSIX-3-Zn

As the presence of water is known to dramatically affect CO_2 adsorption behaviour, ^{2}H SSNMR was used to understand the behaviour of water within the SIFSIX-3-Zn framework. The SSNMR pattern of ^{2}H nuclei are dominated by the QI, described by the quadrupolar coupling constant C_Q, and asymmetry parameter η_Q. The EFGs of the D – O bonds within D_2O are approximately axially symmetric, giving the η_Q a value of zero. The C_Q value meanwhile is

characteristic of the chemical environment, and the line shape is characteristic of the types and rates of motion.
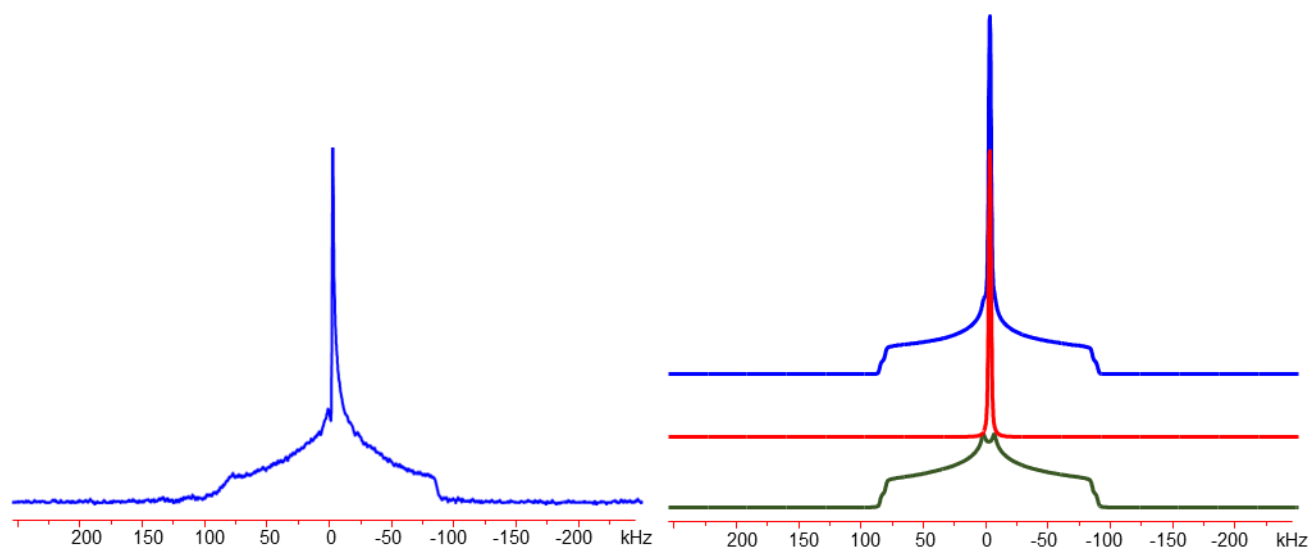
Figure 4.4: The experimental (left) and simulated (right) ^2H spectra of D$_2$O loaded SIFSIX-3-Zn at 393 K is shown above. The spectra were collected using 1800 scans and a 1 s recycle delay. The simulated narrow and broad components are shown in red and green respectively.

At 293 K, the spectrum exhibits a broad pattern with an apparent C$_Q$ of 120(10) kHz and an η$_Q$ of 0.90(5). Additionally, there is a narrow component with a width of approximately 5(5) kHz. This narrow component is likely due to disordered D$_2$O within the pores only weakly interacting with the framework. The combination of both broad and narrow components can be seen in Figure 4.4. ^2H static spectra of D$_2$O loaded SIFSIX-3-Zn across all experimental temperatures are shown in Figure 4.5.

Figure 4.5: The experimental (left) and simulated (right) ^2H spectra of D₂O loaded SIFSIX-3-Zn are shown above at temperatures ranging from 393 K to 153 K. The spectra were collected using between 1500 and 4000 scans and a 1 s recycle delay, except at 293 K where 30 000 scans and a 2 s recycle delay was used. The motional rate of the D₂O molecule's π flip-flop is listed on the simulated spectra.

At a temperature of 393 K, the apparent C_Q of the broad component drops to only 115(5) kHz, though the intensity of the narrow component is significantly greater. At 393 K, the narrow component begins to dominate the pattern, as shown in Figure 4.4. At 153 K, the broad component has an apparent C_Q of 120(10) kHz, and the narrow component appears to have disappeared. The existence of the broad powder pattern across a wide array of temperatures is suggestive of strong interactions between the guest D_2O and the framework, though at sufficiently high temperatures the broad pattern can be expected to disappear as D_2O is evacuated completely.

Using EXPRESS,[27] these powder patterns can be accurately simulated and the static C_Q value obtained for the D – O bond. At 293 K, the motions are simulated as a π flip-flop of D_2O about its symmetry axis, at a rate of 1×10^7 Hz in the intermediate motion regime. This motion is illustrated in Figure 4.6. Using a D – O – D angle of 104.5°, the pattern was reproduced using a static C_Q value of 250 kHz.
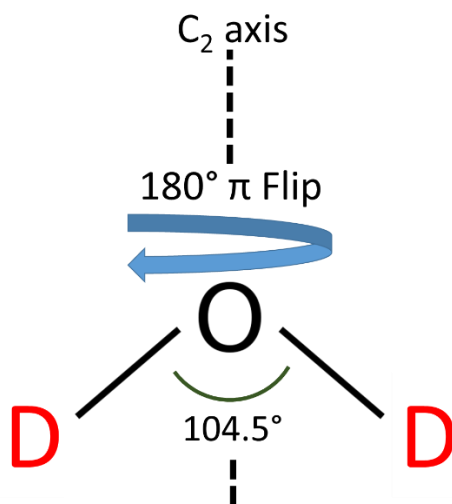
Figure 4.6: The π flipping motion of a D_2O molecule is illustrated above. The ^2H SSNMR spectra of D_2O loaded SIFSIX-3-Zn suggests that the molecules undergo this motion in the fast and intermediate motional regimes, with the exact motional rate depending on the temperature.

The C_Q value for D_2O depends on the EFG at the deuteron position. It's value reflects different binding and different deuteron positions.[30] A static C_Q value of 250 kHz is characteristic of hydrogen bonded molecules in crystalline hydrates.[31] At temperatures of 313 K and above, the rate of motion exceeds 2×10^7 Hz, in the fast motion regime. At a temperature of 153 K, the motional rate was found to drop to 2×10^6 Hz.

It is observed that the D_2O is adsorbed strongly within the SIFSIX-3-Zn framework, exhibiting motions with a low degree of temperature dependence. A single D_2O adsorption site observed in the SSNMR pattern, with a high C_Q value. The apparent C_Q value does not change as the temperature increases, though the broad pattern begins to become dominated by a narrow component. The lack of any obvious motions aside from a π flip-flop of the molecule, and the existence of adsorbed D_2O at temperatures as high as 393 K, is evidence of the strength of the interactions between the D_2O and SIFSIX-3-Zn, comparable to the interactions observed between CO_2 and SIFSIX-3-Zn.

4.3.2 Static ^{67}Zn SSNMR of H_2O saturated SIFSIX-3-Zn

When saturated with moisture, a phase change occurs within SIFSIX-3-Zn, as confirmed by PXRD. This is known to cause a loss of porosity and CO_2 uptake within the framework, likely due to the cleaving of the Zn – F bond and the formation of an aqua complex.[18, 19] It is therefore expected that upon saturation with H_2O, the local Zn environment will change. The spectrum resulting from high field ^{67}Zn SSNMR on water saturated SIFSIX-3-Zn is shown in Figure 4.7. This provides insight into the changes in chemical environment SIFSIX-3-Zn undergoes when exposed to moisture, which are known to affect the framework's CO_2 uptake behaviour.

The ^{67}Zn powder pattern is significantly different from the patterns previously obtained for the as made, activated and CO_2 loaded phases of SIFSIX-3-Zn. The pattern is characterized by a narrow centre component possessing a Lorentzian line width of approximately 7 kHz.

The ^{67}Zn environment of SIFSIX-3-Zn after undergoing a moisture-induced phase change is dramatically different from the ^{67}Zn environment prior to the phase change. The water molecule directly affects the ^{67}Zn environment, significantly more than methanol or CO_2 molecules when occupying of the pores.
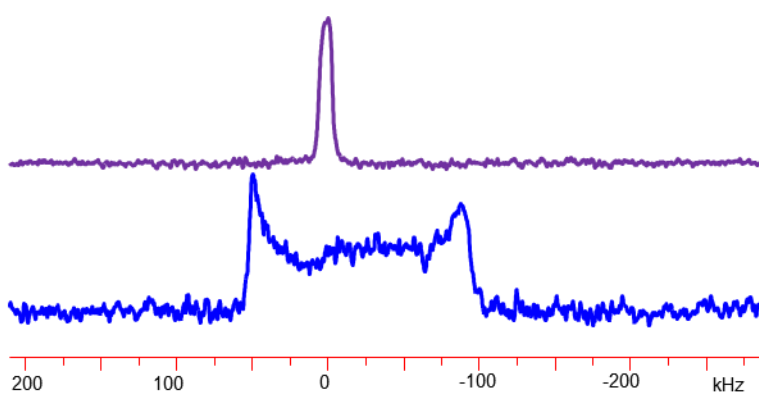
Figure 4.7: The H_2O saturated (purple) and as made (blue) ^{67}Zn spectra of SIFSIX-3-Zn are shown above. The spectra were collected using 256 000 scans and a 0.25 s recycle delay.

4.3.3   Static variable temperature ^2H SSNMR of D_2O loaded ZnAtzOx(H_2O)

^2H SSNMR spectra of ZnAtzOx(H_2O) loaded with D_2O produced more complex powder patterns than the equivalent SIFSIX-3-Zn spectra, with evidence of two distinct D_2O adsorption sites. These spectra are depicted in Figure 4.8. At 293 K, the sites have apparent C_Q values of 120(5) kHz and 60(5) kHz, and apparent η_Q values of 0.50(5) and 0.8(1).
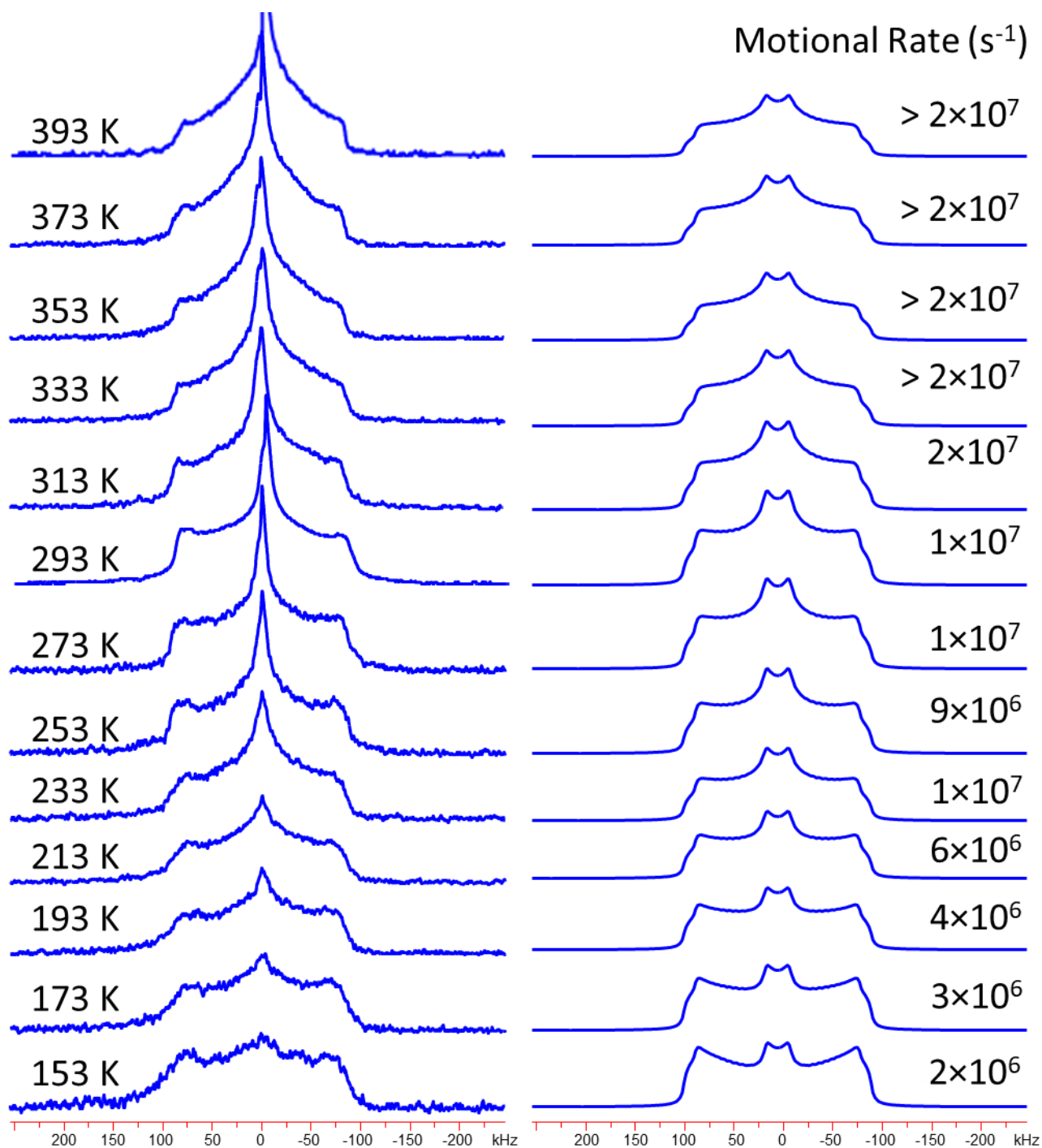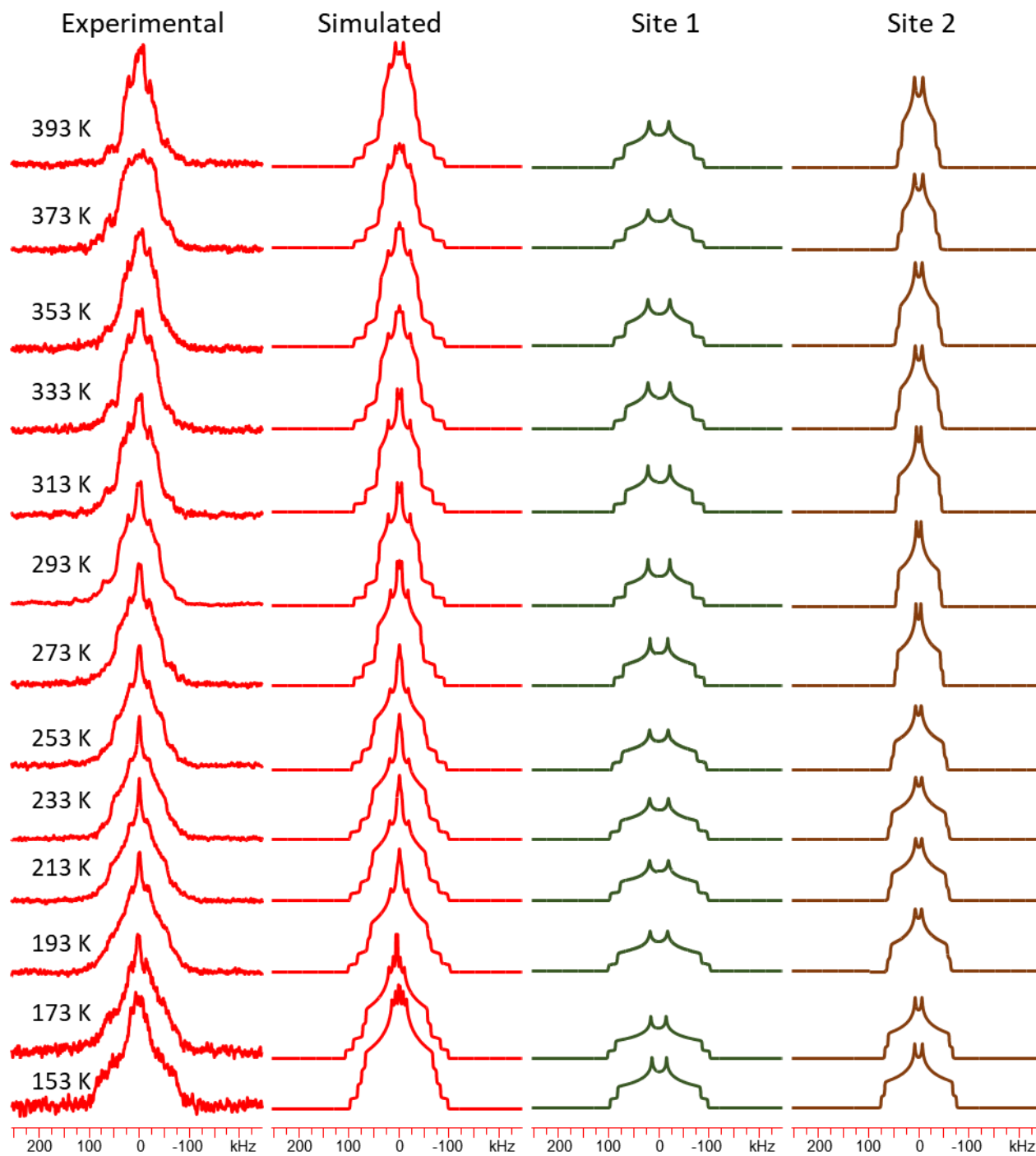
Figure 4.8: The experimental and simulated ^2H spectra of D_2O loaded $ZnAtzOx(H_2O)$ are shown above at temperatures ranging from 393 K to 153 K. The spectra were collected using between 3000 and 4000 scans and a 1 s recycle delay, except at 293 K where 30 000 scans and a 2 s recycle delay was used.
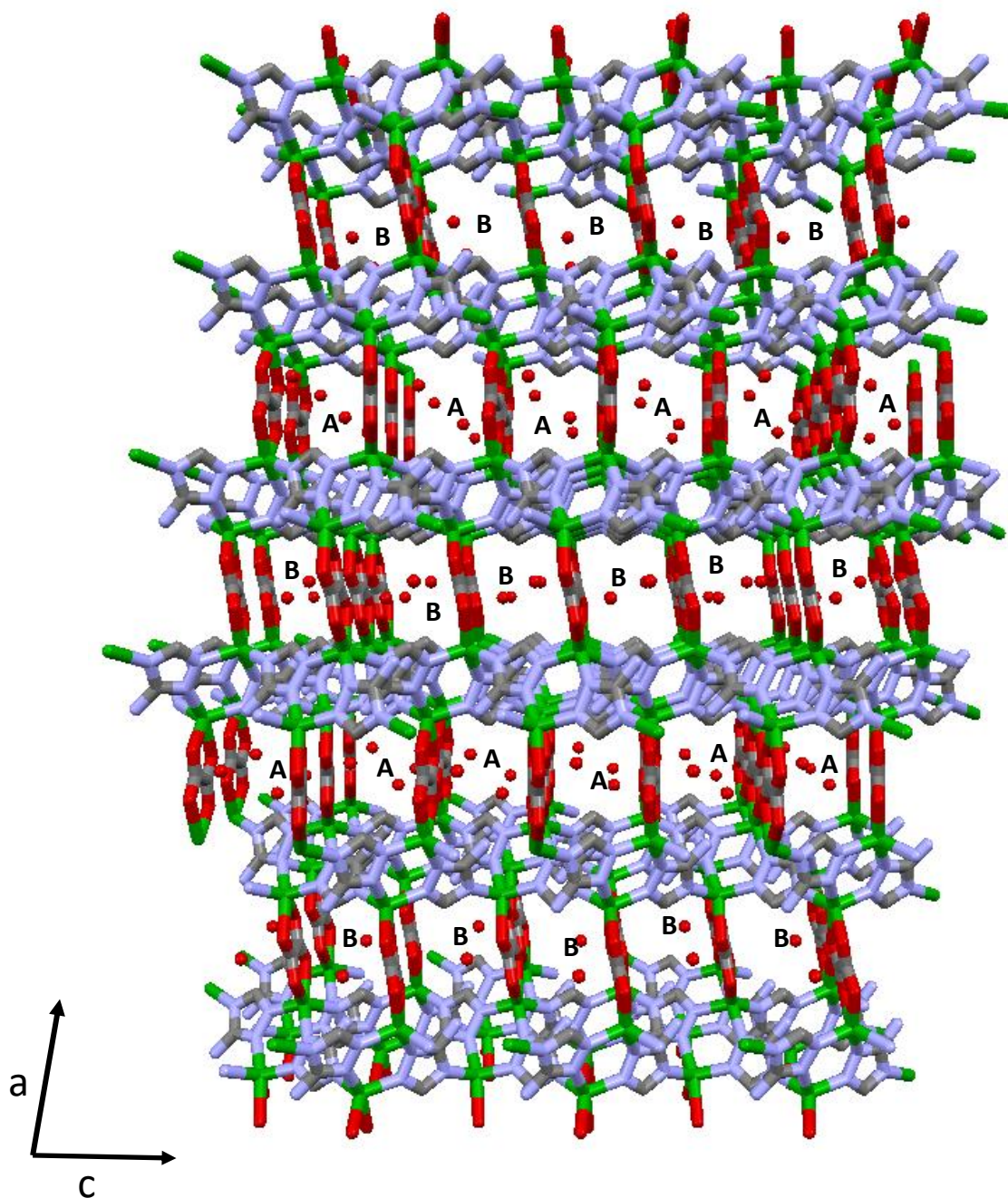
Figure 4.9: The arrangement of the literature reported H₂O sites (A and B) in ZnAtzOx(H₂O) are shown along the b-axis. The arrows and captions indicate distances to the nearest oxalate, amine and C-H groups. Site A is slightly more proximate (0.05 to 0.45 Å) to the groups of interest. The overall locations of the sites are similar.

As the temperature increases, these parameters are unchanged within error. At low temperatures, the apparent C_Q values increase, to 150(20) and 110(20) kHz at 153 K. The changes in apparent C_Q and η_Q are detailed in Table 4.1. There is also a slight narrow intensity from mobile D_2O present at temperatures of 193 K and above, however its intensity does not appear to vary significantly with temperature.

Table 4.1: The observed ^2H QI parameters of H_2O-loaded ZnAtzOx(H_2O) are listed below. These parameters were obtained from analytical simulations of static ^2H SSNMR spectra using WSolids.[26]

Temperature (K)	C_Q, Site 1 (kHz)	η_Q Site 1	C_Q, Site 2 (kHz)	η_Q Site 2
393 K	120 (5)	0.55 (5)	55 (5)	0.6 (1)
373 K	120 (5)	0.50 (5)	55 (5)	0.6 (1)
353 K	120 (5)	0.50 (5)	60 (5)	0.7 (1)
333 K	120 (5)	0.50 (5)	60 (5)	0.7 (1)
313 K	120 (5)	0.50 (5)	60 (5)	0.8 (1)
293 K	120 (5)	0.60 (5)	60 (5)	0.8 (1)
273 K	125 (5)	0.60 (5)	65 (5)	0.8 (1)
253 K	130 (5)	0.60 (5)	70 (5)	0.8 (1)
233 K	130 (5)	0.60 (5)	80 (5)	0.8 (1)
213 K	130 (5)	0.60 (5)	80 (5)	0.8 (1)
193 K	135 (5)	0.65 (5)	85 (5)	0.8 (1)
173 K	150 (20)	0.7 (2)	100 (20)	0.9 (1)
153 K	150 (20)	0.7 (2)	110 (20)	0.8 (2)

Simulations performed using EXPRESS[27] were inconclusive in describing the motions of D_2O at each site, due to the complexity of the powder pattern. Given the known SCXRD structure of ZnAtzOx(H_2O) from the literature,[22] it is surprising that such different apparent C_Q values

would be observed for the different D_2O sites within the framework. Both known H_2O sites possess comparable proximities to the framework nuclei.

The previously reported structure of the as made $ZnAtzOx(H_2O)$ framework identified locations for H_2O oxygen atom within the pores.[22] The sites are arranged in alternating pore layers as viewed along the *b*-axis, shown in Figure 4.9. Based on the known position of the H_2O oxygen atom, one site (A) is located 3.04 Å from the amine nitrogen, 3.24 Å from the C – H carbon, and 3.46 Å from the oxalate carbons. The second site (B) is located 3.49 Å from the amine nitrogen, 3.51 Å from the C – H carbon and 3.51 Å from the oxalate carbons. While both sites are similarly positioned within the framework, site A is slightly more proximate to framework groups and likely corresponds to the broader feature within the ^2H SSNMR powder pattern (site 1 in Figure 4.8).

Regardless of the nature of the D_2O motions within $ZnAtzOx(H_2O)$, it is clear that the framework has strong interactions with water, and is capable of adsorbing water at temperatures as high as 393 K. This is not entirely surprising, given the literature activation conditions for $ZnAtzOx(H_2O)$,[22] which recommend a temperature of 423 K under vacuum to remove water adsorbed within the pores. There is also little temperature dependence of the D_2O behaviour that could be quantified, as the ^2H powder patterns possessed the same shape between 193 K and 393 K.

4.3.4 Static variable temperature ^{13}C SSNMR of H_2O and $^{13}CO_2$ loaded SIFSIX-3-Zn and $ZnAtzOx(H_2O)$

While the presence of moisture is known to inhibit CO_2 uptake in many MOFs, there are several ways in which the H_2O can affect the CO_2 guest. Broadly speaking, the adsorption sites for different guests can be either overlapping, distinct, or proximate.[32] A better understanding of

cosorption effects can be developed through ^{13}C SSNMR of a structure loaded with both water and CO_2.

After SIFSIX-3-Zn has coadsorbed H_2O and CO_2, the powder pattern parameters of the ^{13}C SSNMR spectra are unchanged from the phase containing no H_2O. The implication of this is that while moisture dramatically hinders the CO_2 uptake of SIFSIX-3-Zn, it is not changing the nature of the adsorption site for CO_2 within the structure. The H_2O is presumably occupying an adsorption site overlapping with that of the CO_2 such that it is completely blocked, or causing pore blockage within the structure, preventing the CO_2 from accessing adsorption sites within the structure. The H_2O induced phase change may also be altering the structure of the MOF such that suitable adsorption sites for CO_2 no longer exist.

However, after ZnAtzOx(H_2O) has coadsorbed H_2O and $^{13}CO_2$, there are notable changes to the ^{13}C SSNMR powder pattern, shown in Figure 4.10. The $^{13}CO_2$ loaded phase contains produced a pattern with relatively high skew and span parameters of 0.81(2) and 278(3) ppm at 293 K. In contrast, the resulting pattern from the coadsorbing phase possesses a significantly smaller skew and span values, of 0.46(4) and 240(3). This means the nature of the most occupied CO_2 adsorption site has changed after exposure to water. It is possible that the primary H_2O and CO_2 adsorption sites are identical or overlapping. The H_2O guest would therefore force the CO_2 molecule to occupy a less favourable, less confined second adsorption site, where the CO_2 is more mobile and less strongly adsorbed. Alternatively, given the small pores within ZnAtzOx(H_2O), guest-guest interactions between CO_2 and H_2O may be weakening the interaction between CO_2 and the framework.
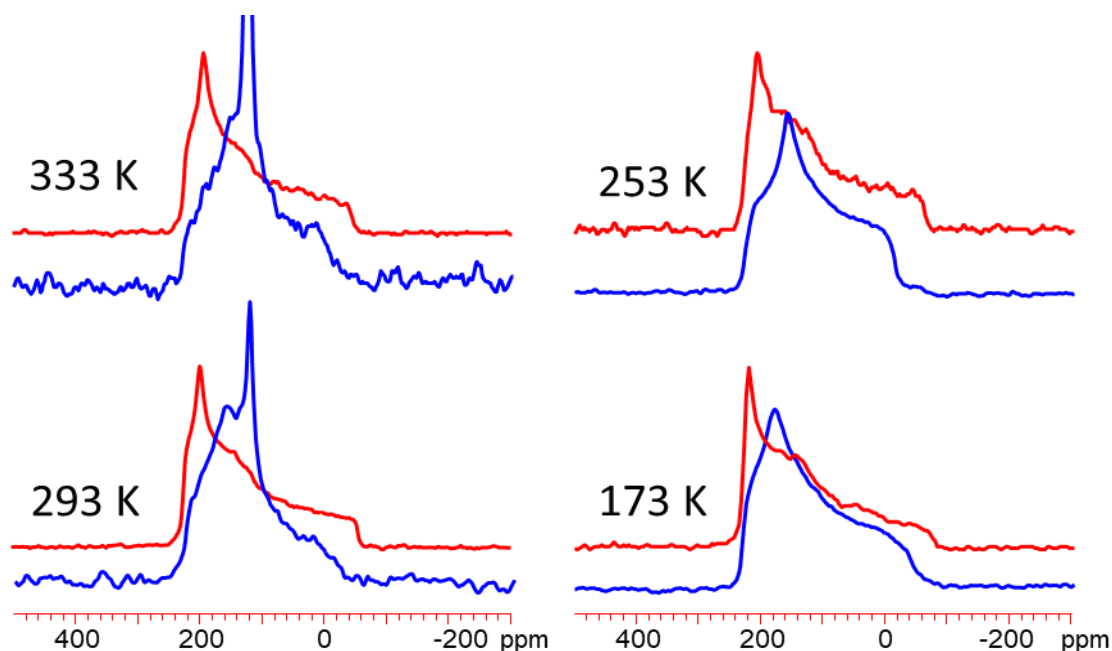
Figure 4.10: The experimental ^{13}C NMR spectrum of H_2O and $^{13}CO_2$-loaded SIFSIX-3-Zn at 333 K, 293 K, 253 K and 173 K is shown above in blue. The experimental spectra of SIFSIX-3-Zn when loaded with dry $^{13}CO_2$ is overlaid in red. The spectra were collected using 800 scans and a 2 s recycle delay.

Variable temperature static ^{13}C SSNMR experiments were performed on the sample, shown in Figure 4.11. As the sample is heated, the intensity of the sharp resonance at 126 ppm increases dramatically. This means that there is more free CO_2, with the MOF adsorbing less CO_2 at higher temperatures. Above temperatures of 333 K, no powder pattern corresponding to adsorbed $^{13}CO_2$ is apparent in the spectrum. This contrasts with the ^{13}C SSNMR powder patterns produced by the MOF when loaded with dry $^{13}CO_2$, where adsorbed $^{13}CO_2$ was detected by SSNMR at temperatures as high as 393 K. This suggests that CO_2 interacts much more weakly with this second adsorption site.
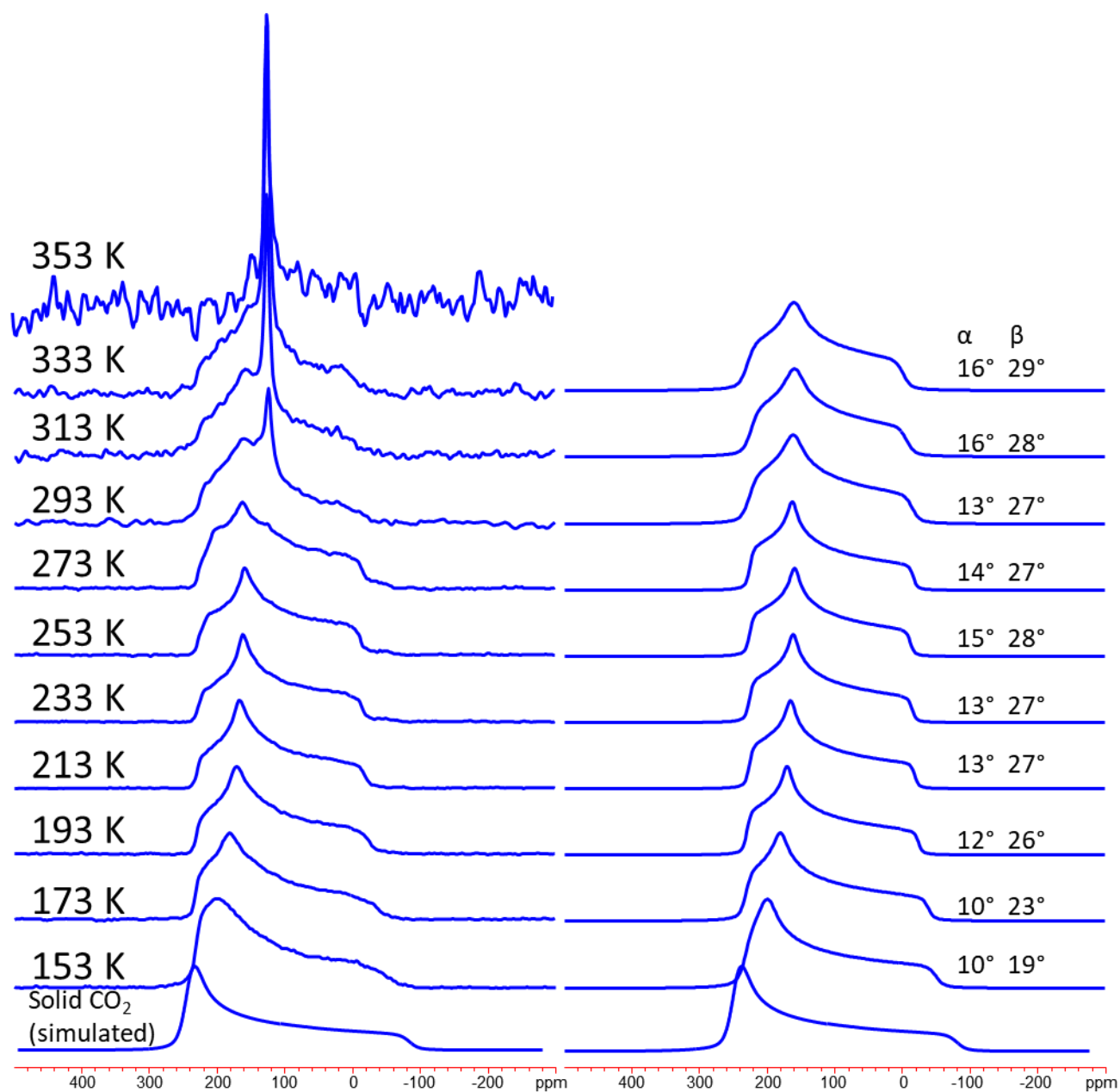
Figure 4.11: The experimental (left) and simulated (right) ^{13}C NMR spectra of H_2O and $^{13}CO_2$-loaded ZnAtzOx(H_2O) are shown at temperatures varying from 353 K to 153 K. The spectra were collected using between 800 and 2000 scans and a 2 s recycle delay. The C_6 rotational motion and C_2 hopping motion of CO_2 is described by the α and β angles listed on the simulated spectra. Simulated spectra of solid CO_2 depicted on the bottom for reference.[29]

Table 4.2: The observed ^{13}C chemical shift parameters H₂O and $^{13}CO2$-loaded ZnAtzOx(H₂O) are listed below. These parameters were obtained from analytical simulations of static ^{13}C SSNMR spectra using WSolids.[26]

Temperature (K)	δ_{iso} (ppm)	Ω (ppm)	K
333	130 (5)	230 (5)	0.40 (5)
313	126 (2)	230 (3)	0.44 (4)
293	125 (2)	240 (3)	0.46 (4)
273	125 (2)	241 (2)	0.48 (2)
253	125 (2)	237 (3)	0.44 (4)
233	125 (2)	240 (2)	0.46 (2)
213	125 (2)	244 (2)	0.50 (2)
193	126 (2)	253 (3)	0.53 (2)
173	125 (2)	269 (3)	0.62 (3)
153	127 (3)	282 (4)	0.77 (3)

A full list of powder pattern parameters across all experimental temperatures can be seen in Table 4.2. The CO_2 motions were quantified using EXPRESS[27] simulations. It was found that the CO_2 exhibited wobbling and C_2 hopping motions, described by the α and β angles respectively. These motions were also previously observed in the primary CO_2 adsorption site in ZnAtzOx(H₂O). The α angle was found to vary between 16° and 10°, while the β angle varied between 29° and 19°, throughout the temperature range used. The α angle values are comparable to those determined for the first CO_2 adsorption site. However, the β angle is much greater, having previously varied only from 18° to 12° over the course of the same temperature range. These greater β values for the second adsorption site are likely why the CO_2 evacuates at lower temperatures than what was observed for the first adsorption site.

4.4   Conclusions

^{2}H SSNMR experiments have been used to study H_2O adsorption in ultramicroporous frameworks known to be highly selective for the adsorption of CO_2 gas. It has been found that both SIFSIX-3-Zn and ZnAtzOx(H_2O) adsorb H_2O at temperatures as high as 393 K, and that the guest-host interactions between the framework and adsorbed D_2O do not change significantly with temperature. The lack of temperature dependence in guest-host interactions is characteristic of these frameworks, having also been observed when studying their CO_2 adsorption. The rates of motion of D_2O within SIFSIX-3-Zn have been quantified.

Additionally, the effects of H_2O on adsorbed CO_2 behaviour was studied in both frameworks using ^{13}C SSNMR. It was found that in ZnAtzOx(H_2O), H_2O forced the adsorbed CO_2 into a less preferential adsorption site, which was not able to adsorb CO_2 at temperatures above 333 K. The CO_2 within this second adsorption site was more mobile than the CO_2 previously observed in the first adsorption site. These motions were quantified through computer simulations.

This chapter helps illustrate the interactions of physical adsorbents with water, and how the water might affect the structures in CO_2 capture applications. The work outlined in this chapter is preliminary, and not yet suitable for publication until additional experiments confirm and supplement the findings. However, a better understanding of the interactions of a framework with all components of flue gas and open air, including H_2O, will aid in the future design of CO_2 capture materials.

4.5   References

1.   Burtch, N. C.; Jasuja, H.; Walton, K. S., Water Stability and Adsorption in Metal-Organic Frameworks. *Chemical Reviews* **2014,** *114* (20), 10575-10612.
2.   Wang, J. T.; Wang, S. F.; Xin, Q. P.; Li, Y. F., Perspectives on water-facilitated CO_2 capture materials. *Journal of Materials Chemistry A* **2017,** *5* (15), 6794-6816.

3.   Canivet, J.; Fateeva, A.; Guo, Y. M.; Coasne, B.; Farrusseng, D., Water adsorption in MOFs: fundamentals and applications. *Chemical Society Reviews* **2014,** *43* (16), 5594-5617.

4.   Low, J. J.; Benin, A. I.; Jakubczak, P.; Abrahamian, J. F.; Faheem, S. A.; Willis, R. R., Virtual High Throughput Screening Confirmed Experimentally: Porous Coordination Polymer Hydration. *Journal of the American Chemical Society* **2009,** *131* (43), 15834-15842.

5.   Granite, E. J.; Pennline, H. W., Photochemical removal of mercury from flue gas. *Industrial & Engineering Chemistry Research* **2002,** *41* (22), 5470-5476.

6.   Li, P. W.; Chen, J. H.; Zhang, J. Y.; Wang, X. L., Water Stability and Competition Effects Toward CO_2 Adsorption on Metal Organic Frameworks. *Separation and Purification Reviews* **2015,** *44* (1), 19-27.

7.   Caskey, S. R.; Wong-Foy, A. G.; Matzger, A. J., Dramatic tuning of carbon dioxide uptake via metal substitution in a coordination polymer with cylindrical pores. *Journal of the American Chemical Society* **2008,** *130* (33), 10870-+.

8.   Yu, J. M.; Balbuena, P. B., Water Effects on Postcombustion CO_2 Capture in Mg-MOF-74. *Journal of Physical Chemistry C* **2013,** *117* (7), 3383-3388.

9.   Kumar, A.; Madden, D. G.; Lusi, M.; Chen, K. J.; Daniels, E. A.; Curtin, T.; Perry, J. J.; Zaworotko, M. J., Direct Air Capture of CO_2 by Physisorbent Materials. *Angewandte Chemie-International Edition* **2015,** *54* (48), 14372-14377.

10.   Madden, D. G.; Scott, H. S.; Kumar, A.; Chen, K. J.; Sanii, R.; Bajpai, A.; Lusi, M.; Curtin, T.; Perry, J. J.; Zaworotko, M. J., Flue-gas and direct-air capture of CO_2 by porous metal-organic materials. *Philosophical Transactions of the Royal Society a-Mathematical Physical and Engineering Sciences* **2017,** *375* (2084).

11.   Nugent, P.; Belmabkhout, Y.; Burd, S. D.; Cairns, A. J.; Luebke, R.; Forrest, K.; Pham, T.; Ma, S.; Space, B.; Wojtas, L.; Eddaoudi, M.; Zaworotko, M. J., Porous materials with optimal adsorption thermodynamics and kinetics for CO_2 separation. *Nature* **2013,** *495* (7439), 80-84.

12.   Shekhah, O.; Belmabkhout, Y.; Adil, K.; Bhatt, P. M.; Cairns, A. J.; Eddaoudi, M., A facile solvent-free synthesis route for the assembly of a highly CO_2 selective and H_2S tolerant NiSIFSIX metal-organic framework. *Chemical Communications* **2015,** *51* (71), 13595-13598.

13.   Elsaidi, S. K.; Mohamed, M. H.; Schaef, H. T.; Kumar, A.; Lusi, M.; Pham, T.; Forrest, K. A.; Space, B.; Xu, W. Q.; Halder, G. J.; Liu, J.; Zaworotko, M. J.; Thallapally, P. K., Hydrophobic pillared square grids for selective removal of CO_2 from simulated flue gas. *Chemical Communications* **2015,** *51* (85), 15530-15533.

14.   Zhang, H.; Goeppert, A.; Prakash, G. K. S.; Olah, G., Applicability of linear polyethylenimine supported on nano-silica for the adsorption of CO_2 from various sources including dry air. *Rsc Advances* **2015,** *5* (65), 52550-52562.

15.   Xu, J.; Sinelnikov, R.; Huang, Y. N., Capturing Guest Dynamics in Metal-Organic Framework CPO-27-M (M = Mg, Zn) by H-2 Solid-State NMR Spectroscopy. *Langmuir* **2016,** *32* (22), 5468-5479.

16.   Dietzel, P. D. C.; Johnsen, R. E.; Blom, R.; Fjellvag, H., Structural changes and coordinatively unsaturated metal atoms on dehydration of honeycomb analogous microporous metal-organic frameworks. *Chemistry-a European Journal* **2008,** *14* (8), 2389-2397.

17.   Pavlov, M.; Siegbahn, P. E. M.; Sandstrom, M., Hydration of beryllium, magnesium, calcium, and zinc ions using density functional theory. *Journal of Physical Chemistry A* **1998,** *102* (1), 219-228.

18.   Mason, J. A.; McDonald, T. M.; Bae, T. H.; Bachman, J. E.; Sumida, K.; Dutton, J. J.; Kaye, S. S.; Long, J. R., Application of a High-Throughput Analyzer in Evaluating Solid Adsorbents for Post-Combustion Carbon Capture via Multicomponent Adsorption of CO_2, N_2, and H_2O. *Journal of the American Chemical Society* **2015,** *137* (14), 4787-4803.

19.   O'Nolan, D.; Kumar, A.; Zaworotko, M. J., Water Vapor Sorption in Hybrid Pillared Square Grid Materials. *Journal of the American Chemical Society* **2017,** *139* (25), 8508-8513.

20. Uemura, K.; Maeda, A.; Maji, T. K.; Kanoo, P.; Kita, H., Syntheses, Crystal Structures and Adsorption Properties of Ultramicroporous Coordination Polymers Constructed from Hexafluorosilicate Ions and Pyrazine. *European Journal of Inorganic Chemistry* **2009,** (16), 2329-2337.

21. Bakhmutov, V. I., Strategies for Solid-State NMR Studies of Materials: From Diamagnetic to Paramagnetic Porous Solids. *Chemical Reviews* **2011,** *111* (2), 530-562.

22. Banerjee, A.; Nandi, S.; Nasa, P.; Vaidhyanathan, R., Enhancing the carbon capture capacities of a rigid ultra-microporous MOF through gate-opening at low CO_2 pressures assisted by swiveling oxalate pillars. *Chemical Communications* **2016,** *52* (9), 1851-1854.

23. Hoffman, R. E., Standardization of chemical shifts of TMS and solvent signals in NMR solvents. *Magnetic Resonance in Chemistry* **2006,** *44* (6), 606-616.

24. Aliev, A. E.; Harris, K. D. M.; Apperley, D. C., HIGH-RESOLUTION SOLID-STATE C-13 AND SI-29 NMR INVESTIGATIONS OF THE DYNAMIC PROPERTIES OF TETRAKIS(TRIMETHYLSILYL)SILANE. *Journal of the Chemical Society-Chemical Communications* **1993,** (3), 251-253.

25. Zhang, Y.; Lucier, B. E. G.; Huang, Y. N., Deducing CO_2 motion, adsorption locations and binding strengths in a flexible metal-organic framework without open metal sites. *Physical Chemistry Chemical Physics* **2016,** *18* (12), 8327-8341.

26. Eichele, R. E. W. K. *WSolids1*, University of Tübingen: Germany, 2001.

27. Vold, R. L.; Hoatson, G. L., Effects of jump dynamics on solid state nuclear magnetic resonance line shapes and spin relaxation times. *Journal of Magnetic Resonance* **2009,** *198* (1), 57-72.

28. CRC Handbook of Chemistry and Physics. CRC Press: Boca Raton, FL, 2005.

29. Beeler, A. J.; Orendt, A. M.; Grant, D. M.; Cutts, P. W.; Michl, J.; Zilm, K. W.; Downing, J. W.; Facelli, J. C.; Schindler, M. S.; Kutzelnigg, W., LOW-TEMPERATURE C-13 MAGNETIC-RESONANCE IN SOLIDS .3. LINEAR AND PSEUDOLINEAR MOLECULES. *Journal of the American Chemical Society* **1984,** *106* (25), 7672-7676.

30. Chihara, H.; Nakamura, N., *Nuclear Quadrupole Resonance Data*. Springer: Berlin, 1997.

31. Long, J. R.; Ebelhauser, R.; Griffin, R. G., H-2 NMR line shapes and spin-lattice relaxation in Ba(ClO_3)(2)center dot(H_2O)-H-2. *Journal of Physical Chemistry A* **1997,** *101* (6), 988-994.

32. Jeong, W.; Kim, J., Understanding the Mechanisms of CO2 Adsorption Enhancement in Pure Silica Zeolites under Humid Conditions. *Journal of Physical Chemistry C* **2016,** *120* (41), 23500-23510.

4.6   Appendix

Table S4.1: Acquisition parameters for VT static ^2H SSNMR of D_2O loaded SIFSIX-3-Zn are shown below.

Sample	Temperature (K)	Acquisitions	Decoupled Nucleus	Pulse Delay (s)	90° Pulse Width (μs)
SIFSIX-3-Zn,	393 K	1802	^1H	2	4.5
D_2O Loaded	373 K	1803	^1H	2	4.5
	353 K	18210	^1H	2	4.5
	333 K	1920	^1H	2	4.5
	313 K	2482	^1H	2	4.5
	293 K	3000	^1H	2	4.5
	273 K	1835	^1H	2	4.5
	253 K	2276	^1H	2	4.5
	233 K	3711	^1H	2	4.5
	213 K	2590	^1H	2	4.5
	193 K	1803	^1H	2	4.5
	173 K	1801	^1H	2	4.5
	153 K	1805	^1H	2	4.5

Table S4.2: Acquisition parameters for VT static ^2H SSNMR of D_2O loaded ZnAtzOx(H_2O) are shown below.

Sample	Temperature (K)	Acquisitions	Decoupled Nucleus	Pulse Delay (s)	90° Pulse Width (µs)
ZnAtzOx(H_2O), D_2O Loaded	393 K	3790	^1H	2	4.5
	373 K	8760	^1H	2	4.5
	353 K	3605	^1H	2	4.5
	333 K	3773	^1H	2	4.5
	313 K	3707	^1H	2	4.5
	293 K	31120	^1H	2	4.5
	273 K	3615	^1H	2	4.5
	253 K	3614	^1H	2	4.5
	233 K	3624	^1H	2	4.5
	213 K	3602	^1H	2	4.5
	193 K	3616	^1H	2	4.5
	173 K	3606	^1H	2	4.5
	153 K	3615	^1H	2	4.5

Table S4.3: Acquisition parameters for VT static ^{13}C SSNMR of $^{13}CO2$ and H_2O loaded ZnAtzOx(H_2O) are shown below.

Sample	Temperature (K)	Acquistions	Decoupled Nucleus	Pulse Delay (s)	90° Pulse Width (µs)
ZnAtzOx(H_2O), $^{13}CO_2$ and H_2O Loaded	333 K	1689	^1H	2	2.7
	313 K	1668	^1H	2	2.7
	293 K	1653	^1H	2	2.7
	273 K	969	^1H	2	2.8
	253 K	830	^1H	2	2.8
	233 K	961	^1H	2	2.8
	213 K	924	^1H	2	2.8
	193 K	867	^1H	2	2.8
	173 K	887	^1H	2	2.8
	153 K	867	^1H	2	2.8

Chapter 5 : Summary and Future Works

5.1   Summary

In this work, the motions, interactions and adsorption sites of CO_2 and H_2O within highly selective ultramicroporous frameworks were investigated using solid-state nuclear magnetic resonance (SSNMR) and single-crystal X-ray diffraction (SCXRD). The results highlighted the strong guest-host interactions within these frameworks, and the low degree of temperature dependence in guest molecule behaviour.

In Chapter 2, the adsorption of CO_2 within SIFSIX-3-Zn was studied. SCXRD of the CO_2 loaded crystal at 110 K was able to precisely locate the CO_2 adsorption site within the pore, located between fluorine and hydrogen atoms of the framework. SCXRD was additionally able to quantify changes in the framework structure after CO_2 loading, which strengthened guest-host interactions. ^{13}C variable temperature (VT) SSNMR experiments on $^{13}CO_2$ loaded samples found that the wobbling motions of the CO_2 molecule exhibited an anomalously low degree of temperature dependence, due to the strong interactions between the host and guest. Guest-host interactions were analyzed using magic-angle spinning (MAS), cross polarization (CP) and rotational-echo double resonance (REDOR) SSNMR experiments, finding evidence of dipolar interactions between fluorine and hydrogen nuclei from the framework and the adsorbed carbon nuclei. A low degree of temperature dependence was found for the strength of the interaction between hydrogen and carbon nuclei, with the interaction growing stronger at 223 K compared to 293 K. ^{67}Zn SSNMR conducted at 21.1 T showed that the EFG about the Zn nucleus changed after activation, likely due to changes in the bond lengths creating a more symmetrical environment about the Zn nucleus.

Chapter 3 focuses on studying the CO_2 gas behaviour within the amine-functionalized ultramicropores of the ZnAtzOx framework. Within ZnAtzOx(H_2O), ^{13}C VT SSNMR experiments on [13]CO_2 loaded samples found small wobbling and hopping guest motions with low temperature dependence. MAS/CP and hetero nuclear correlation (HETCOR) SSNMR experiments found weak interactions between the framework protons and guest ^{13}C nuclei. HETCOR experiments found that the guest ^{13}C nuclei possessed weak interactions with both kinds of framework protons, suggesting there was no clear adsorption site at room temperature. High-field [67]Zn SSNMR identified changes in the EFG about both Zn sites, thought to be due to changes in the bond strength between Zn and O. An alternative ZnAtzOx phase, ZnAtzOx(EtOH), also had the behaviour of guest [13]CO_2 molecules investigated through VT ^{13}C SSNMR experiments. It was found that the CO_2 in this framework exhibited notably more motional freedom than the CO_2 within ZnAtzOx(H_2O), despite their conformational nature.

Chapter 4 showcased the preliminary results of water adsorption studies within SIFSIX-3-Zn and ZnAtzOx(H_2O). ^{2}H static VT SSNMR experiments on D_2O loaded samples determined the number of adsorption sites within each MOF, and found there was a low degree of temperature dependence for the D_2O behaviour within both frameworks. High-field [67]Zn SSNMR found that the Zn environment in SIFSIX-3-Zn was completely changed when the sample was saturated with water, due to the material's phase change. ^{13}C SSNMR experiments found that H_2O adsorption within ZnAtzOx(H_2O) was found to alter and weaken the interaction between the framework and guest CO_2 when both were loaded simultaneously into the framework.

5.2   Suggestions for Future Work

A comprehensive knowledge of the interactions between water, SIFSIX-3-Zn and ZnAtzOx would clarify H_2O adsorption within these frameworks, building on the research begun

in Chapter 4. Structural studies using SCXRD, or more comprehensive SSNMR studies targeting different nuclei, would be useful in understanding how the framework changes upon exposure to H_2O. Alternatively, H_2O interactions with similar SIFSIX-3-M materials could be explored. Materials such as SIFSIX-3-Cu and SIFSIX-3-Ni are not as sensitive as SIFSIX-3-Zn to water,[1, 2] and so an understanding of the differences in interactions between SIFSIX-3-Zn and other members of the SIFSIX-3-M family can further elaborate on the impact of H_2O on CO_2 adsorption. Studying other SIFSIX-3-M Materials using SSNMR would be difficult however, due to their paramagnetic nature,[3] so experiments would primarily need to focus on the use of SCXRD or alternative techniques. Similar SSNMR and SCXRD techniques can be applied to different families of materials, such as UiO-66-NH$_2$, which possesses a strong uptake of both water and CO_2 due to amine functionalization.[4]

The interactions between CO_2 and H_2O while within the same framework are of particular interest, due to the presence of both molecules within flue gas. While experiments in Chapter 4 showed that the behaviour of CO_2 in ZnAtzOx(H_2O) was affected by the presence of water in the framework, additional SSNMR experiments, such as those employing MAS and CP, could help highlight changes in guest-host interactions between CO_2 and ZnAtzOx due to the presence of water, or identify guest-host interactions between water and ZnAtzOx. Similarly, while static ^{13}C experiments could not identify changes in the CO_2 behaviour within SIFSIX-3-Zn due to water, more comprehensive experiments employing CP and MAS may identify interactions between the two guest molecules.

This work has demonstrated the strong guest-host interactions and unusual CO_2 behaviour within certain ultramicroporous MOFs without open metal sites. Future work can be focused on structural modification to further strengthen the electrostatic interactions between pillared

ultramicroporous structures and their guest molecules, particularly carbon dioxide. With additional research into guest-host interactions of ultramicroporous frameworks, structures can be further tuned to promote stronger selectivities towards other industrial gases such as xenon and acetylene.[5, 6] The low temperature dependence of CO_2 adsorption within such frameworks allows for the use of MAS SSNMR, greatly increasing the effectiveness of SSNMR in understanding host-guest interactions. Continued use of MAS SSNMR experiments on guest-loaded structures will help in understanding guest-host interactions in more novel ultramicroporous frameworks such as NbOFFIVE materials.[7]

5.3   References

1.   Kumar, A.; Madden, D. G.; Lusi, M.; Chen, K. J.; Daniels, E. A.; Curtin, T.; Perry, J. J.; Zaworotko, M. J., Direct Air Capture of CO_2 by Physisorbent Materials. *Angewandte Chemie-International Edition* **2015,** *54* (48), 14372-14377.

2.   Madden, D. G.; Scott, H. S.; Kumar, A.; Chen, K. J.; Sanii, R.; Bajpai, A.; Lusi, M.; Curtin, T.; Perry, J. J.; Zaworotko, M. J., Flue-gas and direct-air capture of CO_2 by porous metal-organic materials. *Philosophical Transactions of the Royal Society a-Mathematical Physical and Engineering Sciences* **2017,** *375* (2084).

3.   Bertmer, M., Paramagnetic solid-state NMR of materials. *Solid State Nuclear Magnetic Resonance* **2017,** *81*, 1-7.

4.   Madden, D. G.; Scott, H. S.; Kumar, A.; Chen, K. J.; Sanii, R.; Bajpai, A.; Lusi, M.; Curtin, T.; Perry, J. J.; Zaworotko, M. J., Flue-gas and direct-air capture of CO_2 by porous metal-organic materials. *Philosophical Transactions of the Royal Society a-Mathematical Physical and Engineering Sciences* **2017,** *375* (2084).

5.   Elsaidi, S. K.; Mohamed, M. H.; Simon, C. M.; Braun, E.; Pham, T.; Forrest, K. A.; Xu, W. Q.; Banerjee, D.; Space, B.; Zaworotko, M. J.; Thallapally, P. K., Effect of ring rotation upon gas adsorption in SIFSIX-3-M (M = Fe, Ni) pillared square grid networks. *Chemical Science* **2017,** *8* (3), 2373-2380.

6.   Sikora, B. J.; Wilmer, C. E.; Greenfield, M. L.; Snurr, R. Q., Thermodynamic analysis of Xe/Kr selectivity in over 137 000 hypothetical metal-organic frameworks. *Chemical Science* **2012,** *3* (7), 2217-2223.

7.   Bhatt, P. M.; Belmabkhout, Y.; Cadiau, A.; Adil, K.; Shekhah, O.; Shkurenko, A.; Barbour, L. J.; Eddaoudi, M., A Fine-Tuned Fluorinated MOF Addresses the Needs for Trace CO_2 Removal and Air Capture Using Physisorption. *Journal of the American Chemical Society* **2016,** *138* (29), 9301-9307.

<u>Curriculum Vitae</u>

Name: Bligh Desveaux

Post-secondary   Dalhousie University

Education and   Halifax, Nova Scotia, Canada
Degrees: 2011-2015 B.Sc.

                  The University of Western Ontario
                  London, Ontario, Canada
                  2016-2017 M.Sc.

Honours and   Dalhousie Entrance Scholarship
Awards: 2012

                  Dalhousie Science Entrance Scholarship
                  2012

                  Dalhousie Dean's Honour Roll
                  2012

                  Dalhousie In-Course Scholarship
                  2013

Related Work   Teaching Assistant
Experience   The University of Western Ontario
                  2016-2017

Posters: **Desveaux, B.;** Lucier, B.; Terskikh, V.; Boyle, P.; Huang, Y. "Deducing Adsorbed CO_2, Gas Behaviour in Ultramicroporous Metal-Organic Frameworks using Solid-State NMR Spectroscopy" 100th Canadian Chemistry Conference and Exhibition, Toronto ON, June 2017, & at the 30th Annual MOOT NMR Conference, London ON, September 2017.